



저작자표시-비영리-변경금지 2.0 대한민국

이용자는 아래의 조건을 따르는 경우에 한하여 자유롭게

- 이 저작물을 복제, 배포, 전송, 전시, 공연 및 방송할 수 있습니다.

다음과 같은 조건을 따라야 합니다:



저작자표시. 귀하는 원저작자를 표시하여야 합니다.



비영리. 귀하는 이 저작물을 영리 목적으로 이용할 수 없습니다.



변경금지. 귀하는 이 저작물을 개작, 변형 또는 가공할 수 없습니다.

- 귀하는, 이 저작물의 재이용이나 배포의 경우, 이 저작물에 적용된 이용허락조건을 명확하게 나타내어야 합니다.
- 저작권자로부터 별도의 허가를 받으면 이러한 조건들은 적용되지 않습니다.

저작권법에 따른 이용자의 권리는 위의 내용에 의하여 영향을 받지 않습니다.

이것은 [이용허락규약\(Legal Code\)](#)을 이해하기 쉽게 요약한 것입니다.

[Disclaimer](#)

Ph.D. DISSERTATION

**A Study for a Totally Implantable
Visual Prosthetic System**

완전 이식형 시각 보철 시스템을 위한 연구

BY

SHINYONG SHIM

FEBRUARY 2020

**DEPARTMENT OF ELECTRICAL
AND COMPUTER ENGINEERING
COLLEGE OF ENGINEERING
SEOUL NATIONAL UNIVERSITY**

A Study for a Totally Implantable Visual Prosthetic System

지도교수 김 성 준

이 논문을 공학박사 학위논문으로 제출함.

2020년 1월

서울대학교 대학원

전기·정보공학부

심 신 용

심 신 용의 공학박사 학위논문을 인준함.

2019년 12월

위 원 장 홍 용 택 (인)

부위원장 김 성 준 (인)

위 원 서 강 문 (인)

위 원 서 중 모 (인)

위 원 전 상 범 (인)

Abstract

A visual prosthetic system typically consists of a neural stimulator, which is a surgically implantable device for electrical stimulation intended to restore the partial vision of blind patients, and peripheral external devices including an image sensor, a controller, and a processor. Although several visual prosthetic systems, such as retinal prostheses or retinal implants, have already been commercialized, there are still many issues on them (e.g., substrate materials for implantable units, electrode configurations, the use of external hardware, power supply and data transmission methods, design and fabrication approaches, etc.) to be dealt with for an improved visual prosthetic system. In this dissertation, a totally implantable visual prosthetic system is suggested with four motivations, which are thought to be important, as in the following: 1) simple fabrication of implantable parts, such as micro-sized electrodes and a case, for a neural stimulator based on polymer without semiconductor techniques, 2) multi-polar stimulation for virtual channel generation to overcome a limited number of physical electrodes in a confined space, 3) a new image acquisition strategy using an implantable camera, and 4) power supply as well as data transmission to a neural stimulator without hindering patient's various activities.

First, polymer materials have been widely used to develop various implantable devices for visual prosthetic systems because of their outstanding advantages including flexibility and applicability to microfabrication, compared with metal, silicon, or ceramic. Most polymer-based implantable devices have been

fabricated by the semiconductor technology based on metal deposition and photolithography. This technology provides high accuracy and precision for metal patterning on a polymer substrate. However, the technology is also complicated and time-consuming as it requires masks for photolithography and vacuum for metal deposition as well as huge fabrication facilities. This is the reason why biocompatible cyclic olefin polymer (COP) with low water absorption (<0.01 %) and high light transmission (92 %) was chosen as a new substrate material of an implantable device in this study. Based on COP, simple fabrication process of an implantable device was developed without masks, vacuum, and huge fabrication facilities. COP is characterized by strong adhesion to gold and high ultraviolet (UV) transparency as well. Because of such adhesion and UV transparency, a gold thin film can be thermally laminated on a COP substrate with no adhesion layer and micromachined by a UV laser without damaging the substrate. Using the developed COP-based process, a depth-type microprobe was fabricated first, and its electrochemical and mechanical properties as well as functionality were evaluated by impedance measurements, buckling tests, and *in vivo* neural signal recording, respectively. Furthermore, the long-term reliability of COP encapsulation formed by the developed process was estimated through leakage current measurements during accelerated aging in saline solution, to show the feasibility of the encapsulation using COP as well.

Second, even if stimulation electrodes become sufficiently small, it is demanding to arrange them for precise stimulation on individual neurons due to electrical crosstalk, which is the spatial superposition of electric fields generated by

simultaneous stimuli. Hence, an adequate spacing between adjacent electrodes is required, and this causes a limited number of physical electrodes in a confined space such as in the brain or in the retina. To overcome this limitation, many researchers have proposed stimulation strategies using virtual channels, which are intermediate areas with large magnitudes of electric fields between physical electrodes. Such virtual channels can be created by multi-polar stimulation that can combine stimuli output from two or more electrodes at the same time. To produce more delicate stimulation patterns using virtual channels herein, penta-polar stimulation with a grid-shaped arrangement of electrodes was leveraged specially to generate them in two dimensions. This penta-polar stimulation was realized using a custom-designed integrated circuit with five different current sources and surface-type electrodes fabricated by the developed COP-based process. The effectiveness of the penta-polar stimulation was firstly evaluated by focusing electric fields in comparison to mono-polar stimulation. In addition, the distribution of electric fields changed by the penta-polar stimulation, which indicated virtual channel generation, was estimated in accordance with an amplitude ratio between stimuli of the two adjacent electrodes and a distance from them, through both finite element analysis and *in vitro* evaluation.

Third, an implantable camera is herein proposed as a new image acquisition approach capturing real-time images while implanted in the eye, to construct a totally implantable visual prosthetic system. This implantable camera has distinct advantages in that it can provide blind patients with benefits to perform several ordinary activities, such as sleep, shower, or running, while focusing on objects in accordance with natural eye movements. These advantages are impossible

to be achieved using a wearing unit such as a glasses-mounted camera used in a conventional partially implantable visual prosthetic system. Moreover, the implantable camera also has a merit of garnering a variety of image information using the complete structure of a camera, compared with a micro-photodiode array of a retinal implant. To fulfill these advantageous features, after having been coated with a biocompatible epoxy to prevent moisture penetration and sealed using a medical-grade silicone elastomer to gain biocompatibility as well as flexibility, the implantable camera was fabricated enough to be inserted into the eye. Its operation was assessed by wireless image acquisition that displayed a processed black and white image. In addition, to estimate reliable wireless communication ranges of the implantable camera in the body, signal-to-noise ratio measurements were conducted while it was covered by an 8-mm-thick biological medium that mimicked an *in vivo* environment.

Lastly, external hardware attached on the body has been generally used in conventional visual prosthetic systems to stably deliver power and data to implanted units and to acquire image signals outside the body. However, there are common problems caused by this external hardware, including functional failure due to external damages, unavailability during sleep, in the shower, or while running or swimming, and cosmetic issues. Especially, an external coil for power and data transmission in a conventional visual prosthetic system is connected to a controller and processor through a wire, which makes the coil more vulnerable to the problems. To solve this issue, a totally implantable neural stimulation system controlled by a handheld remote controller is presented. This handheld remote controller can control

a totally implantable stimulator powered by a rechargeable battery through low-power but relatively long-range ZigBee wireless communication. Moreover, two more functions can be performed by the handheld controller for expanded applications; one is percutaneous stimulation, and the other is inductive charging of the rechargeable battery. Additionally, simple switches on the handheld controller enable users to modulate parameters of stimuli like a gamepad. These handheld and user-friendly interfaces can make it easy to use the controller under various circumstances. The functionality of the controller was evaluated *in vivo*, through percutaneous stimulation and remote control especially for avian navigation, as well as *in vitro*. Results of both *in vivo* experiments were compared in order to verify the feasibility of remote control of neural stimulation using the controller.

In conclusion, several discussions on results of this study, including the COP-based simple fabrication process, the penta-polar stimulation, the implantable camera, and the multi-functional handheld remote controller, are addressed. Based on these findings and discussions, how the researches in this thesis can be applied to the realization of a totally implantable visual prosthetic system is elucidated at the end of this dissertation.

Keywords: totally implantable, visual prosthetic system, cyclic olefin polymer, simple fabrication process, penta-polar stimulation, virtual channel, implantable camera, multi-functional handheld remote controller

Student number: 2015-20942

Contents

Abstract	i
Contents	vi
List of Figures	xi
List of Tables	xx
List of Abbreviations	xxii
Chapter 1. Introduction	1
1.1. Visual Prosthetic System	2
1.1.1. Current Issues	2
1.1.1.1. Substrate Materials	3
1.1.1.2. Electrode Configurations	5
1.1.1.3. External Hardware	6
1.1.1.4. Other Issues	7
1.2. Suggested Visual Prosthetic System	8
1.3. Four Motivations	10
1.4. Proposed Approaches	11
1.4.1. Cyclic Olefin Polymer (COP)	11
1.4.2. Penta-Polar Stimulation	13
1.4.3. Implantable Camera	16
1.4.4. Handheld Remote Controller	18

1.5. Objectives of this Dissertation	20
Chapter 2. Materials and Methods	23
2.1. COP-Based Fabrication and Encapsulation	24
2.1.1. Overview	24
2.1.2. Simple Fabrication Process	24
2.1.3. Depth-Type Microprobe	26
2.1.3.1. Design	26
2.1.3.2. Characterization	27
2.1.3.3. <i>In Vivo</i> Neural Signal Recording	30
2.1.4. COP Encapsulation	31
2.1.4.1. <i>In Vitro</i> Reliability Test	33
2.2. Penta-Polar Stimulation	34
2.2.1. Overview	34
2.2.2. Design and Fabrication	35
2.2.2.1. Integrated Circuit (IC) Design	35
2.2.2.2. Surface-Type Electrode Fabrication	38
2.2.3. Evaluations	39
2.2.3.1. Focused Electric Field Measurement	42
2.2.3.2. Steered Electric Field Measurement	42
2.3. Implantable Camera	43
2.3.1. Overview	43
2.3.2. Design and Fabrication	43

2.3.2.1. Circuit Design -----	43
2.3.2.2. Wireless Communication Program -----	46
2.3.2.3. Epoxy Coating and Elastomer Sealing -----	47
2.3.3. Evaluations -----	50
2.3.3.1. Wireless Image Acquisition -----	50
2.3.3.2. Signal-to-Noise Ratio (SNR) Measurement -----	52
2.4. Multi-Functional Handheld Remote Controller -----	53
2.4.1. Overview -----	53
2.4.2. Design and Fabrication -----	53
2.4.2.1. Hardware Description -----	53
2.4.2.2. Software Description -----	57
2.4.3. Evaluations -----	57
2.4.3.1. <i>In Vitro</i> Evaluation -----	57
2.4.3.2. <i>In Vivo</i> Evaluation -----	59
Chapter 3. Results -----	61
3.1. COP-Based Fabrication and Encapsulation -----	62
3.1.1. Fabricated Depth-Type Microprobe -----	62
3.1.1.1. Electrochemical Impedance -----	63
3.1.1.2. Mechanical Characteristics -----	64
3.1.1.3. <i>In Vivo</i> Neural Signal Recording -----	66
3.1.2. COP Encapsulation -----	68
3.1.2.1. <i>In Vitro</i> Reliability Test -----	68

3.2. Penta-Polar Stimulation	70
3.2.1. Fabricated IC and Surface-Type Electrodes	70
3.2.2. Evaluations	73
3.2.2.1. Focused Electric Field Measurement	73
3.2.2.2. Steered Electric Field Measurement	75
3.3. Implantable Camera	76
3.3.1. Fabricated Implantable Camera	76
3.3.2. Evaluations	77
3.3.2.1. Wireless Image Acquisition	77
3.3.2.2. SNR Measurement	78
3.4. Multi-Functional Handheld Remote Controller	80
3.4.1. Fabricated Remote Controller	80
3.4.2. Evaluations	81
3.4.2.1. <i>In Vitro</i> Evaluation	81
3.4.2.2. <i>In Vivo</i> Evaluation	83
Chapter 4. Discussions	86
4.1. COP-Based Fabrication and Encapsulation	87
4.1.1. Fabrication Process and Fabricated Devices	87
4.1.2. Encapsulation and Optical Transparency	89
4.2. Penta-Polar Stimulation.....	99
4.2.1. Designed IC and Electrode Configurations	99
4.2.2. Virtual Channels in Two Dimensions	101

4.3. Implantable Camera	102
4.3.1. Enhanced Reliability by Epoxy Coating	106
4.4. Multi-Functional Handheld Remote Controller	107
4.4.1. Brief Discussions of the Two Extra Functions	108
4.5. Totally Implantable Visual Prosthetic System	113
Chapter 5. Conclusion	117
References	121
Supplements	133
국문 초록	143

List of Figures

- Figure 1.2.1 A conceptual view of the suggested totally implantable visual prosthetic system that consists of an implantable neural stimulator and an implantable camera as well as an external controller and processor. --- 9
- Figure 1.4.1 Schematic diagrams of electric field distribution: mono-polar stimulation (top), multi-polar stimulation (middle), and multi-polar stimulation with current steering (bottom). ----- 14
- Figure 2.1.1 Simple fabrication process of a depth-type microprobe based on COP consisting of seven steps: (a) preparation of a COP film as a substrate, (b) thermal lamination of a gold thin film on the COP substrate, (c) UV laser ablation for gold patterning, (d) preparation of another COP film as a cover, (e) CO₂ laser cutting to open electrode sites and connection pads on the COP cover, (f) thermal lamination of the substrate and the cover with an adhesion COP layer between them, and (g) CO₂ laser cutting to shape an outline of a depth-type microprobe. ----- 25
- Figure 2.1.2 A schematically drawn COP-based depth-type microprobe with four different channels having an individual geometrical surface area of 100×100 μm and with a shank length of 10 mm. ----- 27
- Figure 2.1.3 A three-electrode arrangement setup of an electrochemical impedance measurement using the COP-based depth-type microprobe. ----- 28
- Figure 2.1.4 A conceptual diagram of a buckling test to measure mechanical characteristics of the COP-based depth-type microprobe. ----- 28

Figure 2.1.5 Fabrication procedures of IDEs on a COP film by the developed process.	31
Figure 2.1.6 A diagram illustrating leakage current measurements of four IDEs in the COP encapsulation during accelerated aging in 75 °C saline solution.	32
Figure 2.2.1 A circuit block diagram of the custom-designed penta-polar stimulation ASIC.	34
Figure 2.2.2 Micropatterned gold lines on a COP substrate by the developed fabrication process. These surface-type electrodes had five electrode sites, noted as channels, with an individual diameter of 450 μm and a center-to-center spacing of 800 μm.	38
Figure 2.2.3 Evaluation setups for (a) the FEA and (b) the <i>in vitro</i> evaluation to estimate the spatial electric field distribution formed by the penta-polar stimulation.	40
Figure 2.2.4 Schematic diagrams showing configurations of mono-polar (top) and penta-polar stimulation (bottom) to estimate the effectiveness on focusing electric fields generated by the penta-polar stimulation.	41
Figure 2.2.5 An illustration that depicts the configuration of the penta-polar stimulation with current steering for virtual channel generation.	42
Figure 2.3.1 A circuit block diagram of the implantable camera connected with a power module.	44
Figure 2.3.2 Schematically drawn PCBs of the implantable camera, which were stacked for three-layered structure to be packaged in a spherical form.	-

-----	45
Figure 2.3.3 Photographs of PCBs of the implantable camera before (left) and after (right) underwent epoxy coating, respectively. -----	48
Figure 2.3.4 Procedures of elastomer sealing. (a) Three parts of a molding jig were assembled to make an elastomer shell first. The elastomer was injected into the jig through the inlet at the top. (b) The elastomer shell in a spherical form was molded. (c) The epoxy-coated circuits of the implantable camera were put into the shell. (d) Using the jig without the middle part, the shell containing the circuits was fixed, and (e) the elastomer was injected again to fill the empty space in the shell with the circuits. (f) The elastomer-sealed implantable camera was fabricated like the shape of an eyeball. -----	49
Figure 2.3.5 A BLE communication program algorithm for a wireless image acquisition test using the implantable camera: (a) the TX operation of the implantable camera and (b) the RX operation of an image receiver while connected to a computer. -----	51
Figure 2.4.1 A block diagram of the HNS-controller that can be used for both percutaneous stimulation and remote control of neural stimulation. --	54
Figure 2.4.2 (a) An FPGA program block diagram for the HNS-controller and (b) a flow chart of the FPGA program. -----	56
Figure 2.4.3 A schematic of a totally implantable neural stimulator designed for remote neural stimulation control using the HNS-controller. -----	58
Figure 2.4.4 An illustration of the proposed totally implantable neural stimulation	

system applied to remote avian navigation. ----- 59

Figure 3.1.1 Photographs of the COP-based depth-type microprobe: an image of its overall structure (left) and a microscopic image of the gold patterns (right) comprising the shank of the microprobe highlighted by the red square. ----- 62

Figure 3.1.2 A microscopic image of a gold channel of the COP-based depth-type microprobe. The geometrical surface area of the channel was $100 \times 100 \mu\text{m}$, though its effective surface area would be larger because of the rough surface of the gold thin film. ----- 63

Figure 3.1.3 Results of the buckling tests. (a) A graph of thickness-dependent averaged applied forces vs. displacement. The thicknesses of the COP-based depth-type microprobes were set to be 50 (the number of specimens, $n=6$), 100 ($n=6$), and 200 μm ($n=4$), while they had the same width of 650 μm . (b) A graph of material-related averaged applied forces vs. displacement. The tungsten rod with a diameter of 200 μm and the LCP-based microprobes ($n=3$) with a cross-section area of 650 (width, W) \times 100 (thickness, T) μm were also used in the buckling tests for comparison. ----- 65

Figure 3.1.4 Results of the *in vivo* simultaneous multi-channel neural signal recording. Different color-coded units of the neural signals were sorted according to their shapes of waveforms, after recorded on the four channels of the 100- μm -thick COP-based depth-type microprobe. --- 67

Figure 3.1.5 Raster plots that display the corresponding units of the neural signals

over time. -----	67
Figure 3.1.6 Leakage current measurement results during the accelerated aging tests of the COP encapsulation formed under (a) a lower pressure of 0.051 MPa (Group 1) and (b) a higher pressure of 0.509 MPa (Group 2). The threshold level of 1 μ A (the black dashed line) was set arbitrarily. ----	68
Figure 3.1.7 The two groups of the COP encapsulation harvested after the complete moisture and ion penetration. -----	69
Figure 3.2.1 The custom-designed penta-polar stimulation ASIC fabricated with a size of 4.5 \times 2.4 mm. -----	70
Figure 3.2.2 Five biphasic current pulses supplied from the fabricated penta-polar stimulation ASIC at the same time. -----	71
Figure 3.2.3 A result graph of cyclic voltammetry conducted using the COP-based surface-type electrodes with a scanning rate of 50 mV/s from -0.6 to 0.8 V. -----	73
Figure 3.2.4 Electric fields simulated and measured from the FEA and the <i>in vitro</i> evaluation, respectively, with comparison results between the mono-polar and the penta-polar stimulation. -----	74
Figure 3.2.5 The weighted centroids of electric field magnitudes, virtual channels, plotted from both the FEA and the <i>in vitro</i> evaluation results in accordance with the distance, while varying the amplitude ratio between the stimuli of the two adjacent stimulation electrodes (x-axis: Location X, μ m and y-axis: Location Y, μ m). -----	76
Figure 3.3.1 A photograph of the fabricated implantable camera in a spherical form	

and the power module, which were coated by the biocompatible epoxy and sealed using the medical-grade silicone elastomer. ----- 77

Figure 3.3.2 A test setup for wireless image acquisition and two restored photographs of black and white images of 'ABC' with 38×24 pixels. ----- 78

Figure 3.3.3 The SNR of received signals at the BLE image receiver while varying the communication distances and directions. The green, orange, and red lines indicated the measurements using the unpackaged implantable camera, the packaged one, and the packaged one covered by a biological medium, respectively. The black dashed line was an acceptable SNR of 25 dB for reliable wireless communication. ----- 79

Figure 3.4.1 Photographs of (a) the top-view and (b) the bottom-view of the fabricated HNS-controller. Its dimension and weight were measured to be 17.5×10.0×5.30 cm and 141.8 g except for batteries, respectively. --- ----- 81

Figure 3.4.2 (a) A photograph of the *in vitro* evaluation for remote control of the totally implantable stimulator (unpackaged) using the HNS-controller and (b) one of biphasic current pulses generated from the totally implantable stimulator in the PBS solution. ----- 82

Figure 3.4.3 Photographs of a pigeon's turning-left behavior induced by percutaneous stimulation on the FRM region. These photographs show successive time flow for 2.5 seconds. The red circle indicates a percutaneous link that connected the HNS-controller to an electrode inserted into the target region. ----- 83

Figure 3.4.4 Photographs of a turning-left behavior of a pigeon induced by remote neural stimulation control using the HNS-controller. These photographs also show successive time flow for 2.5 seconds. The black wire on the bottom was tied to the pigeon's leg, restraining the pigeon not to run away in open areas. ----- 84

Figure 4.1.1 Photographs of Scotch tape testing on a gold-laminated COP substrate to briefly evaluate the adhesion between gold and COP. ----- 87

Figure 4.1.2 Possible leakage paths in the fabricated COP encapsulation: a COP surface and a COP-COP interface. ----- 90

Figure 4.1.3 SEM images of cross-sections of the COP encapsulation before and after aging. After soaked, delamination was observed in both of the specimens fabricated under lower pressure and higher pressure. ----- 91

Figure 4.1.4 An illustration of a customized optical experimental setup for light transmission tests using thermally laminated COP films. ----- 93

Figure 4.1.5 Captured images of the black and white line patterns and normalized light intensity outcomes along the horizontal displacement: (a) uncovered and covered by (b) a 13- μm -thick bare COP film and themally laminated COP films whose thicknesses were (c) 26 μm , (d) 63 μm , (e) 113 μm , (f) 201 μm , and (g) 376 μm , respectively. ----- 95

Figure 4.1.6 Measured light transmittances of thermally laminated COP films with varying thicknesses. Both light transmittances of the 13- μm -thick bare COP film and the 26- μm -thick thermally laminated COP film were identical to 95.87 %. The light transmittances of the 63- μm -, 113- μm -,

201- μm -, and 376- μm -thick thermally laminated COP films were 94.43, 95.22, 93.65, and 91.69 %, respectively. -----	96
Figure 4.1.7 Calculated MTFs from the light transmission tests. The threshold level (the black dashed line) represents 10 % of MTF of the image captured without a COP film (the intersection at a 47.6 μm line pitch for the 26- μm -thick thermally laminated COP film). -----	97
Figure 4.1.8 Illustrations of potential applications using COP-based optically transparent encapsulation. -----	98
Figure 4.2.1 Detailed description on the reason why an H-bridge circuit is unable to be used for simultaneous stimulation. -----	99
Figure 4.2.2 The grid-shaped and the honeycomb-shaped arrangement of stimulation electrodes controlled by the penta-polar stimulation. -----	100
Figure 4.2.3 More virtual channels created <i>in vitro</i> by the penta-polar stimulation along another direction in two dimensions at the distance from the stimulation electrodes of 150 μm , the optimal distance for virtual channel generation herein. -----	102
Figure 4.3.1 A surface temperature of the implantable camera measured for an hour in continuous operation. -----	103
Figure 4.3.2 Radiation field analysis using the implantable camera to evaluate the angle-dependency of its wireless communication characteristics. ---	105
Figure 4.3.3 Leakage current measurements during accelerated aging. The red and orange lines showed the leakage currents of the elastomer-sealed samples without the epoxy coating. The green and blue lines indicated	

the leakage currents of the samples underwent both the epoxy coating and the elastomer sealing. The threshold level of 1 μ A, expressed as the black dashed line, was set arbitrarily. ----- 106

Figure 4.4.1 Biphasic current pulses generated from the current stimulation ASIC on the HNS-controller, which were measured by varying pulse rates, durations, and amplitudes: the current pulses at the pulse rate of (a) 452.3 Hz and (b) 246.5 Hz, and the current pulse at the duration and the amplitude of (c) 0.010 ms and 0.107 mA, (d) 0.020 ms and 0.107 mA, (e) 0.010 ms and 0.190 mA, and (f) 0.020 ms and 0.190 mA, respectively. ----- 109

Figure 4.4.2 A graph of power transfer efficiency measured by varying a load resistance of a totally implantable stimulator from 56.1 Ω to 120 k Ω . -- ----- 110

Figure 4.5.1 A conceptual view of the suggested totally implantable visual prosthetic system constructed by the integration with the COP-based fabrication, the penta-polar stimulation, the implantable camera, and the handheld remote controller. ----- 113

List of Tables

Table 1.1.1 Pros and cons of conventional substrate materials used for implantable devices, including metal, silicon, ceramic, and polymer. -----	4
Table 1.4.1 Properties of polymer materials used for the fabrication of implantable devices. -----	11
Table 1.4.2 A comparison table between a glasses-mounted camera and an MPDA used in conventional partially implantable visual prosthetic systems. --- -----	16
Table 1.5.1 Objectives and brief descriptions of this dissertation. -----	21
Table 2.2.1 Detailed specifications of the custom-designed penta-polar stimulation ASIC. -----	35
Table 2.2.2 Details on digital protocols of the custom-designed penta-polar stimulation ASIC: (a) a pulse interval and duration setting frame, (b) a channel and amplitude setting frame, (c) a current generator selection code, and (d) an output channel selection code. Bit 18 and Bit 0 meant the most significant bit (MSB) and the least significant bit (LSB), respectively. Prefix ‘CIS’, ‘PI’, ‘DR’, ‘CG’, ‘CH’, ‘A’, and ‘PO’ indicated continuous interleaved sampling, pulse interval, duration, current generator, channel, amplitude, and polarity, respectively. ‘P’ and ‘F’ stood for announcing parity check (even parity in the ASIC) and EOF. -----	37
Table 3.1.1 Electrochemical impedances at 1 kHz of the four channels consisting of	

the COP-based depth-type microprobe. -----	63
Table 3.1.2 Results of the buckling tests: elastic modulus and yield stress. -----	66
Table 3.2.1 Parameters of the five biphasic current pulses (Figure 3.2.2) for verifying the operation of the fabricated penta-polar stimulation ASIC. -----	71
Table 3.2.2 Electrochemical impedances at 1 kHz of the five channels consisting of the COP-based surface-type electrodes. -----	72
Table 3.2.3 A comparison table on a field distribution area ratio of the penta-polar and the mono-polar stimulation between the FEA and the <i>in vitro</i> evaluation. -----	75
Table 4.3.1 Comparison of image acquisition approaches for visual prosthetic systems. -----	105
Table 4.5.1 A comparison table among visual prosthetic systems including the suggested totally implantable visual prosthetic system in this dissertation. -----	116

List of Abbreviations

Abbreviation	Term
CH	Channel
LCP	Liquid crystal polymer
COP	Cyclic olefin polymer
UV	Ultraviolet
SI	Primary somatosensory cortex
IDE	Inter-digitated electrode
FEA	Finite element analysis
ASIC	Application-specific integrated circuit
MPDA	Micro-photodiode array
BLE	Bluetooth Low Energy
SNR	Signal-to-noise ratio
HNS-controller	Handheld neural stimulation controller
PBS	Phosphate buffered saline
DAQ	Data acquisition
AP	Anterior-posterior
ML	Medial-lateral
DV	Dorsal-ventral
DC	Direct current
CMOS	Complementary metal–oxide–semiconductor

Abbreviation	Term
DAC	Digital-to-analog converter
BCG	Biphasic current generator
PWM	Pulse-width modulated (modulation)
EOF	End of a frame
HFSS	High-frequency structure simulator
CAD	Computer aid design
PCB	Printed circuit board
SCCB	Serial camera control bus
TX	Transmitter
RX	Receiver
ACK	Acknowledgement
YUV	Luminance (Y) and chrominance (UV)
UART	Universal asynchronous receiver/transmitter
RSSI	Received signal strength indicator
PA	Power amplifier
FPGA	Field-programmable gate array
LED	Light-emitting diode
REQ	Request
FRM	Formatio reticularis medialis mesencephalic
CSC	Charge storage capacity
SEM	Scanning electron microscope (microscopic)
MTF	Modulation transfer function

◆ Note

Some parts of this dissertation are extracted and adapted from the following publications which were published during the degree course:

- Shim, S., Park, H. Y., Choi, G. J., Shin, H. C., & Kim, S. J. (2019). A Simply Fabricated Neural Probe by Laser Machining of a Thermally Laminated Gold Thin Film on Transparent Cyclic Olefin Polymer. *ACS Omega*, 4(2), 2590–2595.
- Shim, S., & Kim, S. J. (2019, July). A Feasibility Study on Optically Transparent Encapsulation for Implantable Neural Prostheses. In *2019 41st Annual International Conference of the IEEE Engineering in Medicine and Biology Society (EMBC)* (pp. 3754–3757). IEEE.
- Shim, S., Yun, S., Kim, S., Choi, G. J., Baek, C., Jang, J., Jung, Y., Sung, J., Park, J. H., Seo, K., Seo, J. M., Song, Y. K., & Kim, S. J. (2019). A handheld neural stimulation controller for avian navigation guided by remote control. *Bio-Medical Materials and Engineering*, (Preprint), 1–11.

Chapter 1

Introduction

1.1. Visual Prosthetic System

A neural prosthetic system is the clinical application of neuroscience fused with a wide variety of engineering fields, which is concerned with restoring a motor, sensory, or cognitive modality damaged as a result of a disease or an injury [1–8]. Especially a visual prosthetic system, one embodiment of neural prosthetic systems, is intended to treat the partial vision of blind patients by leveraging neural stimulation, which is the purposeful modulation of activities of the nervous system. Such a visual prosthetic system therefore consists of a neural stimulator and peripheral external devices in general [5, 9, 10].

A neural stimulator is a surgically implantable electronic device that stimulates patient's remaining neurons to substitute their damaged functions; as for a visual prosthetic system, the retina, the optic nerve, or the visual cortex of the blind can be targeted for the stimulation [11–19]. In addition, peripheral devices outside the body involve a sensor, a controller, or a processor which helps a neural stimulator to operate using acquired sensory signals, such as images, or directly control the stimulator. For example, in a retinal prosthesis, an external camera is mounted on a pair of glasses and garners images [11, 19, 20]. This external unit processes the images and transmits them to a neural stimulator partly inserted into the eye. Electrical stimuli made from the images by the neural stimulator then flow along electrodes on or under the retina to restore the partial vision of a blind patient.

1.1.1. Current Issues

Several visual prosthetic systems have already been deployed on a

commercial scale based on the abovementioned system configuration nowadays [19–22]. These visual prosthetic systems, especially retinal prostheses or retinal implants, are clinically applied to patients with vision-related retinal diseases, such as retinitis pigmentosa or age-related macular degeneration, and treat them for rehabilitation. Approximately over 250 patients worldwide have received the implantation of the Argus II epi-retinal prosthesis (Second Sight Medical Products, Inc., USA) to date, since it was first medically approved in Europe in 2011 [19]. In Korea, the Argus II device was implanted in blind patients in 2017, for the first time, and the number of such patients is anticipated to be increased [23, 24].

Nevertheless, the problem is that the efficacy of current visual prosthetic systems on the regeneration of patients' vision is limited, for example with retinal prostheses, to simple pattern or character recognition rather than normal color vision with high resolution [25–28]. There are still many issues on improving the performance of a visual prosthetic system to be dealt with, in terms of substrate materials, electrode configurations, external hardware, power supply and data transmission, design and fabrication, etc., as follows [28, 29].

1.1.1.1. Substrate Materials

Electrode fabrication and encapsulation for a visual prosthetic system are two major technical challenges to achieve both the biocompatibility and the long-term reliability of implantable units, which are expected to minimize unsuspected damages to biological tissues and to span more than a decade, respectively [30, 31]. Unless such implantable units remain stable and functional in the body, they might

Table 1.1.1 Pros and cons of conventional substrate materials used for implantable devices, including metal, silicon, ceramic, and polymer.

	Metal	Silicon (electrode)	Ceramic (package)	Polymer
Pros	<ul style="list-style-type: none"> • Hermetic 	<ul style="list-style-type: none"> • Applicable to the semiconductor technology 	<ul style="list-style-type: none"> • Thermally and electrically insulating • Resistant to corrosion 	<ul style="list-style-type: none"> • Flexible • EM* compatible • Applicable to microfabrication
Cons	<ul style="list-style-type: none"> • Bulky • Heavy • Labor-intensive 	<ul style="list-style-type: none"> • Brittle • Rigid • Not bendable 	<ul style="list-style-type: none"> • Brittle • Not bendable 	<ul style="list-style-type: none"> • Relatively not long-term reliable

* Electromagnetic

not only cause the failure of an entire prosthetic system, which leads to a waste of cost and time, but also severely harm the patient’s health. Therefore, to prevent these problems, it is crucial to choose suitable substrate materials for both electrode fabrication and encapsulation.

To date, metal, silicon, ceramic, and polymer have been used in conventional neural prosthetic systems as demonstrated in Table 1.1.1 [15, 19, 31–37]. Commercial neural prosthetic systems, which are medically approved, particularly rely on metal-based electrodes for reliable electrical connections or silicon-based ones with high density as well as metal-based or ceramic-based encapsulation for the hermeticity of implantable units [38–43]. However, metal is bulky, heavy, and labor-intensive in manufacture. Additionally, silicon and ceramic are brittle, rigid, and unbendable. These material properties make them unsuitable especially for visual prosthetic systems, which require more flexible and more

conformable substrates and miniaturized implantable units apart from the long-term reliability in a physiological environment [31, 44]. On the contrary, polymer has outstanding advantages including high flexibility, electromagnetic compatibility, and applicability to microfabrication. Polymer-based electrode fabrication and encapsulation thus are of great interest recently for various implantable devices, even which have a monolithically fabricated or an optically transparent body [27, 31, 45–47]. Nonetheless, the limitation is the insufficient reliability of polymer materials, which has long been questioned due to its degradation resulting from the penetration of moisture and ions in the body [31, 45, 48].

1.1.1.2. Electrode Configurations

In neural prosthetic systems, electrodes are essential components that directly deliver stimuli to target neurons. Especially in visual prosthetic systems, configurations of such electrodes are more significant for precise stimulation with high spatial resolution as well as improved neural interfaces related to electrode contacts to targets, such as the retina, the optic nerve, or the visual cortex [49].

To generate elaborate stimulation patterns, electrodes have advanced to have smaller size and higher density by the help of breakthroughs in microfabrication [30, 49]. These progresses have helped researchers to stimulate dense networks of neurons in a confined space [15, 50, 51], however, it is still challenging to arrange such electrodes to precisely stimulate individual neurons. Electrical crosstalk, the spatial superposition of electric fields among dense electrodes, leads interactions between simultaneous stimuli and degrades the independence of every single

electrode [52–54]. An adequate spacing between adjacent electrodes is required, which causes a limited number of physical electrodes that interferes with precise stimulation, thus the limitation of spatial perception with current visual prosthetic systems occurs [49, 55].

To overcome these limitations, many researchers have proposed structural modification to electrodes and new stimulation paradigms using virtual channels (CHs; these are also expressed as electrode sites or electrodes in this thesis) [56–62]. On the one hand, three-dimensional conformable or embossed structures can be applied to electrodes for closer contacts with targets and effective stimulation [57, 59–62]. On the other hand, virtual channels can be used to provide more delicate stimulation patterns using intermediate areas with large magnitudes of electric fields between physical electrodes, which can be generated by combining simultaneous stimuli supplied from two or more electrodes [54, 56, 58]. Despite these efforts, the effectiveness of these approaches is still insufficient to enhance the spatial resolution using visual prosthetic systems and needs more breakthroughs [49].

1.1.1.3. External Hardware

The use of external hardware in a neural prosthetic system has been regarded as inevitable so far in sensing sensory signals, such as images or sounds, and processing them into electrical signals to control a neural stimulator. However, for example with a cochlear implant, it was reported that some potential users were deterred by the cosmetic appearance of a cochlear implant [63, 64]. This situation might have no difference with that of a visual prosthetic system. As mentioned above,

a conventional visual prosthetic system consists of an implantable neural stimulator and an external camera mounted on a pair of glasses with an inductive link between two coils that enables the transmission of power and data across the skin. Among these elements, a glasses-mounted camera and an inductive link may provide several functional and psychological disadvantages due to their visibility and prominence [65].

First, functional failure of external devices can easily occur as a result of unpredictable damages from the outside. Manufacturers thus recommend using the external devices against vigorous activities, such as running or swimming, but patients are also unable to wear them during several ordinary activities, such as during sleep or in the shower. Moreover, the use of the external devices can invoke cosmetic issues, which can act as a stigma symbol that draws attention to a negative identity [64, 66].

1.1.1.4. Other Issues

In addition to the three major issues above, power supply and data transmission methods also should be considered for improving the performance of a visual prosthetic system. An inductive link, which is constructed between two coils across the skin, has been widely used because of some merits of delivering power and data simultaneously with high power transfer efficiency [67, 68]. However, it is difficult to align the two coils for the higher efficiency, and the external coil of the two may be vulnerable to damages resulting from unpredictable external impacts. Instead of such an inductive link, a rechargeable battery in a neural stimulator and a

commercial wireless communication protocol, such as ZigBee, Bluetooth, or Wi-Fi, can be utilized for power supply and data transmission, respectively [69]. On the other hand, an optical transcutaneous link can be used as well to achieve low-power and high-rate data communication [70].

Another issue can be concerned with design and fabrication of a neural stimulator. Modular design has been widely used in commercial neural prosthetic systems because it is helpful in replacing old parts of a neural stimulator with new ones. On the contrary, monolithic fabrication has different advantages in device miniaturization as well as the prevention of moisture and ions penetration through connections or feedthroughs [45, 47]. The complexity of fabrication process can be also an important point that is closely related to the manufacture cost of an entire prosthetic system.

Other than these issues, surgical placement of electrodes in a visual prosthetic system is one of the key points for improving its performance [71, 72], and there are more issues on stimulation paradigms, neural signal mapping, threshold levels of neurons, coverage, etc. [73–75].

1.2. Suggested Visual Prosthetic System

In this dissertation, overall four of the abovementioned issues, thought to be crucial, are handled selectively, and by extension, a totally implantable visual prosthetic system is suggested as described in Figure 1.2.1. The suggested visual prosthetic system consists of an implantable neural stimulator and an implantable camera as well as an external controller and processor, and it works to stimulate the

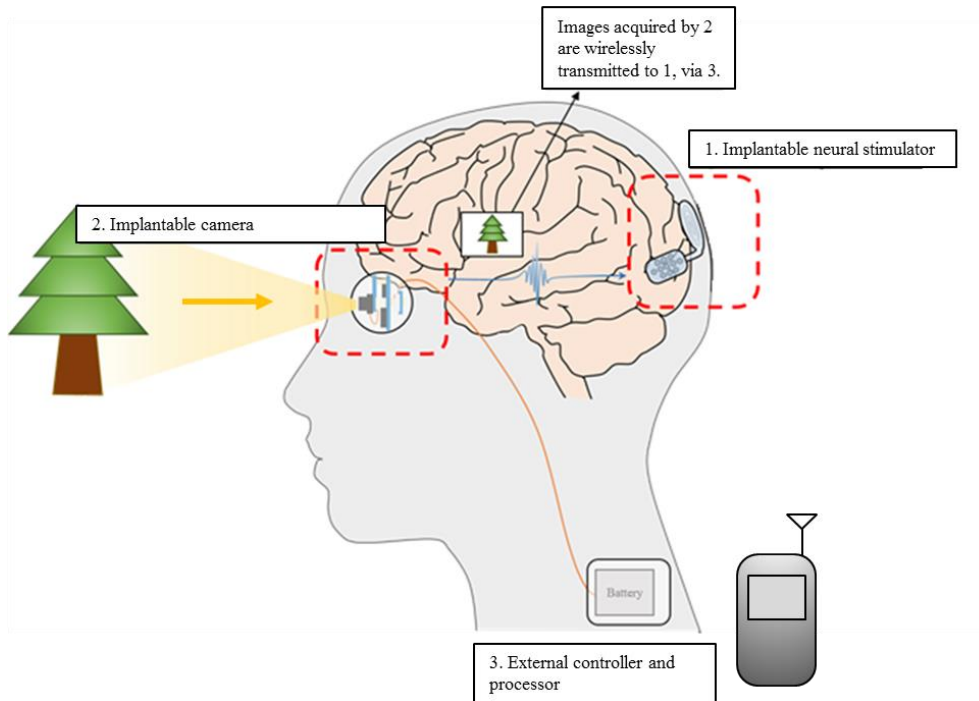


Figure 1.2.1 A conceptual view of the suggested totally implantable visual prosthetic system that consists of an implantable neural stimulator and an implantable camera as well as an external controller and processor.

visual cortex. Images acquired by the implantable camera can be wirelessly transmitted to the neural stimulator, occasionally through the handheld remote controller and processor; the remote controller also can manipulate the stimulator according to user's intentions.

The implantable camera can have the potential to be used for many blind patients generally. However, it could be firstly applied to the blind underwent the enucleation of the eye, caused by trauma, infection, or ocular tumors, like an intraocular prosthesis, which is a passive device that merely helps them to maintain the shape of an eyeball. In addition, these people have only orbital contents intact,

which implies that their visual cortex or optic nerve be stimulated rather than the retina, to restore their partial vision. In this case, because the implantable camera has a merit of obtaining lots of image information using the complete structure of a camera, it can be particularly suitable to stimulate the visual cortex, which features a relatively broad area to be stimulated using a large number of electrodes [76–78].

1.3. Four Motivations

As mentioned above, overall four issues are introduced herein to deal with several crucial issues on a visual prosthetic system among the abovementioned ones and construct the suggested totally implantable visual prosthetic system. The first motivation is to simply fabricate implantable units of a visual prosthetic system, including micro-sized electrodes and a package. An optically transparent polymer material was chosen, and thermal lamination along with laser machining was only used in this fabrication without semiconductor techniques. The second motivation is to overcome a limited number of physical electrodes in a confined space. Multi-polar stimulation was employed to generate more delicate stimulation patterns by combining electrical stimuli supplied from multiple electrode sites at the same time. The third motivation is to develop a new image acquisition strategy for a visual prosthetic system using an implantable camera, and the last one is to realize power supply and data transmission to a neural stimulator without hindering patient's various activities unlike an inductive link. Both of the third and the last motivations can substantially contribute to the development of the suggested totally implantable visual prosthetic system.

1.4. Proposed Approaches

1.4.1. Cyclic Olefin Polymer (COP)

As demonstrated above, polymer is of great interest recently for the development of diverse implantable devices. Most implantable devices based on polymer materials, such as polyimide, parylene-C, or liquid crystal polymer (LCP), have been fabricated by the semiconductor technology including metal deposition and photolithography techniques, especially for metal patterning [79–84]. These techniques provide highly accurate and precise metal patterns on a polymer substrate. Nevertheless, the techniques are also complicated and time-consuming, which can increase the manufacture cost of an entire prosthetic system, because they require masks for photolithography and vacuum for metal deposition as well as huge fabrication facilities.

As an alternative to the techniques, simple fabrication process of an implantable device was herein developed using a sort of optically transparent

Table 1.4.1 Properties of polymer materials used for the fabrication of implantable devices.

	COP (ZeonorFilm)	Polyimide (PI-2525)	Parylene-C (GALXYL)	LCP (Vecstar)
Melting temperature (°C)	-	-	290	280–335
Glass transition temperature (°C)	136–163	>320	-	-
Tensile strength (MPa)	60–70	128	69	240–330
Young’s modulus (GPa)	2.6	2.4	3.2	2–3
Water absorption rate (%)	<0.01	2–3	>0.06	<0.04
Dielectric constant (at 1 MHz)	2.3	3.3	2.95	2.9
Light transmittance (%)	92	~81	~70	<20

polymer materials, named cyclic olefin polymer (COP). COP is an amorphous material that features biocompatibility, low water absorption (<0.01 %), and high light transmission (92 % in a wavelength range of 300 to 1,100 nm), as shown in Table 1.4.1 [85–93]. Because of these advantageous properties, COP has been used in a variety of applications including drug packages, displays, waveguides, and microfluidic devices [89, 90, 94–97].

The developed COP-based fabrication process employed ultraviolet (UV) laser machining after thermal lamination of a gold thin film and a COP substrate. Film-type COP can be leveraged as a substrate of an implantable device for future monolithic integration, both enabling device miniaturization as well as eliminating feedthroughs that may form small gaps through which moisture and ions can penetrate. COP films therefore were used based on thermal lamination, a suitable fabrication procedure using films. Additionally, gold was used as a conducting material because it can easily adhere to COP with no adhesion layer [94]. In addition to such adhesion, due to their different optical properties, gold can be ablated by a UV laser, whereas COP with UV transparency can remain intact [89, 90, 98, 99]. Thereby, a gold thin film thermally laminated on a COP substrate can be selectively micromachined by a UV laser without the semiconductor technology.

The developed COP-based process was firstly applied to fabrication of a depth-type microprobe. To demonstrate electrochemical and mechanical characteristics as well as the functionality of this COP-based microprobe, impedance measurements, buckling tests, and *in vivo* neural signal recording were performed, respectively. An averaged electrochemical impedance of the COP-based microprobe

was characterized in saline solution, and the elastic modulus as well as yield stresses of the COP-based microprobe was measured in relation to its thickness and compared with those of an LCP-based microprobe. Furthermore, the COP-based microprobe was inserted into the primary somatosensory cortex (SI) of a rat to carry out simultaneous multi-channel neural signal recording.

In addition to the microprobe fabrication using COP, its reliability in a physiological environment was estimated as well. This estimation is necessary to the characterization of polymer as a substrate material of an implantable device, because the long-term reliability of polymer is uncertain due to its degradation resulting from the penetration of moisture and ions in the body [31, 45, 48]. Therefore, to show the feasibility of COP encapsulation, this encapsulation was formed by the developed COP-based fabrication process as well, and leakage current measurements were conducted during accelerated aging in saline solution. These measurements involved four customized inter-digitated electrodes (IDEs) in the COP encapsulation, and leakage currents flowing through the IDEs were detected.

1.4.2. Penta-Polar Stimulation

As explained above, many researchers have proposed stimulation strategies using virtual channels to overcome a limited number of physical electrodes in a confined space, which blocks precise stimulation on individual neurons [54, 100–102]. Virtual channels are intermediate areas with large electric field magnitudes between physical electrodes. Such virtual channels can be generated by current steering, which is an approach to combine stimuli supplied from two or more

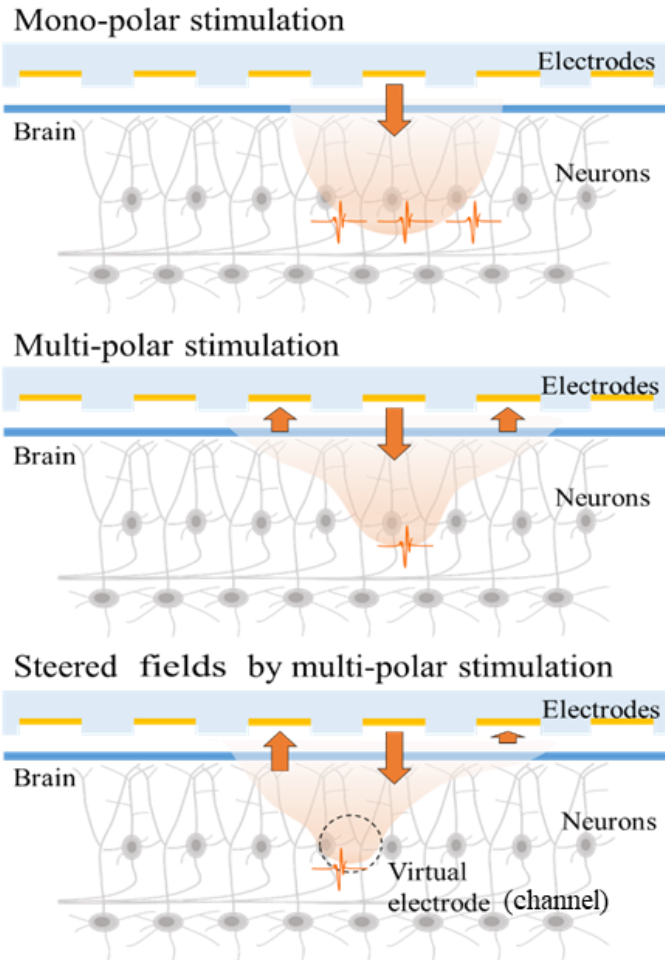


Figure 1.4.1 Schematic diagrams of electric field distribution: mono-polar stimulation (top), multi-polar stimulation (middle), and multi-polar stimulation with current steering (bottom).

adjacent electrodes simultaneously. This approach thereby can modulate the distribution of electric fields made by multi-polar stimulation as shown in Figure 1.4.1.

The feasibility and the effectiveness of virtual channels *in vivo* were verified through clinical trials and animal tests, respectively [103, 104]. In these

researches, virtual channels induced additional pitch perception in adult cochlear implant recipients and effectively altered neural activation patterns in the visual cortex. In spite of these positive results, there have been no studies on how virtual channels are really created in an electrolyte. Therefore, in this study, not only was virtual channel generation aimed to be implemented for more delicate stimulation patterns, but also how virtual channels can be formed *in vitro* was evaluated particularly in two dimensions, where stimulation on the brain or the retina is closely related. Moreover, finite element analysis (FEA) in the same conditions with this *in vitro* evaluation was conducted as well in order to prove the relationship between FEA and *in vitro* evaluation results.

For virtual channel generation, a configuration of stimulation electrodes is important to the spatial distribution of electric fields. Such a configuration in two dimensions can have an arrangement of a grid shape or a honeycomb shape [103, 104]. Among these shapes, the grid-shaped arrangement was chosen because it consists of one center electrode and four peripheral electrodes, which can be driven at the same time with lower power than the honeycomb-shaped configuration with one center electrode and six peripheral electrodes. A new penta-polar stimulation strategy thus was devised with current steering; this penta-polar stimulation can use five electrodes simultaneously and steer electric fields in two dimensions generated by five different output currents.

To realize this virtual channel generation using the penta-polar stimulation, an application-specific integrated circuit (ASIC) for such stimulation and COP-based surface-type electrodes arranged in a cross shape, as the specific portion of a

grid shape, were custom-designed. The effectiveness of the penta-polar stimulation on focusing electric fields, as shown in Figure 1.4.1, was evaluated first to show its effectiveness through comparison with mono-polar stimulation. Furthermore, changes of the electric fields, which indicated steered virtual channels, were estimated from both FEA and *in vitro* evaluation in accordance with an amplitude ratio between stimuli of the two adjacent electrodes and a distance from them. Based on this estimation, the optimum distance at which virtual channels were most effectively generated with the designed ASIC and electrodes was found.

1.4.3. Implantable Camera

There are two external devices in a conventional partially implantable visual prosthetic system, which potentially cause the abovementioned problems of external hardware: a glasses-mounted camera and an external coil placed beside the eye or the ear. To solve the problems, issues of image acquisition approaches including a glasses-mounted camera are dealt with in this section first, and those of

Table 1.4.2 A comparison table between a glasses-mounted camera and an MPDA used in conventional partially implantable visual prosthetic systems.

	Glasses-mounted camera	MPDA
Image sensing area	N/A	3.0×3.0 mm
The maximum number of pixels	N/A	1,600
Tracking objects in accordance with natural eye movements	X (needs more complicated hardware and software)	O

an external coil will be handled in the next section.

Every visual prosthetic system needs an image sensor to transduce optical patterns into electrical signals like photoreceptors of the retina. One widely-used method for this transduction is using a glasses-mounted camera [20, 105, 106]. This glasses-mounted camera captures real-time images, modulates them into stimulation patterns, and transmits the modulated data to a neural stimulator via an inductive link. The glasses-mounted camera can produce sophisticated image data with a variety of sizes, colors, or formats, which can be easily processed. However, the glasses-mounted camera has no function to focus on objects in accordance with natural eye movements because its movements are inevitably synchronized with those of the head rather than the eye; to implement this tracking function, the glasses-mounted camera needs additional complex hardware and software as demonstrated in Table 1.4.2 [107]. Additionally, glasses may elicit a little discomfort to patients as well as hindering several ordinary activities such as sleep, shower, or running [65].

Another image acquisition method utilizes a micro-photodiode array (MPDA) implanted in the sub-retinal region [106, 108, 109]. Such an MPDA is integrated with stimulation circuits in general, thus it can generate electrical stimuli directly converted from incident light. In contrast to the glasses-mounted camera, the MPDA can track objects along with natural eye movements and requires no wearing unit like glasses. However, the MPDA without the complete structure of a camera provides insufficient information on images, which may contain only the intensity of incident light. Moreover, because the MPDA needs to be integrated with stimulation circuits, the number of photodiodes in one array could be limited

spatially, which leads to low resolution and lacking information of images as well.

To overcome the limitations of both the glass-mounted camera and the MPDA, a new image acquisition approach using an implantable camera is presented herein. This implantable camera has distinct advantages in that it can enable blind patients to perform several ordinary activities while seeing objects in accordance with their eye movements. These advantages are impossible to be accomplished by the glasses-mounted camera. In addition, compared with the MPDA, the implantable camera also can obtain a variety of image information using the complete camera structure.

With these merits, the implantable camera was developed as a miniaturized wireless camera coated with a biocompatible epoxy and sealed in a spherical form using a medical-grade silicone elastomer to be implanted in the eye. For low-power operation in the body, current consumption of the implantable camera was considered, thus a low-power image sensor and Bluetooth Low Energy (BLE) communication were used. The functionality of the implantable camera was evaluated by wireless image acquisition that displayed a processed black and white image. Furthermore, signal-to-noise ratio (SNR) measurements were carried out while the implantable camera was covered by an 8-mm-thick biological medium to mimic an *in vivo* environment.

1.4.4. Handheld Remote Controller

From now on, an external coil in a conventional visual prosthetic system is handled as mentioned in the previous section.

An external coil attached on the body is connected to a controller and processor through a wire to stably deliver power and data to a neural stimulator. However, this also makes the external coil vulnerable to the common problems caused by external hardware, including functional failure due to external damages, unavailability during sleep, in the shower, or while running or swimming, and cosmetic issues. To solve the problems of the external coil, a totally implantable neural stimulation system controlled by a handheld remote controller is proposed.

The proposed neural stimulation system consists of a handheld remote controller and a totally implantable stimulator. This totally implantable stimulator is integrated with a stimulation circuit, a wireless transceiver, and a rechargeable battery connected to a charger. Receiving control signals wirelessly sent from the handheld remote controller, the totally implantable stimulator delivers electrical stimuli to electrodes, for instance, inserted into the brain. This thesis focuses on the handheld remote controller (referred to as an HNS-controller (handheld neural stimulation controller), henceforth), which the author contributed more to the design and fabrication.

To build a remote controller for neural stimulation, handheld and user-friendly interfaces are required so that it can be driven by users easily under various circumstances. Additionally, to have these interfaces, low-power but relatively long-range wireless communication is needed. To achieve these requirements, ZigBee was chosen herein as the wireless communication protocol between the HNS-controller and the totally implantable stimulator. Not only does ZigBee consume lower power than Wi-Fi, but also it can transmit data for a longer distance (up to 100 m in practice)

than Bluetooth [110, 111]. Owing to the use of ZigBee, the HNS-controller became handheld by operating with batteries. Furthermore, the HNS-controller had gamepad-like design comprised of simple switches to have user-friendly interfaces. The functionality of the HNS-controller was evaluated *in vivo*, through percutaneous stimulation and remote neural stimulation control, as well as *in vitro*. These evaluations were conducted especially for avian navigation, because the proposed totally implantable and remotely controlled neural stimulation system might be the most suitable for navigating the location of a bird, which can fly a long distance in open areas. Results of both *in vivo* experiments were then compared in order to verify the feasibility of remote control of neural stimulation using the HNS-controller.

1.5. Objectives of this Dissertation

This dissertation addresses a study for developing a totally implantable visual prosthetic system with four motivations: 1) simple fabrication of implantable electrodes and package for a neural stimulator based on polymer without semiconductor techniques, 2) multi-polar stimulation for virtual channel generation to overcome a limited number of physical electrodes in a confined space, 3) a new image acquisition strategy using an implantable camera, and 4) power supply as well as data transmission to a neural stimulator without hindering patient's various activities (Table 1.5.1).

First, simple fabrication process of an implantable device is developed based on advantageous characteristics of COP without masks, vacuum, and huge fabrication facilities. The developed COP-based process can be used in fabrication

of a depth-type microprobe or surface-type electrodes as well as encapsulation of an implantable device.

Second, penta-polar stimulation is realized using a custom-designed ASIC to produce virtual channels for more elaborate stimulation patterns. The penta-polar stimulation is effective in focusing electric fields when compared with mono-polar stimulation. Furthermore, virtual channels can be created by the penta-polar stimulation with current steering especially in two dimensions.

Third, an implantable camera is suggested and fabricated as a new image acquisition approach for a visual prosthetic system. The implantable camera can

Table 1.5.1 Objectives and brief descriptions of this dissertation.

Goal	Motivation	Design	Fabrication	Evaluation
A neural stimulator	1. Simple fabrication of an implantable device without semiconductor techniques	<ul style="list-style-type: none"> • Thermal lamination of a gold thin film on a COP substrate • UV laser machining for patterning 	• A depth-type microprobe and COP encapsulation using the developed COP-based fabrication process	<ul style="list-style-type: none"> • Impedance measurements • Buckling tests • Neural signal recording • Accelerated aging tests
	2. Multi-polar stimulation for virtual channel generation to overcome the limitation of physical electrodes	• A penta-polar stimulation ASIC with five current generators	• Surface-type electrodes using the developed COP-based fabrication process	• FEA and <i>in vitro</i> evaluation of focused as well as steered electric field distribution
A totally implantable visual prosthetic system	3. A new image acquisition strategy for a totally implantable visual prosthetic system	• A miniaturized wireless camera with a low-power image sensor and BLE wireless communication	<ul style="list-style-type: none"> • Biocompatible epoxy coating • Medical-grade silicone elastomer sealing 	<ul style="list-style-type: none"> • Wireless image acquisition • SNR measurements
		4. power supply and data transmission to a neural stimulator without hindering patient's activities	<ul style="list-style-type: none"> • Multiple functions for a totally implantable neural stimulation system • Handheld and user-friendly interfaces 	<ul style="list-style-type: none"> • An HNS-controller for remote control of neural stimulation

obtain a variety of image information while focusing on objects in accordance with natural eye movements. The implantable camera also has a merit in that it can provide blind patients with benefits to perform several ordinary activities.

Lastly, a totally implantable neural stimulation system controlled by a handheld remote controller is presented. The handheld remote controller can control a neural stimulator powered by a rechargeable battery through ZigBee wireless communication. Its handheld and user-friendly interfaces can make it easy to use the remote controller under various circumstances.

Chapter 2

Materials and Methods

2.1. COP-Based Fabrication and Encapsulation

2.1.1. Overview

Based on several advantageous features of COP, simple fabrication process of an implantable device was developed and firstly applied to fabrication of a depth-type microprobe. This COP-based microprobe underwent impedance measurements, buckling tests, and *in vivo* neural signal recording to evaluate its electrochemical and mechanical characteristics as well as functionality, respectively. Furthermore, to estimate a lifetime of COP encapsulation fabricated by the developed process, leakage current measurements were performed during accelerated aging in a physiological environment. These measurements were aimed to show the feasibility of the encapsulation using COP as well.

2.1.2. Simple Fabrication Process

The developed simple fabrication process using COP, which was applied to the microprobe fabrication, is schematically illustrated in Figure 2.1.1. Both COP films with low and high glass transition temperature (T_g) (ZF14 and ZF16; a T_g of 136 and 163 °C, respectively, Zeon, Co., Japan) were used in the developed fabrication process with multiple layers; these COP films, provided by the vendor, were available in diverse thicknesses ranging from 13 to 188 μm . First, a high- T_g COP film served as a substrate of a microprobe (Figure 2.1.1(a)). As depicted in Figure 2.1.1(b), this COP substrate was thermally laminated with a gold thin film (5.5 cm \times 3.5 cm \times 100 nm, Hanil Gold Leaf, Co., Korea) using a heating press (model 4122; process conditions of 235 °C, 5.09 MPa, and 3 minutes, Carver, USA).

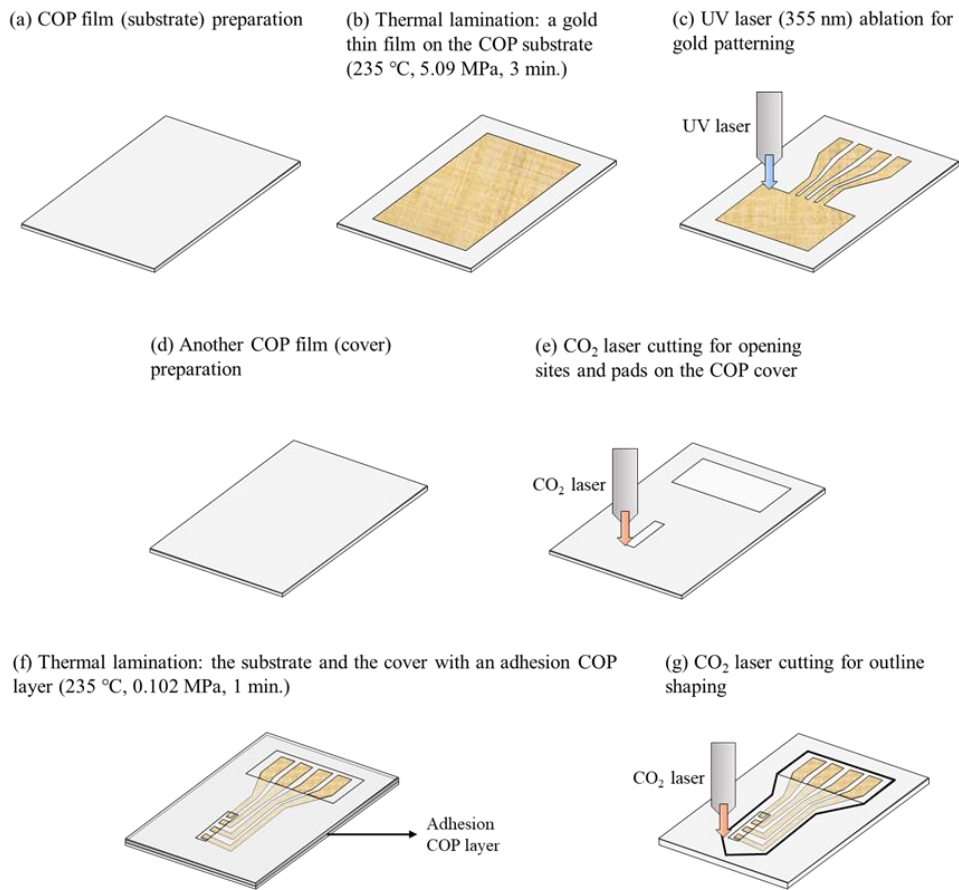


Figure 2.1.1 Simple fabrication process of a depth-type microprobe based on COP consisting of seven steps: (a) preparation of a COP film as a substrate, (b) thermal lamination of a gold thin film on the COP substrate, (c) UV laser ablation for gold patterning, (d) preparation of another COP film as a cover, (e) CO₂ laser cutting to open electrode sites and connection pads on the COP cover, (f) thermal lamination of the substrate and the cover with an adhesion COP layer between them, and (g) CO₂ laser cutting to shape an outline of a depth-type microprobe.

After this thermal lamination, UV laser (Samurai system; a wavelength of 355 nm, DPSS Lasers, Inc., USA) micropatterning was performed on the gold-laminated

substrate as shown in Figure 2.1.1(c). The gold thin film thermally laminated on the COP substrate thereby was selectively micromachined by the UV laser with no semiconductor techniques. In the meantime, another high- T_g COP film was prepared as a cover, whose thickness was 13 μm (Figure 2.1.1(d)). This COP cover was partially cut by a CO_2 laser (VLS6.60, Universal Laser Systems, Inc., USA) with a wavelength of 10.6 μm , where COP loses its transparency [89, 90]. This CO_2 laser cutting opened electrode sites (also called as channels, henceforth) and connection pads (Figure 2.1.1(e)). Subsequently, the gold-patterned substrate and the partially cut cover were laminated using the heating press (with process conditions of 235 $^\circ\text{C}$, 0.102 MPa, and 1 minute) with a 13- μm -thick low- T_g COP film between them (Figure 2.1.1(f)); this low- T_g COP film, which can diffuse easier than a high- T_g one at the same temperature, was partially cut by the CO_2 laser as well and used as an adhesion layer for strong bonding between the substrate and the cover. Finally, the CO_2 laser cut the overall laminated COP structure to shape an outline of a depth-type microprobe, as described in Figure 2.1.1(g). In this outline shaping procedure, the CO_2 laser and the laminated structure were precisely aligned using an additional layer placed under the structure.

2.1.3. Depth-Type Microprobe

2.1.3.1. Design

Figure 2.1.2 presents a COP-based microprobe that was designed to become depth-type with four different channels for simultaneous multi-channel neural signal recording. Each channel had a geometrical surface area of 100×100

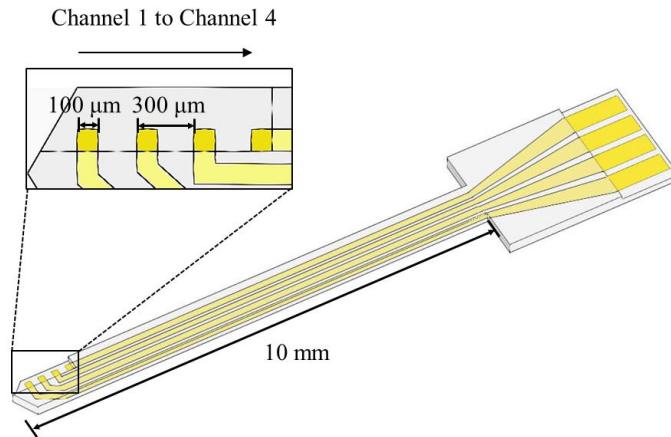


Figure 2.1.2 A schematically drawn COP-based depth-type microprobe with four different channels having an individual geometrical surface area of $100 \times 100 \mu\text{m}$ and with a shank length of 10 mm.

μm . Each spacing between two adjacent channels was $300 \mu\text{m}$, so that neural signals recorded *in vivo* could be clearly distinguished. In addition, the designed depth-type microprobe had a shank length of 10 mm; this shank length was regarded as the minimum probe length required to be inserted in the brain [112].

2.1.3.2. Characterization

To characterize the COP-based depth-type microprobe, its electrochemical impedance was measured first in phosphate buffered saline (PBS) solution (Gibco #10010, Invitrogen Life Technologies, USA) using an impedance analyzer (SI 1287 and SI 1260, Solartron Analytical, U.K.). For this measurement, a three-electrode arrangement with an Ag/AgCl reference electrode and a Pt mesh counter electrode was used as depicted in Figure 2.1.3. An impedance magnitude of each channel was

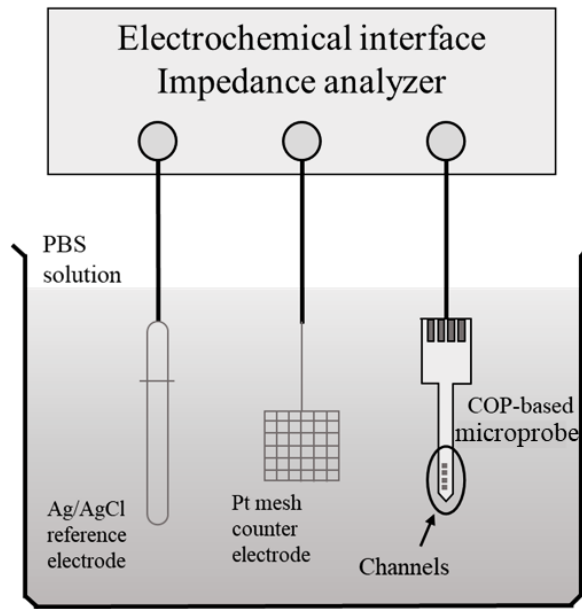


Figure 2.1.3 A three-electrode arrangement setup of an electrochemical impedance measurement using the COP-based depth-type microprobe.

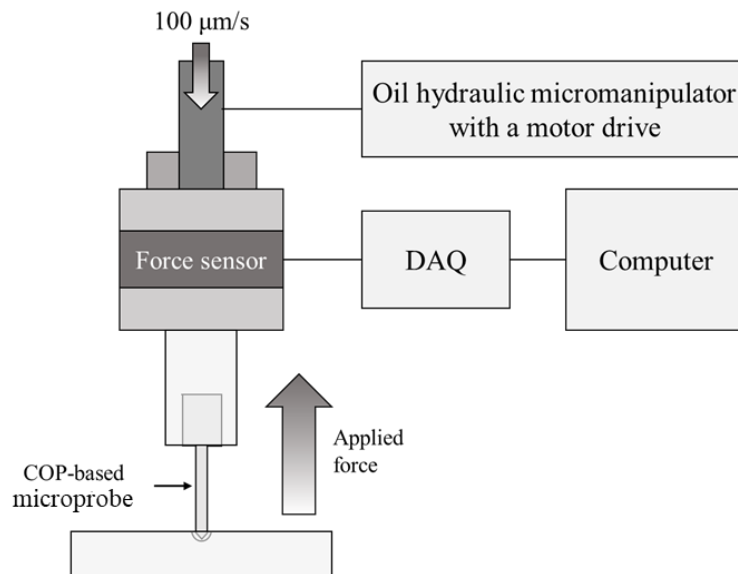


Figure 2.1.4 A conceptual diagram of a buckling test to measure mechanical characteristics of the COP-based depth-type microprobe.

measured over a frequency range of 1 Hz to 100 kHz, while a root-mean-square amplitude of a sinusoidal input voltage was 10 mV without an offset.

In addition, to measure certain mechanical characteristics corresponding to stiffness of the COP-based depth-type microprobe, buckling tests were performed as described in Figure 2.1.4. One side of the microprobe was fixed to a force sensor with a data acquisition (DAQ) unit (Nano17, ATI Industrial Automation, Inc., USA), and the other side was pinned vertically to an acrylic plate placed on the bottom. Using a single-axis oil hydraulic micromanipulator with a motor drive (MO-81, Narishige, Japan), the force sensor, connected to them, moved downward at a speed of 100 $\mu\text{m/s}$. While the force sensor was moving, the force exerted on the microprobe against the movement was monitored.

From this buckling test, elastic modulus of a microprobe can be calculated using the Euler buckling load (2.1) and the area moment of inertia (2.2) with measured forces as follows,

$$F = \frac{\pi^2 EI}{(KL)^2} \quad (2.1)$$

and

$$I = \frac{1}{12} wh^3, \quad (2.2)$$

respectively, where F is the buckling load (the critical force that a specimen can endure without buckling), E is the elastic modulus, I is the smallest area moment of inertia of a cross-section of the column, K is the column effective length factor (0.7071 for the column whose one end is fixed and the other end is pinned), L is the column length, w is the width of the cross-section, and h is the thickness of the cross-

section [83, 84, 113, 114].

With results of the buckling tests, the elastic modulus depending on a thickness of the COP-based depth-type microprobe (differently set to be 50, 100, and 200 μm , respectively) was investigated. To compare with other materials, the buckling tests were also performed on a tungsten rod with a diameter of 200 μm (AM Systems, USA) and LCP-based microprobes with the identical dimensions to a 100- μm -thick COP-based microprobe.

2.1.3.3. *In Vivo* Neural Signal Recording

A rat in this experiment, collaborated by the Prof. Shin, H. C.'s laboratory in Hallym University, was anesthetized using a mixture of Zoletil 50 (40 mg/kg, Virbac S.A., France) and Rompun (10 mg/kg, Bayer, Germany) and fixed on a stereotaxic apparatus (Stereotaxic Model 1404, David Kopf Instruments, USA). The COP-based depth-type microprobe with a thickness of 100 μm was inserted into the left SI region (AP: -3.0 mm, ML: 5.0 mm, DV: 2.5 mm) of the rat. A stainless-steel screw was placed on its forehead as a reference. Neural signals evoked in the left SI region against physical whisker stimulation were measured through an amplifier (Model 3500, A-M Systems, USA) and a DAQ unit (Micro1401-3, Cambridge Electronic Design, Ltd., U.K.). A commercial connector (Molex, LLC., USA) and header pins were used to connect these devices and the 100- μm -thick COP-based depth-type microprobe. For accurate measurements, this experiment was repeatedly performed with a specific stimulation cycle (30-second standby, 30-second right whisker stimulation, 30-second standby, and 30-second left whisker stimulation). All

animals were treated in accordance with the animal research guidelines of Seoul National University and Hallym University (Hallym2016-49).

2.1.4. COP Encapsulation

The reliability of the COP encapsulation fabricated by the developed process was characterized through *in vitro* accelerated aging tests in 75 °C saline solution. These tests involved four customized IDEs, and leakage currents flowing through each of these IDEs were measured.

As illustrated in Figure 2.1.5, the IDEs for the leakage current measurements were fabricated based on the developed process using thermal lamination and two kinds of laser machining. In this case, both 100- μm -thick COP

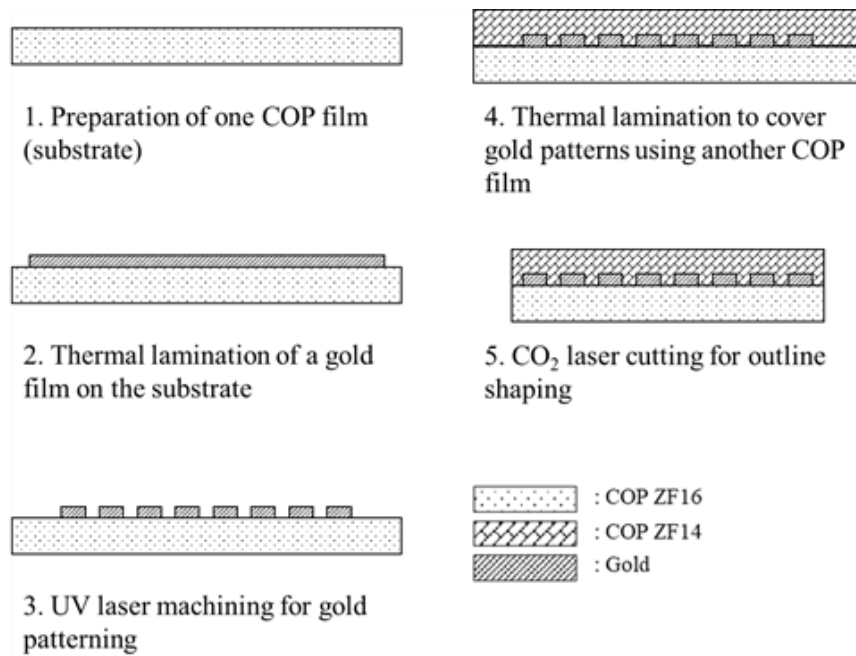


Figure 2.1.5 Fabrication procedures of IDEs on a COP film by the developed process.

films with low and high T_g were used. A COP film with high T_g served as a substrate of the IDEs. This COP substrate was thermally laminated with a gold thin film (5.5 cm×3.5 cm×100 nm, Hanil Gold Leaf, Co., Korea) using the heating press, which was the same with the microprobe fabrication. After the thermal lamination, the UV laser machining was applied to patterning the IDEs on the gold-laminated COP substrate. A width and a spacing of each IDE were both customized at 100 μm , and interconnection lines between the IDEs were designed to be 200- μm -wide. Subsequently, the gold-patterned COP substrate was covered with a low- T_g COP film by thermal lamination. In this procedure, encapsulated samples were divided into two groups according to lamination pressure exerted, to find effects of the pressure on the reliability of this COP encapsulation. One sample was fabricated

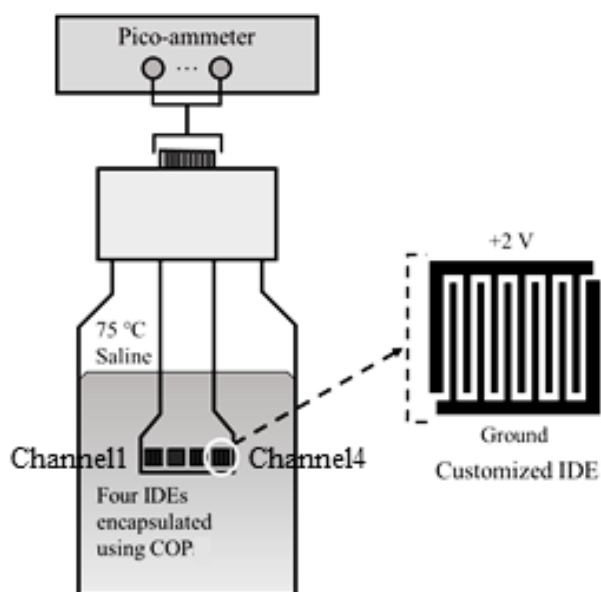


Figure 2.1.6 A diagram illustrating leakage current measurements of four IDEs in the COP encapsulation during accelerated aging in 75 °C saline solution.

with process conditions of 235 °C, 0.051 MPa, and 40 seconds. The other sample was formed with process conditions of 235 °C, 0.509 MPa, and 40 seconds, which had higher pressure than that of the former process conditions. Finally, the CO₂ laser served to cut the overall laminated structures to shape an outline of the COP encapsulation.

2.1.4.1. *In Vitro* Reliability Test

To estimate the reliability of the fabricated COP encapsulation in a physiological environment, the IDEs underwent the leakage current measurements during accelerated aging. As shown in Figure 2.1.6, the COP encapsulation consisted of four customized IDEs to measure the leakage currents flowing at each position. These IDEs were soaked in saline solution to detect the penetration of moisture and ions through the COP encapsulation. For accelerating the aging of the COP encapsulation, it was placed into a bottle with PBS solution (Gibco #10010, Invitrogen Life Technologies, USA) and then put into a forced convection oven heated to 75 °C. During these accelerated aging tests, a DC (direct current) bias at a voltage of 2 V was regularly applied between the IDEs, and the leakage currents were measured using a pico-ammeter (Model 6485, Keithley Instruments, Inc., USA). The leakage current measurements were automated using a LabView-based program and a high-density switch system (Keithley 7001). One measurement of each IDE was conducted 100 times, and the recorded data from this measurement were averaged.

2.2. Penta-Polar Stimulation

2.2.1. Overview

To realize penta-polar stimulation for virtual channel generation, an ASIC that can supply five different currents at the same time was custom-designed, and surface-type electrodes were fabricated by the developed COP-based process. All assessments were carried out through both FEA and *in vitro* evaluation. The effectiveness of the penta-polar stimulation was evaluated by focusing electric fields, compared with that of mono-polar stimulation. Subsequently, changes of the electric field distribution using the penta-polar stimulation were examined in accordance with an amplitude ratio between stimuli of the two adjacent electrodes and a distance from them.

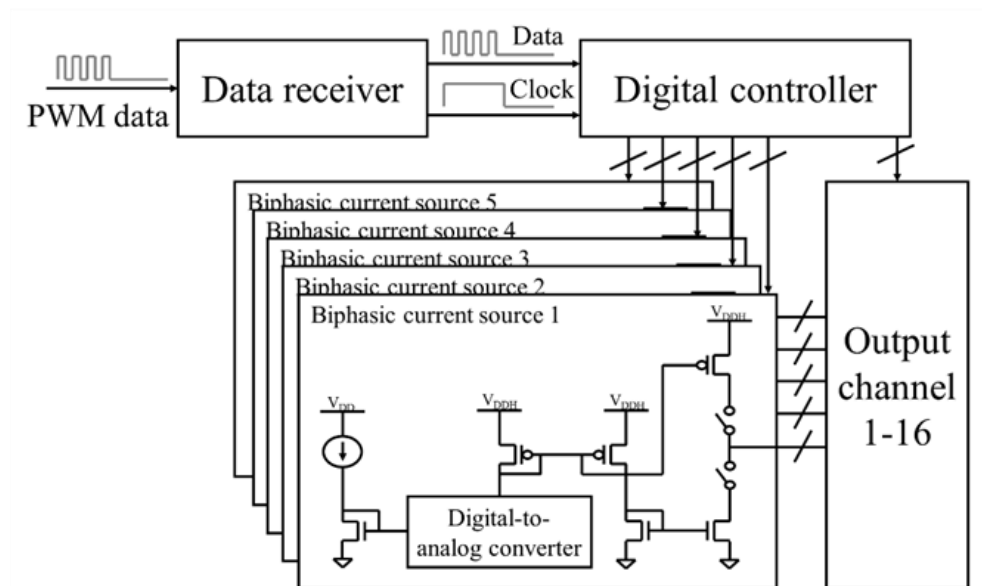


Figure 2.2.1 A circuit block diagram of the custom-designed penta-polar stimulation ASIC.

2.2.2. Design and Fabrication

2.2.2.1. Integrated Circuit (IC) Design

As described in Figure 2.2.1, the penta-polar stimulation ASIC, custom-designed using the AMS 0.35 μm high-voltage CMOS process, consisted of five biphasic current sources and 16 output channels. Each biphasic current source comprised a current reference, a digital-to-analog converter (DAC), and a biphasic current generator (BCG). The current reference was designed to supply a temperature-invariant current of 10 μA , which is an acceptable current level for neural stimulation [30]. This reference current was then multiplied by the DAC that exploited a series of current mirrors whose sizes were differentiated exponentially; by entering digital inputs to the DAC, a level of the multiplied current could be easily varied. Subsequently, the multiplied current flowed through the BCG to become biphasic, which is required to maintain charge balances *in vivo* not to damage neurons during stimulation [30]. Each of the BCGs was devised not to share

Table 2.2.1 Detailed specifications of the custom-designed penta-polar stimulation ASIC.

Process	AMS 0.35 μm high-voltage CMOS	
Die size (mm)	4.5 \times 2.4	
Operating voltage (V)	3.3–9	
Stimulation parameters	Amplitude (mA)	0.01–1.00
	Duration (ms)	0.05–3.20
	Pulse interval (ms)	0.80–51.2

the reference of the penta-polar stimulation ASIC, unlike an H-bridge widely used in conventional stimulation circuits [54]. Thereby, each biphasic current pulse for the penta-polar stimulation was supplied separately from independent sources so as not to interact with other pulses output at the same time; if H-bridges were used for this simultaneous stimulation, every biphasic current pulse would be summed together and divided by a resistance ratio between each output channel and a reference of a stimulation circuit because all H-bridges share the same reference. The five independent biphasic current pulses produced by each of the sources then flowed to five of the 16 output channels, which were controlled by a digital controller in the ASIC.

To modulate and control parameters, such as amplitudes, durations, or pulse intervals (periods), of biphasic current pulses, the penta-polar stimulation ASIC received pulse-width modulated (PWM) data carried by a frequency of 6.25 MHz. A frequency of 6.25 MHz was used to obtain intended ranges of the pulse parameters, such as durations and pulse intervals, shown in Table 2.2.1; this frequency was adjustable within a range of 1 to 10 MHz for expanded uses while varying the parameter ranges. These PWM data were transferred to a data receiver and a digital controller in the ASIC. The data receiver consisted of an inverted Schmitt trigger as well as a delaying circuit thus enveloped the PWM data carried by the 6.25-MHz frequency to be used as a clock signal, which was needed for operating the digital controller. Taking in the PWM data along with the clock signal, the digital controller counted the number of pulses in one period of the data (0–3: a bit of ‘0’, 4–7: the end of a frame (EOF), 8–11: a bit of ‘1’, 12–15: an error,

Table 2.2.2 Details on digital protocols of the custom-designed penta-polar stimulation ASIC: (a) a pulse interval and duration setting frame, (b) a channel and amplitude setting frame, (c) a current generator selection code, and (d) an output channel selection code. Bit 18 and Bit 0 meant the most significant bit (MSB) and the least significant bit (LSB), respectively. Prefix ‘CIS’, ‘PI’, ‘DR’, ‘CG’, ‘CH’, ‘A’, and ‘PO’ indicated continuous interleaved sampling, pulse interval, duration, current generator, channel, amplitude, and polarity, respectively. ‘P’ and ‘F’ stood for announcing parity check (even parity in the ASIC) and EOF.

(a)

Bit 18	Bit 17	Bit 16	Bit 15	Bit 14	Bit 13	Bit 12	Bit 11	Bit 10	Bit 9	Bit 8	Bit 7	Bit 6	Bit 5	Bit 4	Bit 3	Bit 2	Bit 1	Bit 0	F
0	CIS	X	X	X	PI	PI	PI	PI	PI	PI	DR	DR	DR	DR	DR	DR	X	P	F

CIS: continuous interleaved sampling / PI: pulse interval / DR: duration / P: parity (even) / F: end of a frame

(b)

Bit 18	Bit 17	Bit 16	Bit 15	Bit 14	Bit 13	Bit 12	Bit 11	Bit 10	Bit 9	Bit 8	Bit 7	Bit 6	Bit 5	Bit 4	Bit 3	Bit 2	Bit 1	Bit 0	F
1	X	CG	CG	CG	CH	CH	CH	CH	A	A	A	A	A	A	A	A	PO	P	F

CG: current generator / CH: channel / A: amplitude / PO: polarity / P: parity (even) / F: end of a frame

(c)

CG[2:0]	Biphasic current generator
001	Biphasic current generator 1
010	Biphasic current generator 2
011	Biphasic current generator 3
100	Biphasic current generator 4
101	Biphasic current generator 5
else	X

(d)

CH[3:0]	Channel
0000–1111	Channel 1–16

- CIS: a CIS strategy on (1) and off (0)
- On/off for continuous stimulation (not the CIS strategy)
 - Off: all 18 bits of zero
 - On: all 17 bits of one except Bit 0

respectively), and it demodulated them into corresponding bit streams of a frame as demonstrated in Table 2.2.2. Using these bit streams, the digital controller controlled whole functions of the ASIC: changing the parameters of five biphasic current pulses by manipulating the DAC as well as the BCG and activating the output channels

where the pulses were to be supplied.

All analog parts in the penta-polar stimulation ASIC were designed and simulated using the Virtuoso of Cadence, and all digital parts were realized and tested using the Synopsys tools. Details of the specifications of the penta-polar stimulation ASIC are filled in Table 2.2.1 as well. The ASIC operated under a voltage range of 3.3 to 9 V, and after layout, the ASIC occupied an area of 4.5×2.4 mm.

2.2.2.2. Surface-Type Electrode Fabrication

To test the operation of the penta-polar stimulation ASIC and verify spatial electric field distribution created by the penta-polar stimulation, surface-type stimulation electrodes with five channels (electrode sites) arranged in a cross shape were designed with an individual diameter of 450 μm and a center-to-center spacing

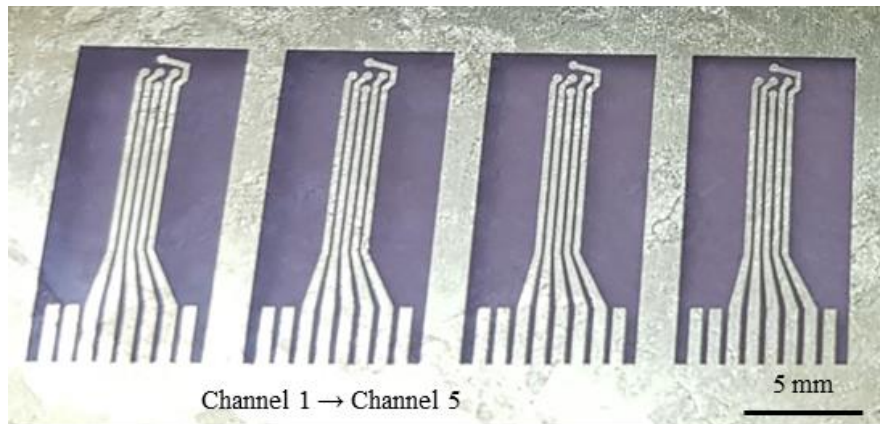


Figure 2.2.2 Micropatterned gold lines on a COP substrate by the developed fabrication process. These surface-type electrodes had five electrode sites, noted as channels, with an individual diameter of 450 μm and a center-to-center spacing of 800 μm .

of 800 μm , as depicted in Figure 2.2.2; the following references were used to determine these dimensions because the references showed neural activation patterns altered by current steering *in vivo* using electrodes with similar dimensions [58, 104, 115]. The surface-type electrodes were fabricated by the same procedures of the developed COP-based simple fabrication process explained in the previous section. A conducting material for the sites was 100-nm-thick gold, and a substrate material was 50- μm -thick COP.

2.2.3. Evaluations

A simple finite element model was constructed to simulate the spatial electric field distribution formed by the penta-polar stimulation. The HFSS (high-frequency structure simulator) from ANSYS was utilized for this FEA. The same surface-type electrodes were three-dimensionally modeled by a CAD tool using the properties of COP with gold, and an ambient condition around the electrodes was filled with saline solution, as an electrolyte, to mimic an *in vivo* environment (Figure 2.2.3(a)).

In addition to the FEA, an *in vitro* evaluation setup was built to be similar to that of the FEA as depicted in Figure 2.2.3(b). As mentioned above, the surface-type stimulation electrodes were fabricated using a COP and a thin gold film by the thermal lamination and the two kinds of laser machining. Measurements were conducted in PBS solution (Gibco #10010, Invitrogen Life Technologies, USA). Unlike the FEA, recording electrodes were necessary *in vitro* evaluation. These recording electrodes were made to be an 8 \times 5 array on a gold-plated FR-4 printed

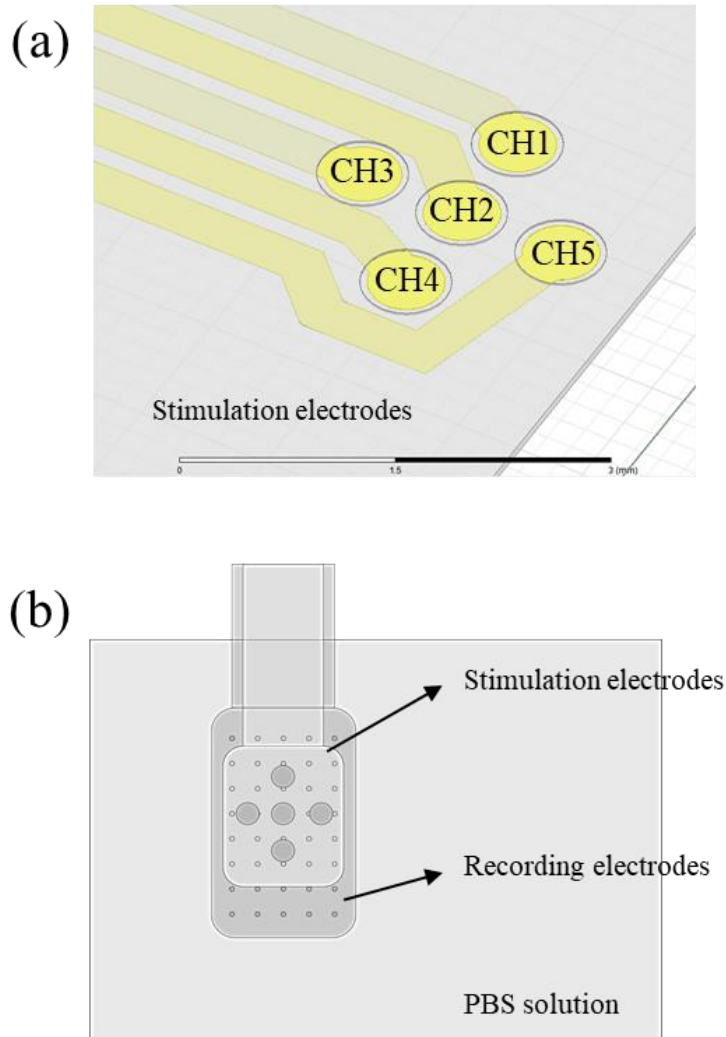


Figure 2.2.3 Evaluation setups for (a) the FEA and (b) the *in vitro* evaluation to estimate the spatial electric field distribution formed by the penta-polar stimulation.

circuit board (PCB). The recording electrodes featured an individual diameter of 75 μm and a center-to-center spacing of 500 μm .

From the measurements *in vitro*, electric potentials were garnered using an oscilloscope (DPO4034, Tektronix, Inc., USA). Therefore, in order to prove the relationship between the FEA and the *in vitro* evaluation, the measured electric

potentials should be converted into magnitudes of electric fields by (2.3):

$$E = |-\nabla V|, \quad (2.3)$$

where E is the electric field magnitude and V is the electric potential; thereby the spatial electric field distribution was obtained.

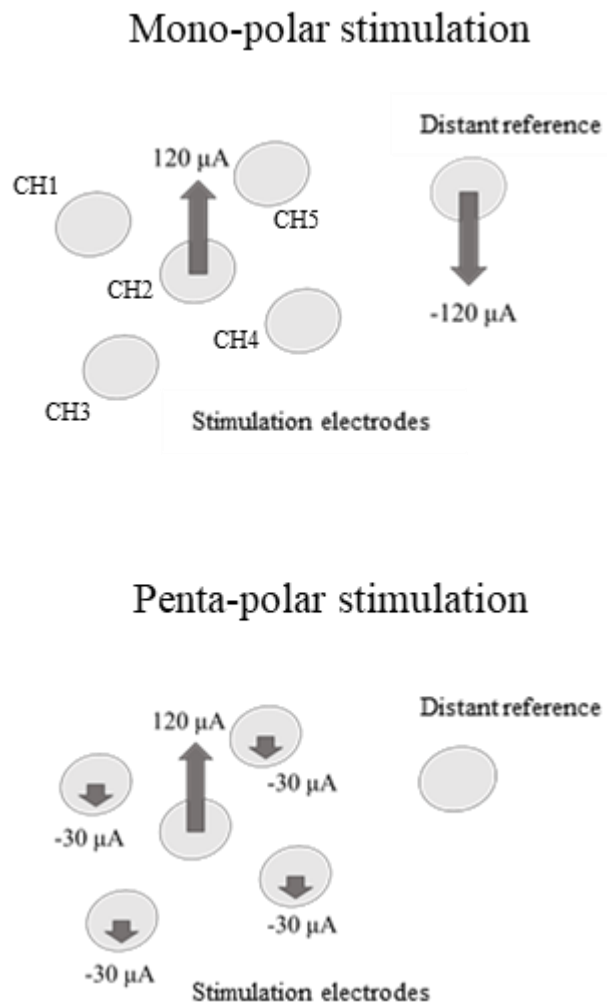


Figure 2.2.4 Schematic diagrams showing configurations of mono-polar (top) and penta-polar stimulation (bottom) to estimate the effectiveness on focusing electric fields generated by the penta-polar stimulation.

2.2.3.1. Focused Electric Field Measurement

In both the FEA and the *in vitro* evaluation, the effectiveness of the penta-polar stimulation on focusing electric fields was evaluated by comparing with mono-polar stimulation, prior to virtual channel generation, as described in Figure 2.2.4. Electric field magnitudes were simulated and measured, respectively, at a distance from the stimulation electrodes of 100 μm . In mono-polar stimulation, current pulses with an amplitude of 120 μA were supplied from the center electrode and flowed to the distant reference. By contrast, in penta-polar stimulation, current pulses with the same amplitude was supplied from the center electrode and divided into four to flow to the peripheral electrodes, respectively.

2.2.3.2. Steered Electric Field Measurement

Subsequently, spatial changes of the electric field distribution while varying an amplitude ratio between stimuli of the two adjacent stimulation electrodes

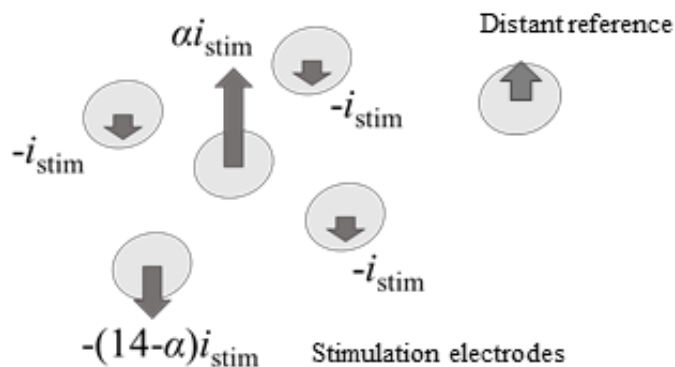


Figure 2.2.5 An illustration that depicts the configuration of the penta-polar stimulation with current steering for virtual channel generation.

were also estimated to localize virtual channels. This estimation was conducted at the distances of 13, 50, 100, 150, 200, and 250 μm , respectively. The amplitude ratio of the stimuli was varied as described in Figure 2.2.5. The amplitude of the fundamental current i_{stim} was set to be 10 μA , and the amplitude ratio coefficient α was changed to be 1, 3, 5, 7, 9, 11, and 13, respectively. After simulating and measuring electric field magnitudes, the weighted centroids of the magnitudes, which were considered as virtual channels, from both of the FEA and the *in vitro* evaluation results were plotted as neural activation patterns on the visual cortex evoked by current steering were analyzed in the previous research [58].

2.3. Implantable Camera

2.3.1. Overview

Coated with a biocompatible epoxy to prevent moisture penetration and sealed using a medical-grade silicone elastomer to attain biocompatibility as well as flexibility, an implantable camera was developed enough to be inserted into the eye. Its operation of wireless image acquisition was evaluated by displaying a processed black and white image. Moreover, to examine reliable wireless communication ranges of the implantable camera in the body, its SNRs were measured while it was covered by an 8-mm-thick biological medium that mimicked an *in vivo* environment.

2.3.2. Design and Fabrication

2.3.2.1. Circuit Design

Circuits for the implantable camera were designed based on two major

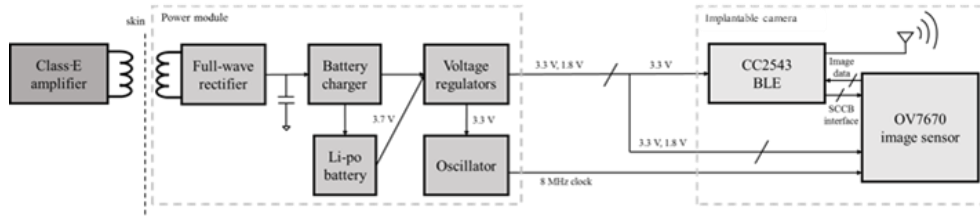


Figure 2.3.1 A circuit block diagram of the implantable camera connected with a power module.

considerations in mind. The first consideration was that current consumption of the implantable camera should be minimized not to damage the eye and the circuits, and the second one was that the implantable camera must be miniaturized enough to be inserted into the eye. Under these thoughts, the circuits were realized as shown in Figure 2.3.1, using a low-power image sensor (OV7670, OmniVision Technologies, Inc., USA) and a BLE system-on-a-chip (CC2543, Texas Instruments, Inc., USA) without extra memories. Wireless image acquisition without extra memories might become a little slow, but this helped the overall circuits to operate in low power and to be miniaturized a lot with no use of peripheral components as well as memories.

The BLE chip consisted of a low-power microcontroller core, a programmable memory, and a 2.4-GHz BLE transceiver. This microcontroller core in the chip controlled not only the interior units, but also the image sensor outside. It drove the image sensor based on the SCCB (serial camera control bus) interface provided by the vendor and received image data from the image sensor. These received image data were then stored into the programmable memory, and the memory delivered them to the BLE transceiver immediately. BLE communication was leveraged because it can operate under lower power and more reliable wireless

connection than other communication protocols, such as ZigBee or Wi-Fi, due to its one-to-one connection [116].

The overall circuits of the implantable camera were powered by a power module including a rechargeable lithium-polymer battery with a voltage of 3.7 V. Because a size of a rechargeable battery was closely related to its capacity, this power module was separated from the implantable camera to achieve sufficiently large battery capacity for stable operation as well as sufficient operating time. The power module with the rechargeable battery was connected to the implantable camera by a cable and supplied operating voltages and a clock signal, as presented in Figure 2.3.1. If the battery was completely discharged in the body, a class-E

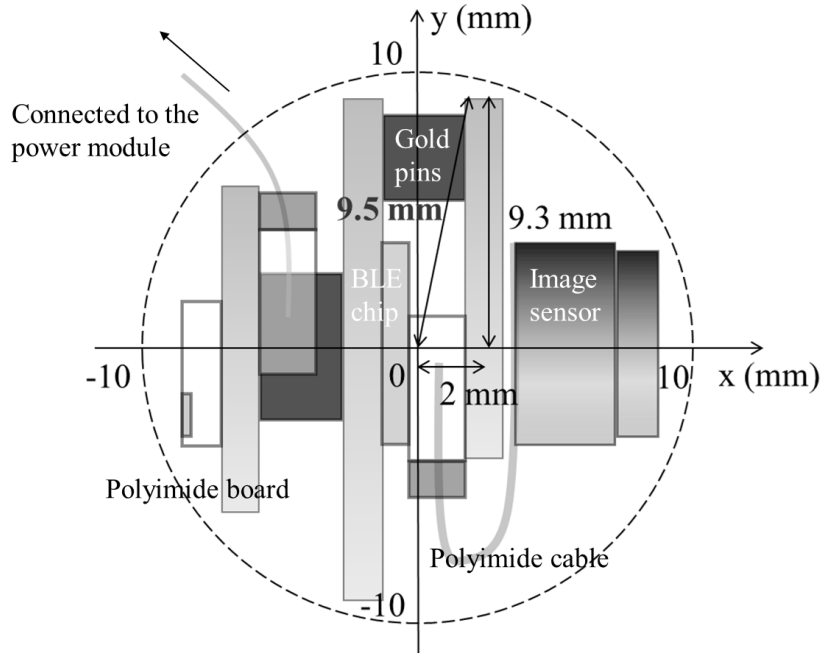


Figure 2.3.2 Schematically drawn PCBs of the implantable camera, which were stacked for three-layered structure to be packaged in a spherical form.

amplifier outside the body can be used to transfer charging power to the battery via an inductive link.

Furthermore, PCBs of the implantable camera were designed to be stacked in three-layered structure as drawn in Figure 2.3.2. This PCB structure of three layers was deeply considered for device miniaturization to easily insert the implantable camera into the eye. Each layer was made of flexible round-shaped polyimide and connected to each other by gold header pins with 1-mm pitches. Every component of the implantable camera including the BLE chip was soldered on the PCBs, and the image sensor was attached on a flexible polyimide cable, sealed with a pinhole lens, and connected to the PCBs by a commercial connector (Molex, LLC., USA). The overall structure of the circuits of the implantable camera in Figure 2.3.2 was built up with the maximum radius of 9.5 mm to be packaged in a spherical form afterward.

2.3.2.2. Wireless Communication Program

When the implantable camera started running, it firstly acted as a beacon, a kind of a transmitter (TX), to confirm the presence of a receiver (RX). The implantable camera was supposed to find a specific RX using a synchronous address preset in the implantable camera. If a certain RX with the same address appeared, this RX took a beacon signal from the implantable camera and sent an acknowledgement (ACK) signal back, which implied that the beacon signal was successfully received. As a result, using this initial signal exchange between the two devices, the BLE communication of one-to-one connection became completed.

Subsequently, the implantable camera acquired an image of one frame, and the operation of transmitting several rows of the image immediately was repeated until the image was entirely sent to the RX through the BLE communication. This prompt transmission of an image was unavoidably used due to the absence of extra memories, but it was quite effective in obtaining real-time images wirelessly.

2.3.2.3. Epoxy Coating and Elastomer Sealing

Epoxy coating and elastomer sealing were leveraged to package the overall circuits of the implantable camera like the shape of an eyeball; these processes were also applied to packaging the power module in a cuboidal form, but the procedures were explained in this section focusing on the implantable camera only.

For sealing, a medical-grade silicone elastomer (MED-6233, NuSil Technology, USA) was used to achieve the optical transparency, the biocompatibility, and the flexibility of the implantable camera not only to obtain clear images, but also not to damage surrounding tissues *in vivo*. However, silicone elastomers solely have higher moisture absorption and permeation than other polymeric sealants [31]. Hence, the overall circuits of the implantable camera were also covered with a biocompatible epoxy (EPOTEK 301-2, Epoxy Technology, Inc., USA), prior to elastomer sealing. This epoxy features a visible light transmittance of 99 % as well as a moisture absorption rate of lower than 0.01 %, which could be helpful to improve long-term reliability of an implantable device in a physiological environment [45, 117].

As mentioned above, the overall circuits of the implantable camera were

coated first with the biocompatible epoxy. In this process, dip coating was utilized since it was advantageous to cover rough surfaces of the circuits with a liquid material. The circuits were tied up by thin thread and immersed into a bottle containing the epoxy. The circuits were then pulled up and heated in a convection oven with a temperature of 45 °C for 30 minutes. This heating procedure was conducted for epoxy curing; this low temperature was used not to spoil the circuits and the battery in the power module by heating. After the first epoxy curing, the dip coating and heating was repeated four times more to make the epoxy coated on the circuits thicker. Moreover, because a thickness of the coated epoxy at this moment may be uneven due to gravity, these entire five-time procedures were also performed with the circuits tied upside down. When all the procedures finished, for the complete curing of the coated epoxy, the circuits were heated with the same temperature for

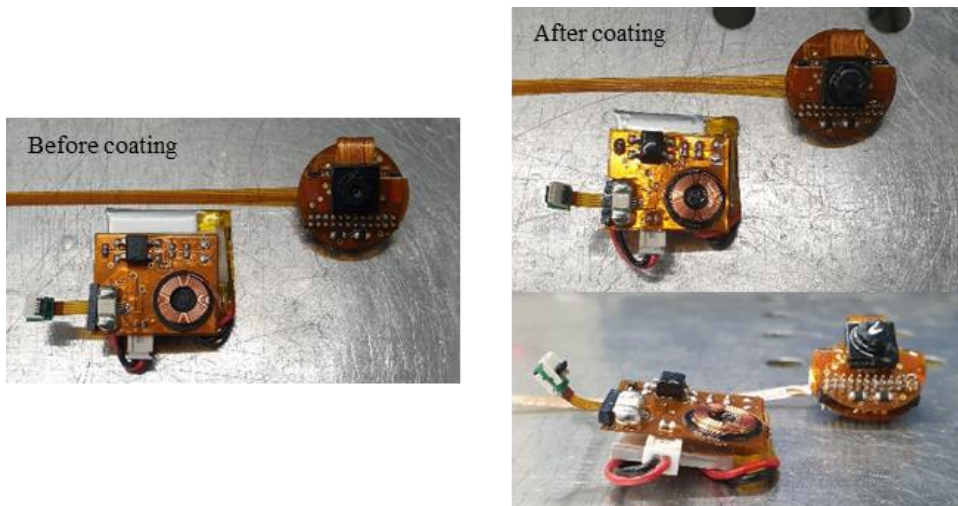


Figure 2.3.3 Photographs of PCBs of the implantable camera before (left) and after (right) underwent epoxy coating, respectively.

more than six hours. The final thickness of the coated epoxy was measured to be about 120 to 130 μm on average.

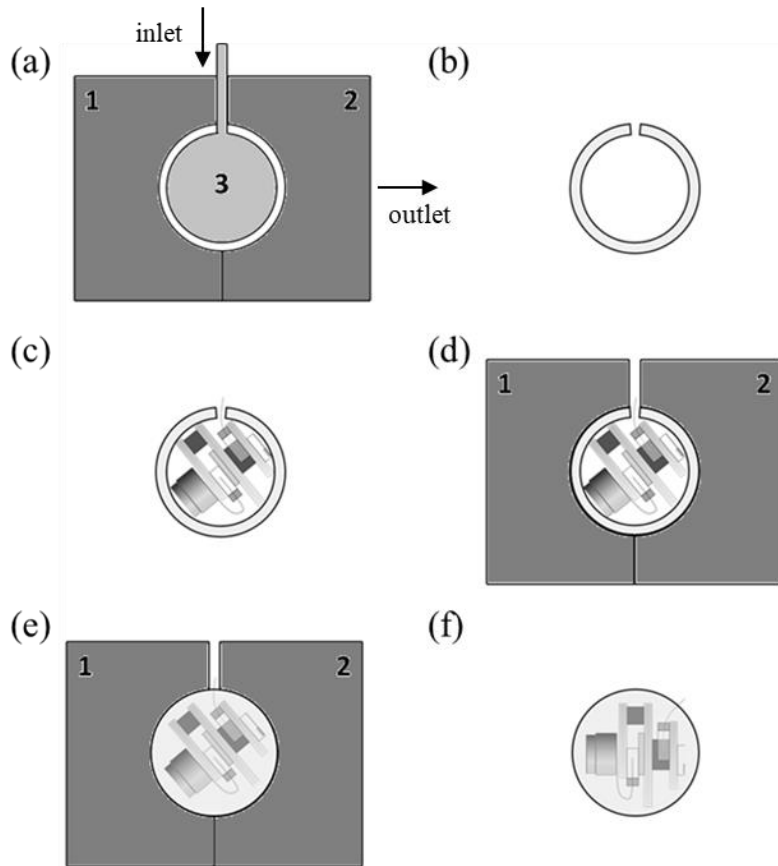


Figure 2.3.4 Procedures of elastomer sealing. (a) Three parts of a molding jig were assembled to make an elastomer shell first. The elastomer was injected into the jig through the inlet at the top. (b) The elastomer shell in a spherical form was molded. (c) The epoxy-coated circuits of the implantable camera were put into the shell. (d) Using the jig without the middle part, the shell containing the circuits was fixed, and (e) the elastomer was injected again to fill the empty space in the shell with the circuits. (f) The elastomer-sealed implantable camera was fabricated like the shape of an eyeball.

After the overall circuits of the implantable camera were coated with the epoxy, they were sealed using the medical-grade silicone elastomer to have a spherical form like an eyeball. Procedures for this elastomer sealing were demonstrated in Figure 2.3.4. As depicted in Figure 2.3.4(a), a molding jig used for the sealing consisted of three parts. The left and the right parts were used to comprise a sphere-shaped mold, and the middle part was used to make an elastomer shell first. When the three parts were assembled, the middle part became floating inside and created an empty space among the parts of the jig. The elastomer was then injected into the jig through the inlet at the top, and the remaining air was deflated via the side outlet. After this injection and elastomer curing with a temperature of 150 °C for 30 minutes, the elastomer shell was molded in a spherical form as described in Figure 2.3.4(b). The elastomer shell was used to make a spherical form in advance and to prevent the circuits from being exposed to the outside. Subsequently, the epoxy-coated circuits of the implantable camera were put into the shell (Figure 2.3.4(c)). The shell containing the circuits was fixed using the jig without the middle part, and the elastomer was injected again to fill the empty space in the shell with the circuits, as drawn in Figure 2.3.4(d) and Figure 2.3.4(e), respectively. Lastly, the final elastomer curing was performed under a temperature of 45 °C for more than six hours not to damage the circuits, and thereby the complete elastomer-sealed implantable camera that resembled an eyeball was fabricated (Figure 2.3.4(f)).

2.3.3. Evaluations

2.3.3.1. Wireless Image Acquisition

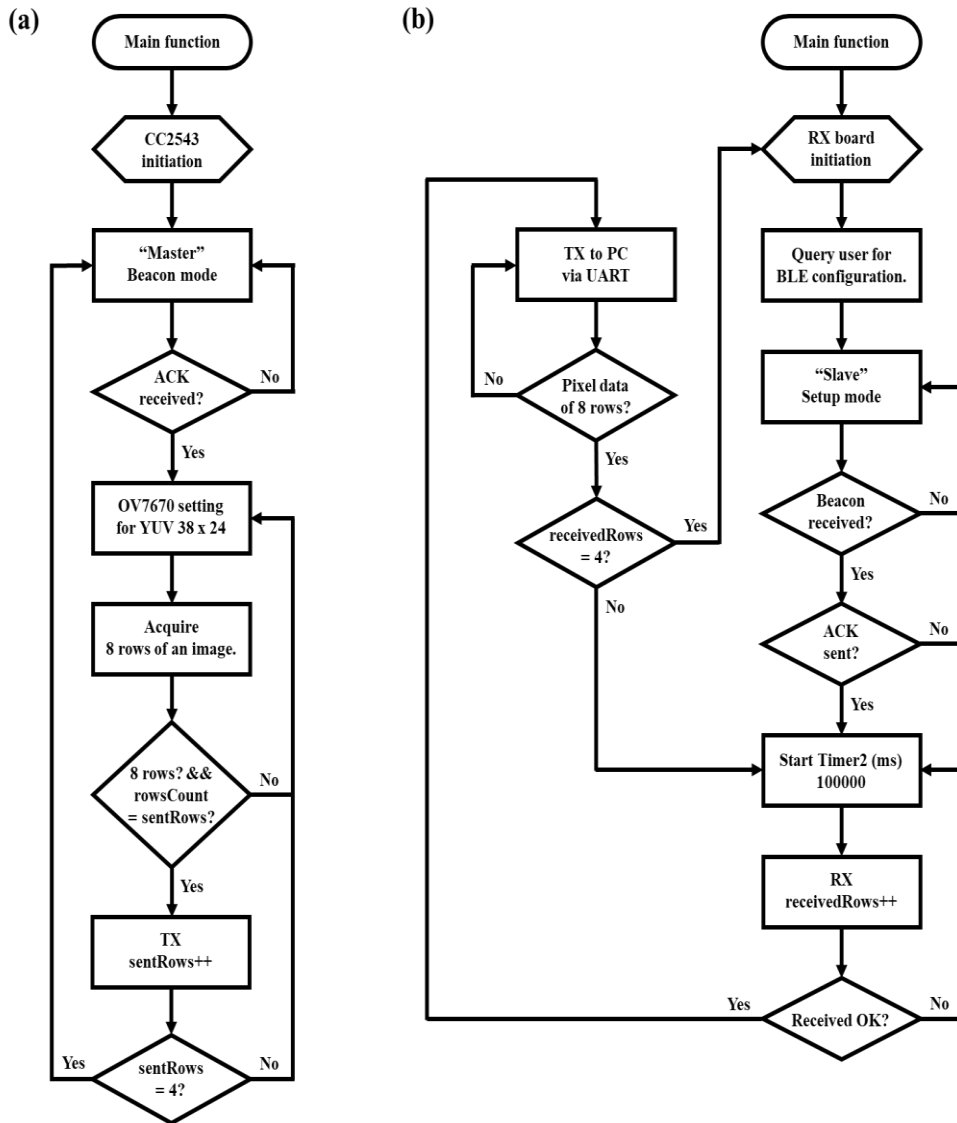


Figure 2.3.5 A BLE communication program algorithm for a wireless image acquisition test using the implantable camera: (a) the TX operation of the implantable camera and (b) the RX operation of an image receiver while connected to a computer.

For wireless image acquisition, the fabricated implantable camera operated with the following four steps sequentially: 1) to catch a control signal from an image

RX (SmartRF05EB, Texas Instrument, Inc., USA), 2) to capture a real-time image, 3) to process the captured image into a black and white image consisting of 38×24 pixels, as described in Figure 2.3.5, and 4) to transmit the processed image as hexadecimal data to the RX. The preset number of pixels was set to be more than 625, the useful number of pixels for pattern recognition tasks [118]. Receiving the hexadecimal image data from the implantable camera, the RX communicated with a computer via a universal asynchronous receiver/transmitter (UART) protocol to deliver the received data. The captured and processed image was then restored from the hexadecimal image data and displayed on a monitor using MATLAB.

2.3.3.2. Signal-to-Noise Ratio (SNR) Measurement

For SNR measurements, the SmartRF Studio 7 of Texas Instrument was used to compute the received signal strength indicator (RSSI) of background noises and random data received by the image RX, respectively. During these measurements, the fabricated implantable camera was reprogrammed by IAR Embedded Workbench to send a number of random data to the RX. The RSSI of the random data was measured repeatedly while communication distances and directions between the implantable camera and the RX were varied. The SNR of the received signals was calculated by subtracting the RSSI of background noises, which was measured when the implantable camera was turned off, from the RSSI of the random data. The measurements were performed in an open area while the implantable camera was covered by an 8-mm-thick biological medium which mimicked an *in vivo* environment; its thickness of 8 mm was chosen to be far thicker than that of the

facial skin. For comparison, the SNR was measured without a biological medium as well. With these measured SNRs, reliable communication ranges of the implantable camera were estimated.

2.4. Multi-Functional Handheld Remote Controller

2.4.1. Overview

The HNS-controller for the proposed totally implantable neural stimulation system herein can control a neural stimulator powered by a rechargeable battery through low-power but relatively long-range ZigBee wireless communication. Additionally, two more functions can be performed by the HNS-controller for expanded applications in percutaneous stimulation as well as inductive charging of the rechargeable battery. Simple switches on the HNS-controller enable users to modulate parameters of stimuli like a gamepad. These handheld and user-friendly interfaces can make it easy to use the HNS-controller under various circumstances. Having these beneficial features, the HNS-controller was fabricated, and its functionality was evaluated *in vivo*, through percutaneous stimulation and remote control especially for avian navigation, as well as *in vitro*.

2.4.2. Design and Fabrication

2.4.2.1. Hardware Description

As mentioned above, although the crucial function of the HNS-controller was ZigBee remote control of a totally implantable neural stimulator, two more functions were added to be used in following experiments; one was precise target

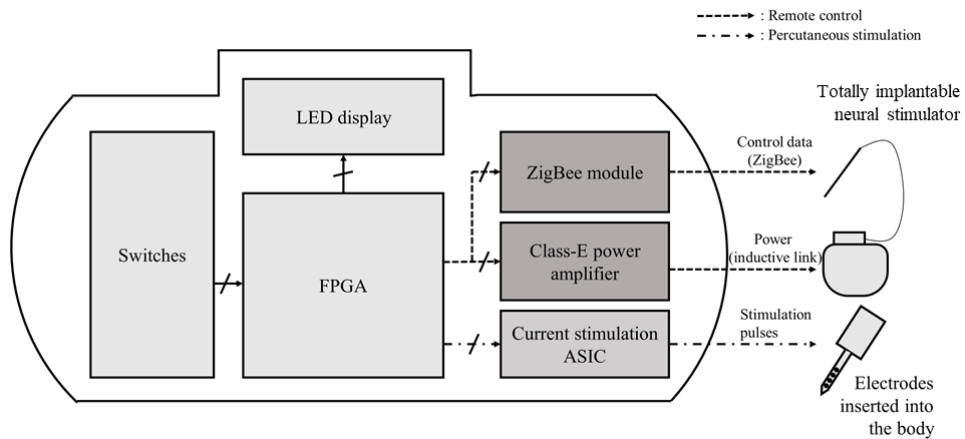


Figure 2.4.1 A block diagram of the HNS-controller that can be used for both percutaneous stimulation and remote control of neural stimulation.

positioning through a percutaneous link prior to implantation of a neural stimulator, and the other was inductive charging of a rechargeable battery in a neural stimulator implanted *in vivo*. These two functions are to be explained briefly in this section and the discussion section.

As described in Figure 2.4.1, the HNS-controller consisted of a current stimulation ASIC, a class-E power amplifier (PA), a ZigBee module, and a field-programmable gate array (FPGA). The HNS-controller can communicate with electrodes and a totally implantable neural stimulator for percutaneous stimulation and remote control, respectively.

In one embodiment, the current stimulation ASIC on the HNS-controller can be connected to electrodes inserted into the brain and supply biphasic current pulses to neurons percutaneously. While the current stimulation ASIC generated biphasic current pulses, the class-E PA and the ZigBee module on the HNS-controller

were completely turned off. To fabricate the HNS-controller, a customized current stimulation ASIC was used [119]. This customized ASIC was designed to generate biphasic current pulses on 16 output channels, in pulse rates, durations, and amplitudes of 20.00–226.0 Hz, 0.020–1.280 ms, and 0.010–10.23 mA, respectively. Though we used the customized ASIC in this study, one may replace it with commercial active elements [120–122].

In other embodiment, the class-E PA and the ZigBee module can transmit power and data, respectively, to a totally implantable neural stimulator wirelessly. While the class-E PA and the ZigBee module delivered power and data, the current stimulation ASIC was on standby, consuming less than 1 mW. The class-E PA can transfer enough power via an inductive link to charge a rechargeable battery in a totally implantable stimulator. This PA was constructed using a widely-used topology that has very high power transfer efficiency (100 % theoretically) while taking up small area [123, 124]. In addition to the PA, the ZigBee module (CC2530, Texas Instruments, Inc., USA) can send control data including parameters of biphasic current pulses to a totally implantable stimulator. Using data wirelessly sent from this ZigBee module on the HNS-controller, a stimulation circuit in a totally implantable stimulator can generate pulses corresponding to the data.

The FPGA on the HNS-controller had to communicate with all of these components comprising the HNS-controller. To realize this operation, an FPGA module (DLP-HS-FPGA-A, DLP Design, USA) was used. This FPGA module has 50 programmable pins, sufficiently large memories, and easy-to-program interfaces. A diagram and a flow chart of an FPGA program for the HNS-controller are depicted

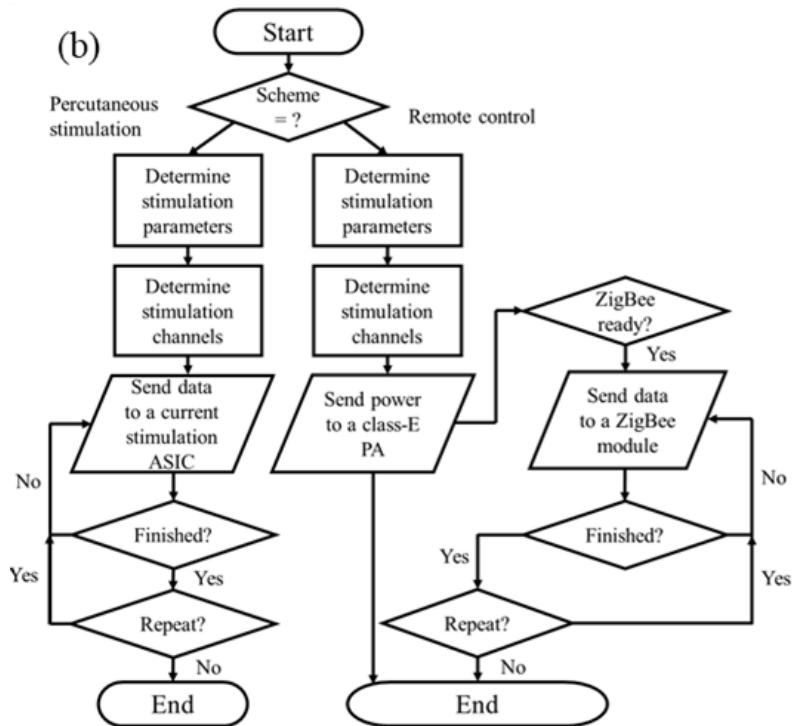
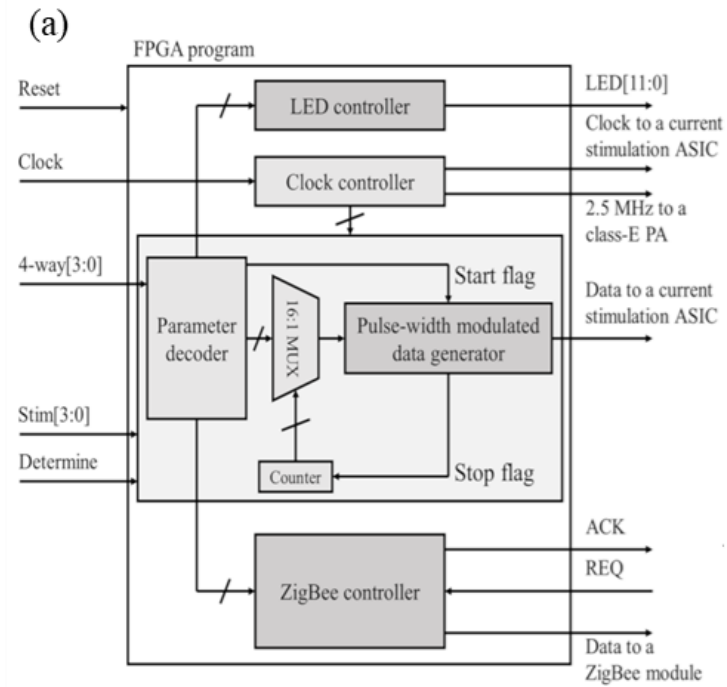


Figure 2.4.2 (a) An FPGA program block diagram for the HNS-controller and (b) a flow chart of the FPGA program.

in Figure 2.4.2(a) and Figure 2.4.2(b), respectively. Details of this FPGA program are demonstrated below.

2.4.2.2. Software Description

Users should choose one of two operation schemes of the HNS-controller, either percutaneous stimulation or remote control of neural stimulation as shown in Figure 2.4.2(b), though the FPGA worked in the same way as follows as depicted in Figure 2.4.2(a). 4-way[3:0] were responsible for a 4-way switch. After users selected which parameter of biphasic current pulses to be varied by horizontal movements of the 4-way switch, they can change values of each parameter by its vertical movements. In the meantime, the corresponding values were presented on a light-emitting diode (LED) display through LED[11:0], and users can store these values in memories by triggering a button switch, named Determine. Subsequently when one of four button switches, named Stim[3:0], was triggered, control data including all the values were delivered to the current stimulation ASIC or the ZigBee module in accordance with an operation scheme chosen at the beginning. Especially for remote neural stimulation control, ACK and REQ (request) were declared and used to synchronize data communication between the FPGA and the ZigBee module.

2.4.3. Evaluations

2.4.3.1. *In Vitro* Evaluation

Figure 2.4.3 describes a schematic of a totally implantable neural stimulator designed for remote neural stimulation control using the HNS-controller.

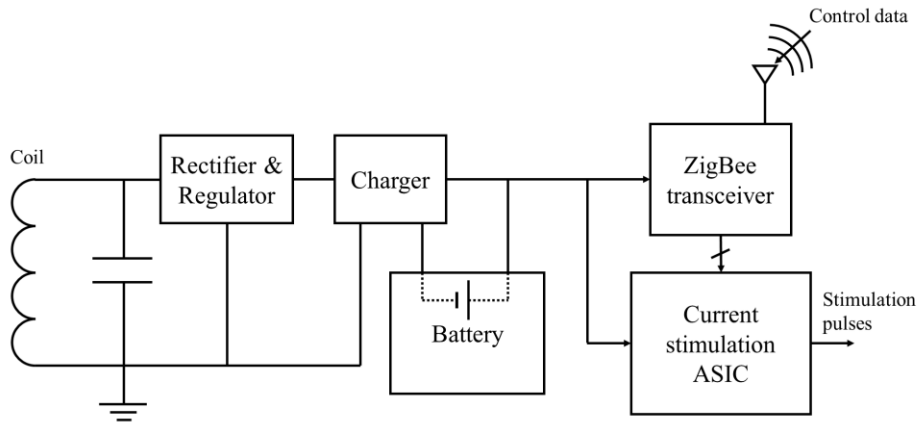


Figure 2.4.3 A schematic of a totally implantable neural stimulator designed for remote neural stimulation control using the HNS-controller.

The customized current stimulation ASIC abovementioned was also used as a stimulation circuit in this totally implantable stimulator. Using control data received by a ZigBee transceiver of the stimulator, this current stimulation ASIC can generate biphasic current pulses and vary their parameters.

A rechargeable battery powered the current stimulation ASIC and the ZigBee transceiver. However, due to limited capacity of a battery, it may be impossible to operate the stimulator permanently *in vivo*. To overcome this limitation, a coil and a charger were contained in the stimulator to build an inductive charging link. Further details of the totally implantable stimulator were provided in the following reference of Yun, S., collaborated in this work [69].

In vitro evaluation on remote control of the totally implantable stimulator using the HNS-controller was conducted to verify the functionality of the HNS-controller prior to *in vivo* evaluation. An electrode, whose impedance magnitude was

measured to be 10 k Ω , was dipped in PBS solution (Gibco #10010, Invitrogen Life Technologies, USA) and connected to the stimulator. This PBS solution was used to set up an *in vivo*-like environment. The HNS-controller sent control data of biphasic current pulses with a duration of 0.100 ms and an amplitude of 0.200 mA to the stimulator. Biphasic current pulses generated from the stimulator were measured by the oscilloscope.

2.4.3.2. *In Vivo* Evaluation

In vivo experiments, especially for avian navigation, were carried out for both percutaneous stimulation and remote control of neural stimulation using the HNS-controller; these evaluations were collaborated with three laboratories in Seoul National University (Prof. Seo, K., Seo, J. M., and Song, Y. K.). To observe a turning

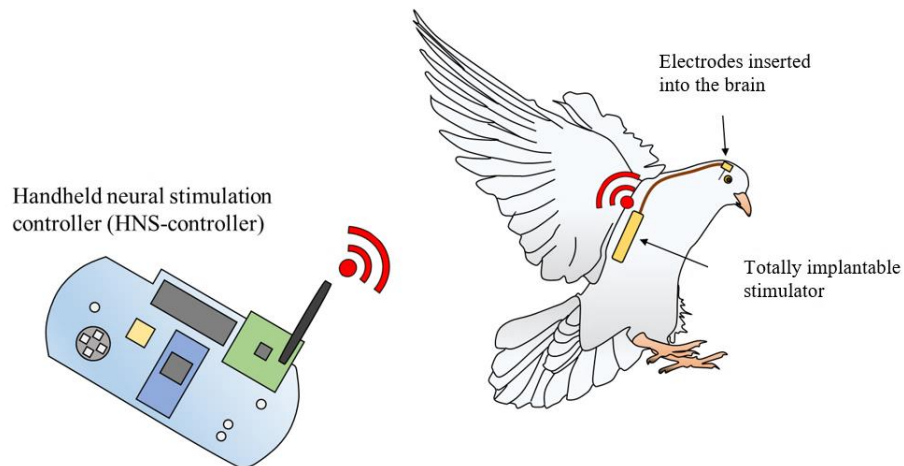


Figure 2.4.4 An illustration of the proposed totally implantable neural stimulation system applied to remote avian navigation.

behavior of a pigeon, its nucleus (formatio reticularis medialis mesencephalic, FRM) was targeted for stimulation [125]. The FRM was selected based on the recent study on electrical stimulation of motor-related brain nuclei of pigeons [126].

An adult pigeon (*Columbia livia*) was anesthetized with inhalational isoflurane. After positioning the pigeon's head in a stereotaxic apparatus so that the eye-beak plane pointed 45 degrees below the horizontal plane, a reference point (bregma) was determined and holes were drilled in the skull above the target region. This motor-related region was targeted using the stereotaxic apparatus with precision based on the following reference [126]. The dura and the arachnoid were penetrated with a 27G needle. An electrode was then advanced to the target region along the penetration path. After implantation of the electrode, for percutaneous stimulation, the gap between the electrode and the cranium was closed using dental cement. On the other hand, for remote navigation, the electrode was connected through a biocompatible polyimide cable to a totally implanted stimulator in the pigeon's back, which was packaged using LCP. Connections were sealed using dental cement, and all surgical wounds were closed with nylon sutures. In both *in vivo* experiments, biphasic pulses with a duration of 0.080 ms and an amplitude of 0.400 mA were applied to the target region repeatedly for 0.5 seconds using the HNS-controller. All experiment procedures performed in this study involving animals were in accordance with the ethical standards of the Institutional Animal Care and Use Committee of Seoul National University (SNU-170622-1).

Chapter 3

Results

3.1. COP-Based Fabrication and Encapsulation

3.1.1. Fabricated Depth-Type Microprobe

As shown in Figure 3.1.1, the COP-based depth-type microprobe with four isolated channels was fabricated by the developed simple process. The shank of the microprobe had a length of 10 mm and a width of 650 μm . Its morphology, highlighted in Figure 3.1.1 by the red square, was minutely examined under a microscope (Eclipse LV150, Nikon, Japan). The shank consisted of four gold transmission lines having a width of 100 μm , and its tip was sharpened by the CO_2 laser for easier insertion to the brain. Each gold electrode site had a geometrical surface area of $100 \times 100 \mu\text{m}$, while each spacing between two adjacent channels was 300 μm as designed to record clearly distinguishable neural signals *in vivo*. Additionally, the connection pads of the microprobe were separated by a pitch of 0.5 mm to be joined to the commercial Molex connector.

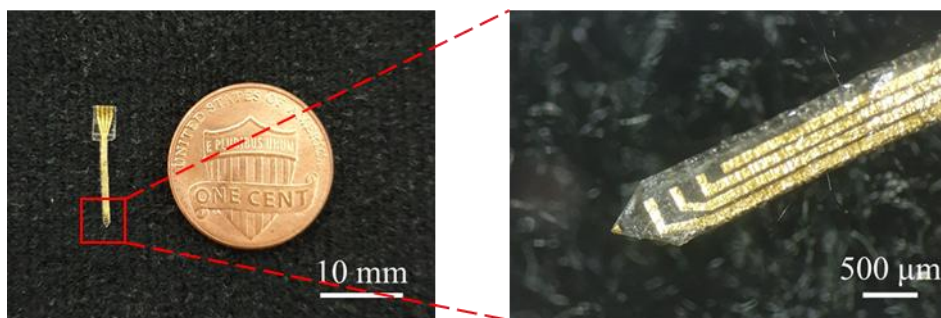
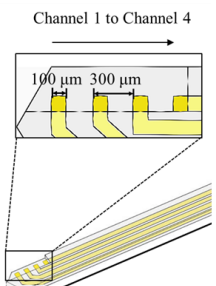


Figure 3.1.1 Photographs of the COP-based depth-type microprobe: an image of its overall structure (left) and a microscopic image of the gold patterns (right) comprising the shank of the microprobe highlighted by the red square.

Table 3.1.1 Electrochemical impedances at 1 kHz of the four channels consisting of the COP-based depth-type microprobe.



Channel number	Impedance (kΩ)
Channel 1	15.36 ∠ -71.23°
Channel 2	13.94 ∠ -73.93°
Channel 3	13.94 ∠ -73.59°
Channel 4	15.87 ∠ -69.81°

3.1.1.1. Electrochemical Impedance

An electrochemical impedance of each channel was measured in the PBS solution at 1 kHz, the standard frequency commonly used in this assessment, as



Figure 3.1.2 A microscopic image of a gold channel of the COP-based depth-type microprobe. The geometrical surface area of the channel was 100×100 μm, though its effective surface area would be larger because of the rough surface of the gold thin film.

demonstrated in Table 3.1.1. The averaged impedance magnitude of the four channels was calculated to be $14.8 \pm 0.857 \text{ k}\Omega$. As depicted in Figure 3.1.2, the rough surface of the gold thin film increased an effective surface area of each channel. Accordingly, the COP-based depth-type microprobe had a lower ratio of the averaged impedance magnitude to the geometrical surface area of each channel than that of other microprobes in the following references [83, 84].

3.1.1.2. Mechanical Characteristics

Figure 3.1.3(a) shows measurement results of the buckling tests carried out with varying thicknesses of the COP-based depth-type microprobes. As the force sensor moved downward, the force applied on the COP-based depth-type microprobe smoothly increased. In accordance with the thickness varied from 50 to 200 μm , both the buckling load and the yield stress of the microprobe also increased proportionally depending on the thickness, as charted in Table 3.1.2.

The forces exerted on the tungsten rod and the LCP-based microprobes were measured as well (Figure 3.1.3(b)), to estimate the corresponding elastic modulus as well as yield stresses and to compare their mechanical characteristics with those of the COP-based microprobes. Both the elastic modulus and the yield stresses of all the examined specimens are demonstrated in Table 3.1.2. With the identical dimensions, the COP-based microprobe was stiffer than the LCP-based one, while both of them were more flexible than the tungsten rod.

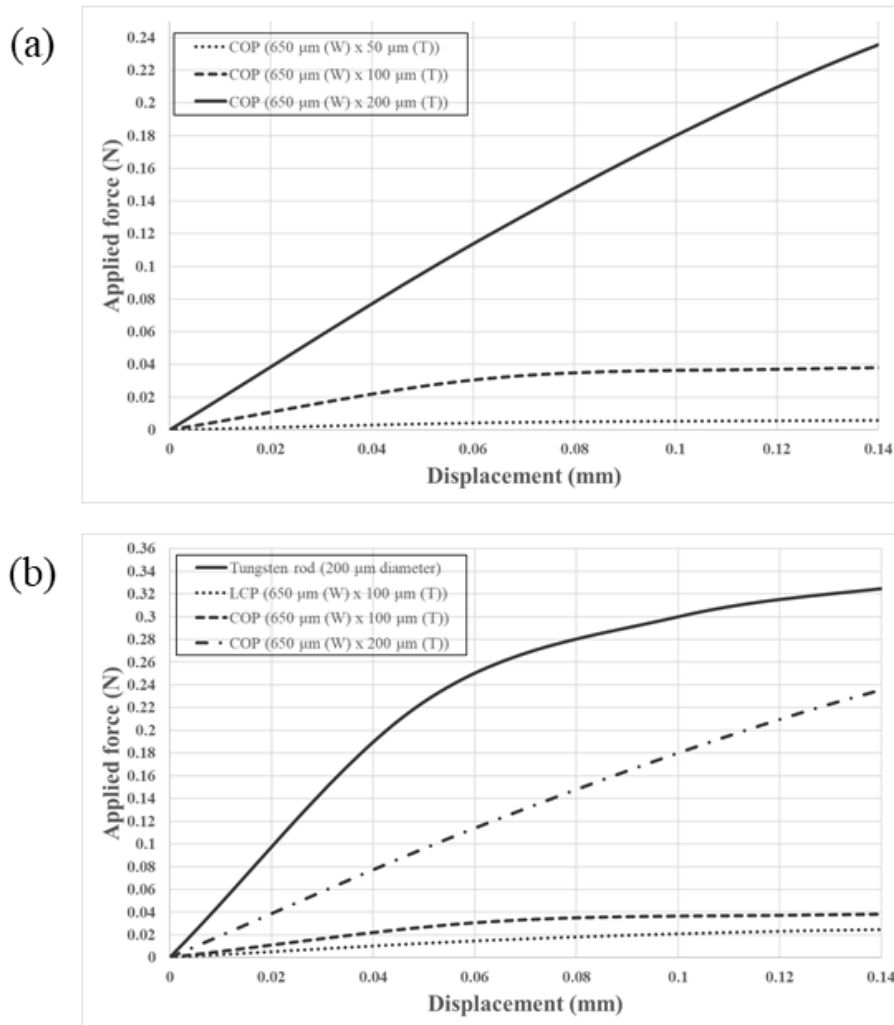


Figure 3.1.3 Results of the buckling tests. (a) A graph of thickness-dependent averaged applied forces vs. displacement. The thicknesses of the COP-based depth-type microprobes were set to be 50 (the number of specimens, $n=6$), 100 ($n=6$), and 200 μm ($n=4$), while they had the same width of 650 μm . (b) A graph of material-related averaged applied forces vs. displacement. The tungsten rod with a diameter of 200 μm and the LCP-based microprobes ($n=3$) with a cross-section area of 650 (width, W) \times 100 (thickness, T) μm were also used in the buckling tests for comparison.

Table 3.1.2 Results of the buckling tests: elastic modulus and yield stress.

Material (W ^a ×T ^b)	COP (650 μm × 50 μm)	COP (650 μm × 100 μm)	COP (650 μm × 200 μm)	LCP (650 μm × 100 μm)	Tungsten rod (200 μm diameter)
Elastic modulus (GPa)	1.098 (n=6)	1.738 (n=6)	2.001 (n=4)	1.372 (n=3)	372.7
Yield stress (mN)	8 ±1.5	41 ±1.6	220 ±8.3	34 ±1.9	290

^a width, ^b thickness

3.1.1.3. *In Vivo* Neural Signal Recording

Neural signals evoked in the left SI region of the rat were recorded using the 100-μm-thick COP-based depth-type microprobe. These neural signals were analyzed by an analysis program (Offline Sorter, Plexon, Inc., USA). Figure 3.1.4 describes different color-coded units of the neural signals, which were sorted according to their waveform shapes after recorded on the four channels, from Channel 1 to Channel 4 (as noted in Figure 2.1.2). The neural signals were garnered with two units on Channel 1, three units on Channel 2, four units on Channel 3, and two units on Channel 4. Furthermore, Figure 3.1.5 shows raster plots that present the corresponding units of the neural signals over time.

As shown in both Figure 3.1.4 and Figure 3.1.5, larger and more frequent neural signals were measured on Channel 4, especially from 30 to 60 seconds during right whisker stimulation, than those of the other channels. These results demonstrated that the brain region associated with whisker stimulation was closest to Channel 4, and the neural signals were synchronized to the stimulation cycle as

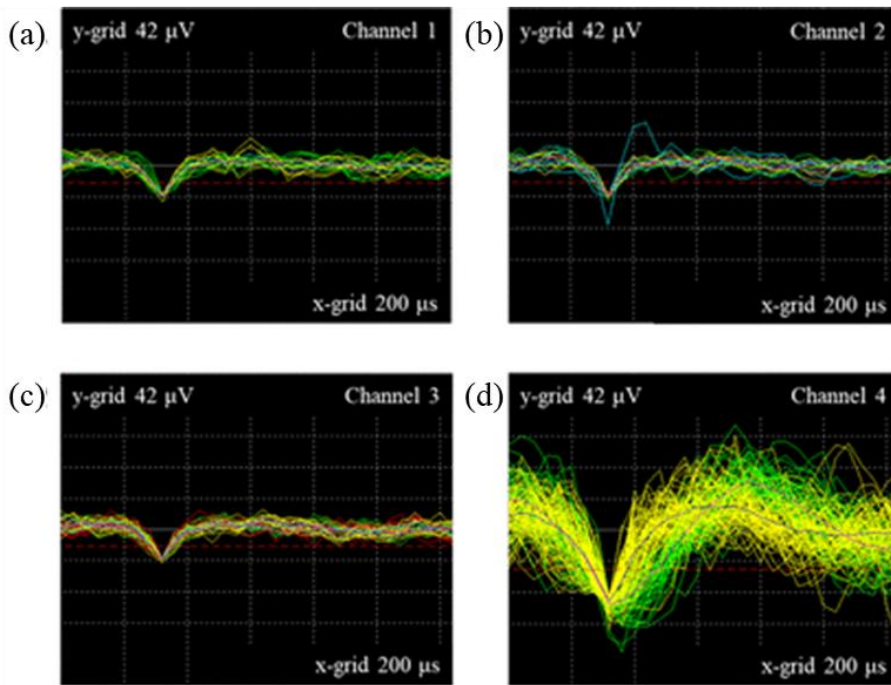


Figure 3.1.4 Results of the *in vivo* simultaneous multi-channel neural signal recording. Different color-coded units of the neural signals were sorted according to their shapes of waveforms, after recorded on the four channels of the 100- μ m-thick COP-based depth-type microprobe.

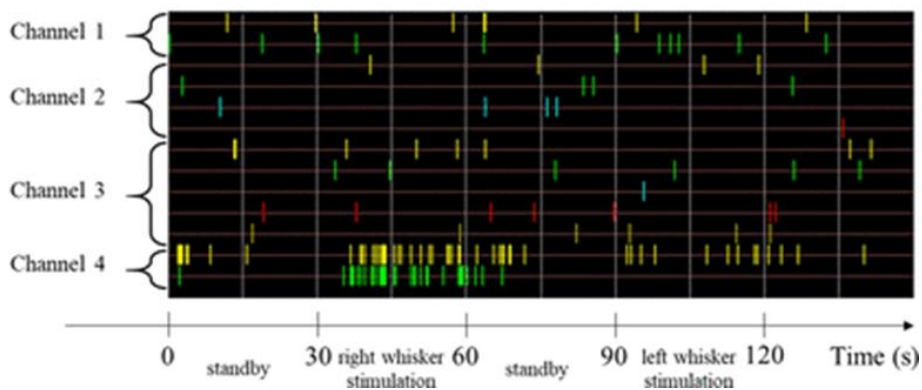


Figure 3.1.5 Raster plots that display the corresponding units of the neural signals over time.

well. As a result of this recording in the left SI region of the rat, the neural signals of right whisker stimulation were successfully garnered by the 100- μm -thick COP-based depth-type microprobe, while their differences among channels were obvious because of the distant spacing of 300 μm between two adjacent channels.

3.1.2. COP Encapsulation

3.1.2.1. *In Vitro* Reliability Test

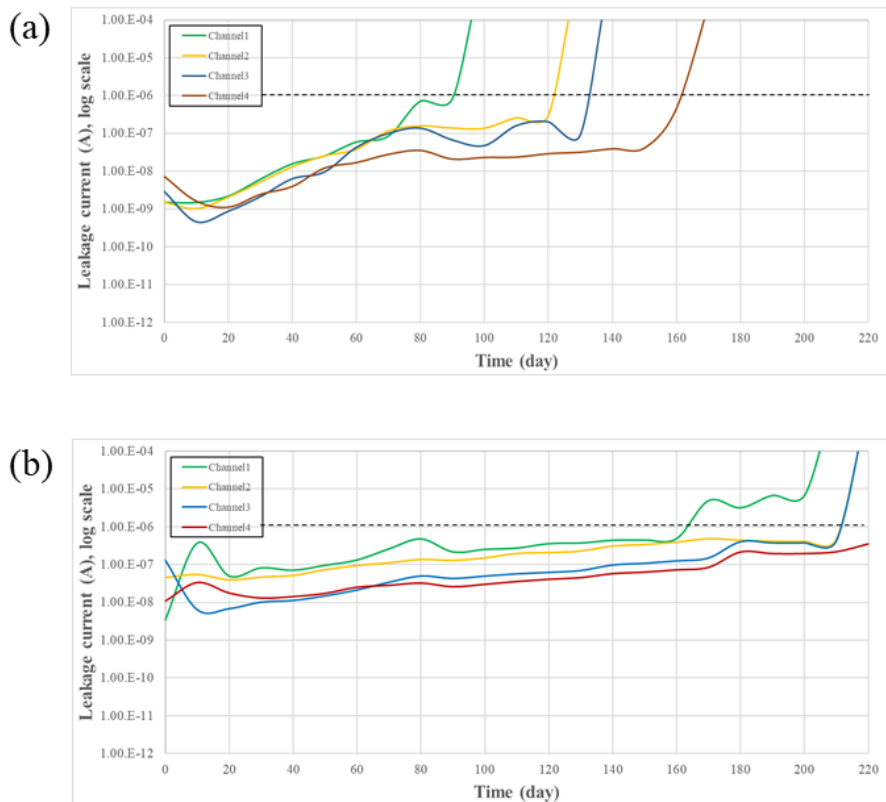


Figure 3.1.6 Leakage current measurement results during the accelerated aging tests of the COP encapsulation formed under (a) a lower pressure of 0.051 MPa (Group 1) and (b) a higher pressure of 0.509 MPa (Group 2). The threshold level of 1 μA (the black dashed line) was set arbitrarily.

Figure 3.1.6(a) and Figure 3.1.6(b) present averaged leakage current data measured from the four IDEs in the COP encapsulation formed under a lower pressure of 0.051 MPa and a higher pressure of 0.509 MPa, respectively. The initial leakage current levels for all of the IDEs in the two groups were on the nano-ampere scale at a DC bias of 2 V. After soaked, the leakage current levels were stabilized for the first 10 to 15 days, after which they slowly increased to 0.1–1 μA over a period of more than 100 days for the former group and 200 days for the latter group. Subsequently, there were the drastic increases of the leakage currents for every IDE; a drastic increase in a leakage current would indicate that an IDE failed during accelerated aging and soaking, due to the complete penetration of moisture and ions.

After the COP encapsulation failed the accelerated aging tests, the tested

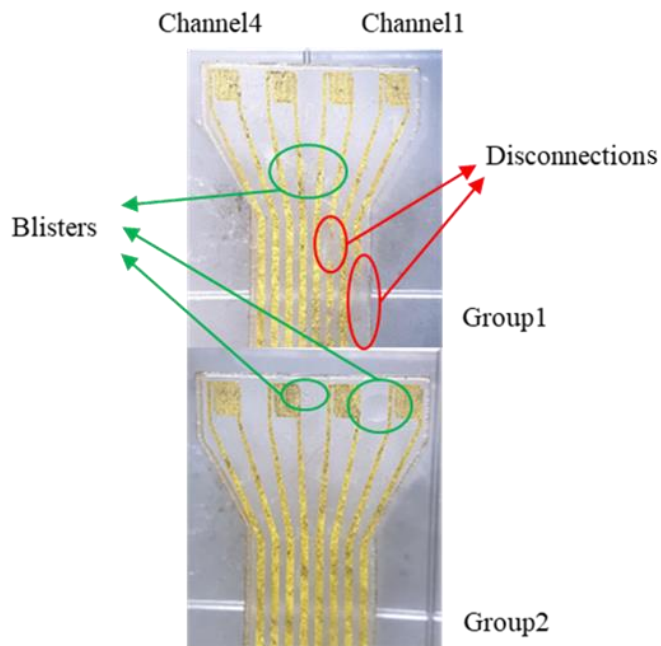


Figure 3.1.7 The two groups of the COP encapsulation harvested after the complete moisture and ion penetration.

two groups were harvested and observed under a microscope. As shown in Figure 3.1.7, the failed groups had several degradations in their structure. In Group 1 of the COP encapsulation formed with the lower pressure, severe disconnections were detected apart from small blisters. On the contrary, in Group 2 of the COP encapsulation fabricated with the higher pressure, there was several small blisters but no disconnection. These results explained that higher pressure in the fabrication of the COP encapsulation can provide more reliable insulation performance to some extent for future implantable devices.

3.2. Penta-Polar Stimulation

3.2.1. Fabricated IC and Surface-Type Electrodes

The custom-designed penta-polar stimulation ASIC was fabricated with a size of 4.5×2.4 mm, as depicted in Figure 3.2.1. Most area of the ASIC, presented

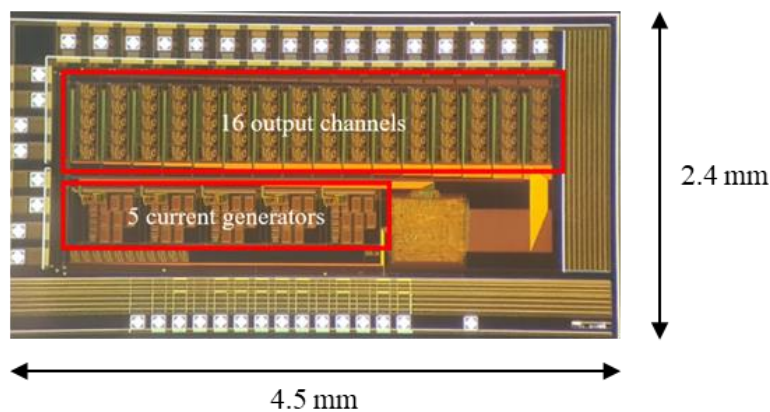


Figure 3.2.1 The custom-designed penta-polar stimulation ASIC fabricated with a size of 4.5×2.4 mm.

by the red rectangles, was filled with the five current generators and the 16 output channels.

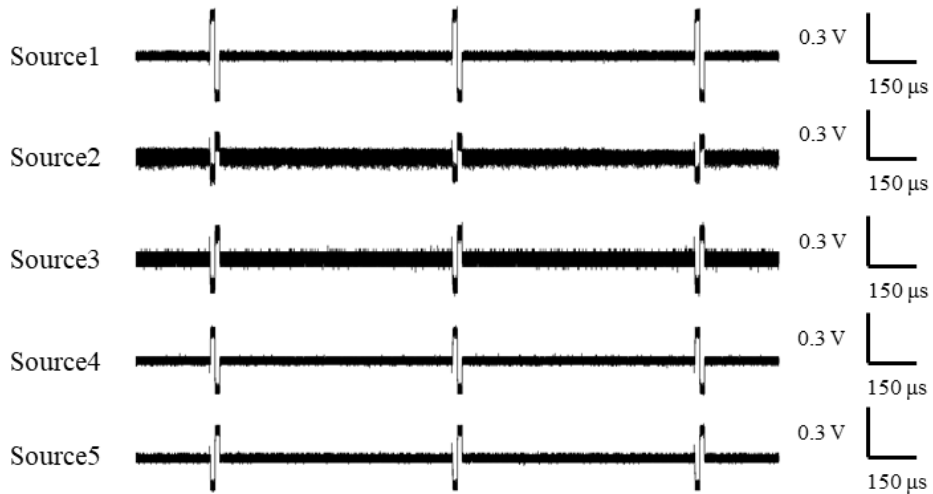


Figure 3.2.2 Five biphasic current pulses supplied from the fabricated penta-polar stimulation ASIC at the same time.

Table 3.2.1 Parameters of the five biphasic current pulses (Figure 3.2.2) for verifying the operation of the fabricated penta-polar stimulation ASIC.

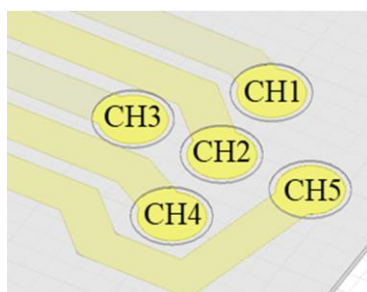
Duration (ms)		0.05
Pulse interval (ms, period)		0.80
Amplitude (mA) and phase	Source 1	0.03 and anodic-first
	Source 2	0.01 and cathodic-first
	Source 3	0.02 and cathodic-first
	Source 4	0.02 and anodic-first
	Source 5	0.02 and cathodic-first

The operation of simultaneous stimulation using the fabricated penta-polar stimulation ASIC was verified as shown in Figure 3.2.2. For this measurement, a load resistance of 10 k Ω was connected to each output channel. Parameters of five biphasic current pulses supplied from the fabricated ASIC were arbitrarily determined for the verification as listed in Table 3.2.1.

As described in Figure 2.2.2, the COP-based surface-type electrodes were fabricated by the developed simple process. The COP-based surface-type electrodes contained five separate channels, each of which had an individual diameter of 450 μm and a center-to-center spacing of 800 μm .

The COP-based surface-type electrodes were briefly characterized by measuring electrochemical impedances of the five channels and charge storage capacity (CSC) of one channel. An electrochemical impedance of each channel was measured in the PBS solution at 1 kHz as demonstrated in Table 3.2.2. Moreover, the CSC was estimated from a result of cyclic voltammetry as shown in Figure 3.2.3. The cyclic voltammetry was performed with a scanning rate of 50 mV/s from

Table 3.2.2 Electrochemical impedances at 1 kHz of the five channels consisting of the COP-based surface-type electrodes.



Channel number	Impedance (k Ω)
CH 1	3.006 \angle -23.29°
CH 2	2.049 \angle -30.38°
CH 3	2.161 \angle -37.23°
CH 4	2.071 \angle -38.42°
CH 5	1.857 \angle -36.55°

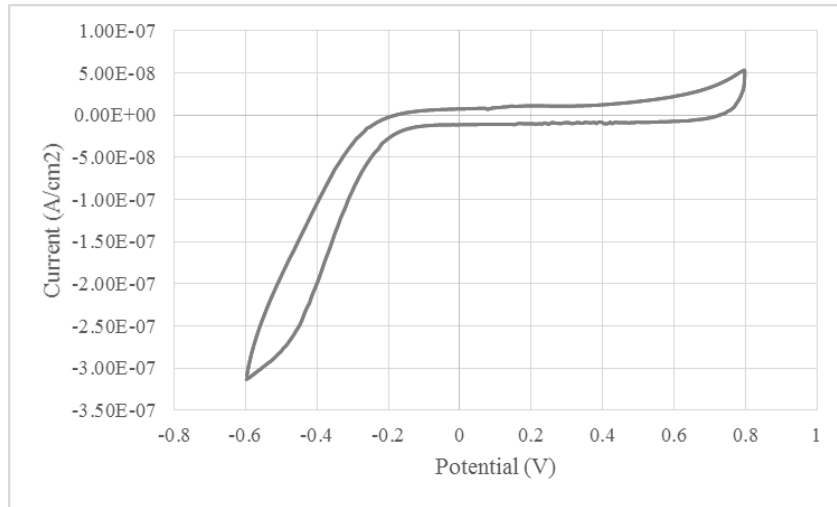


Figure 3.2.3 A result graph of cyclic voltammetry conducted using the COP-based surface-type electrodes with a scanning rate of 50 mV/s from -0.6 to 0.8 V.

-0.6 to 0.8 V. As a result of the estimation, the CSC was calculated to be about 0.187 mC/cm², which needs to be enhanced by surface modification, for example, by iridium oxide deposition for actual effective neural stimulation over threshold levels of neurons [30, 127].

3.2.2. Evaluations

3.2.2.1. Focused Electric Field Measurement

Electric fields produced by the mono-polar and the penta-polar stimulation (Figure 2.2.4) are described in Figure 3.2.4. Each result of the FEA and the *in vitro* evaluation was normalized using the maximum electric field magnitude measured from the FEA and the *in vitro* evaluation, respectively. Overall electric field magnitudes of the penta-polar stimulation were slightly lower than those of the

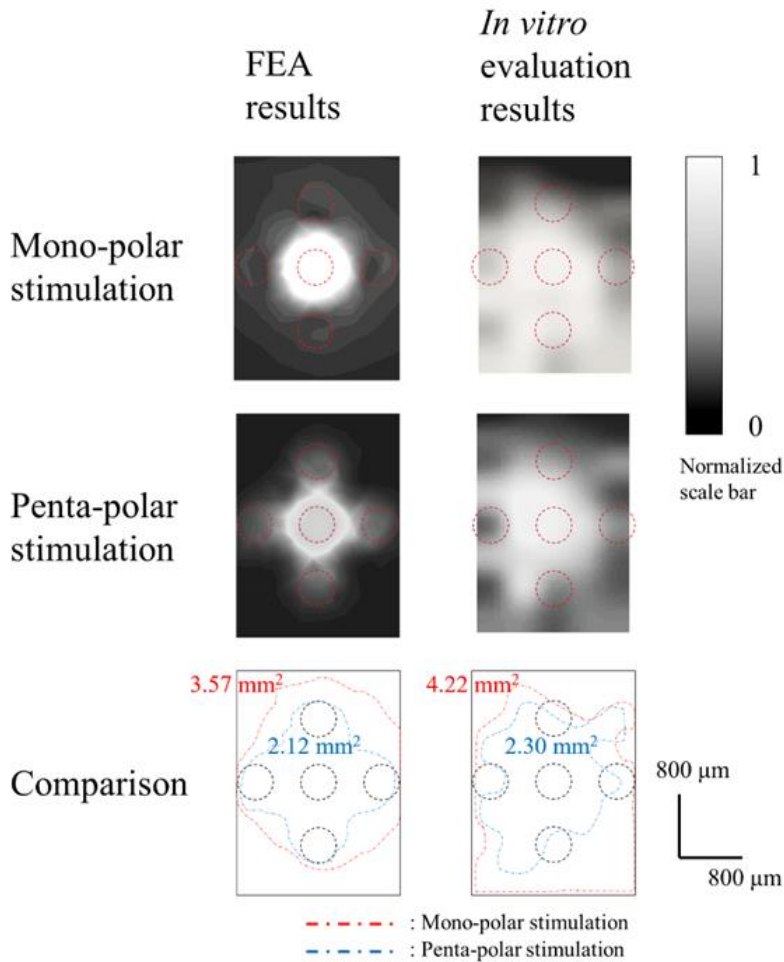


Figure 3.2.4 Electric fields simulated and measured from the FEA and the *in vitro* evaluation, respectively, with comparison results between the mono-polar and the penta-polar stimulation.

mono-polar stimulation, but field distribution areas were much smaller in the penta-polar stimulation than in the mono-polar stimulation. To analyze these field distribution areas quantitatively, effective electric fields were assumed to have the magnitudes of more than 20 % of the maximum value. As a result, compared with the mono-polar stimulation, the penta-polar stimulation showed 0.594 and 0.545

Table 3.2.3 A comparison table on a field distribution area ratio of the penta-polar and the mono-polar stimulation between the FEA and the *in vitro* evaluation.

A ratio between field distribution areas of the penta-polar and the mono-polar stimulation	
FEA	0.594
<i>In vitro</i> evaluation	0.545

times smaller areas of field distribution, respectively, at the distance from the stimulation electrodes of 100 μm , as charted in Table 3.2.3.

3.2.2.2. Steered Electric Field Measurement

Furthermore, the weighted centroids of electric field magnitudes generated by the penta-polar stimulation according to the distance from the stimulation electrodes were plotted in Figure 3.2.5, while varying the amplitude ratio coefficient (Figure 2.2.5). These results on virtual channel generation were estimated qualitatively. At the distance of less than 100 μm , the weighted centroids were created near the edge of each electrode. The weighted centroids were generated most effectively at the distance of 150 μm . The greatest number of the weighted centroids between the two adjacent stimulation electrodes was observed at the distance of 100 μm , but more linear arrangements of them were produced at the distance of 150 μm . By contrast, at the farther distance than 150 μm , the number of the weighted centroids between the two stimulation electrodes decreased, and the arrangements became nonlinear again. In addition, the weighted centroids tended to be created

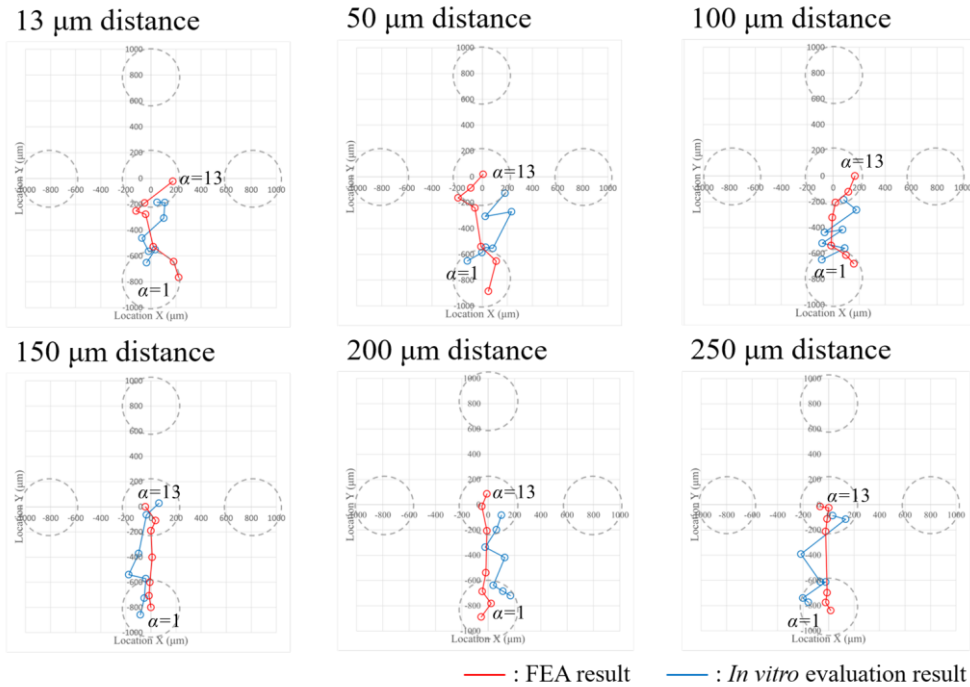


Figure 3.2.5 The weighted centroids of electric field magnitudes, virtual channels, plotted from both the FEA and the *in vitro* evaluation results in accordance with the distance, while varying the amplitude ratio between the stimuli of the two adjacent stimulation electrodes (x-axis: Location X, μm and y-axis: Location Y, μm).

around the middle of each electrode as the distance increased.

3.3. Implantable Camera

3.3.1. Fabricated Implantable Camera

Figure 3.3.1 depicts the implantable camera fabricated in a spherical form and the connected power module by a polyimide cable. Coated with the epoxy and sealed using the elastomer, the implantable camera featured a diameter of 19.7 mm and a weight of 5.75 g; due to the packaging, the diameter of the implantable

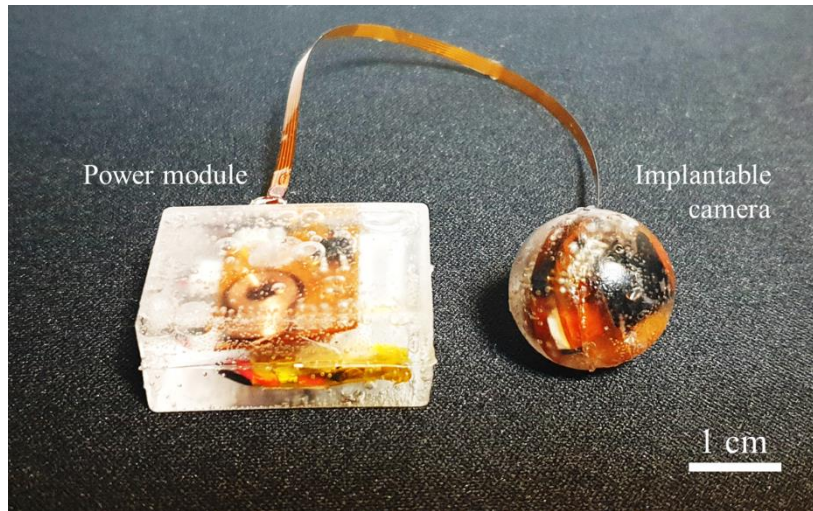


Figure 3.3.1 A photograph of the fabricated implantable camera in a spherical form and the power module, which were coated by the biocompatible epoxy and sealed using the medical-grade silicone elastomer.

camera increased by around 0.7 mm. In addition, the current consumption of the implantable camera was estimated to be 13.0 mA on average, when an image was acquired and wirelessly transmitted via the BLE communication. The power module was also packaged by the same processes, and it had a size of 35.0×24.0×14.0 mm and a weight of 16.6 g. The size of the power module was closely dependent on a size of the rechargeable battery in it, whose nominal capacity was 100 mAh.

3.3.2. Evaluations

3.3.2.1. Wireless Image Acquisition

Figure 3.3.2 shows a wireless image acquisition test setup with the fabricated implantable camera connected with the power module and the BLE image receiver linked with a computer through a UART cable. The text of ‘ABC’ was

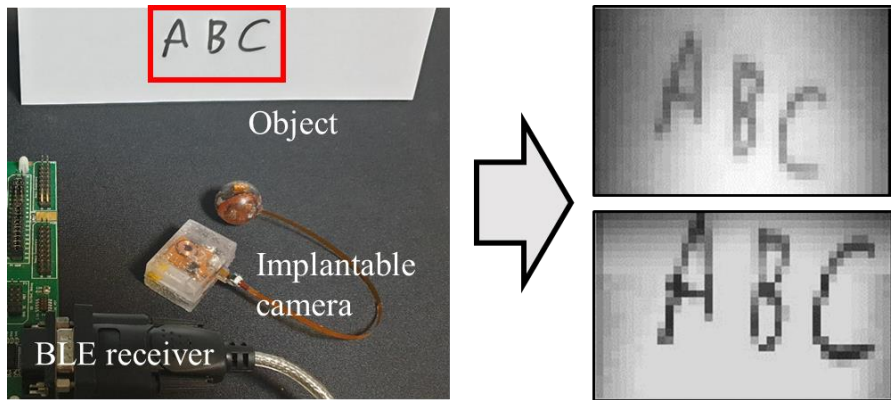
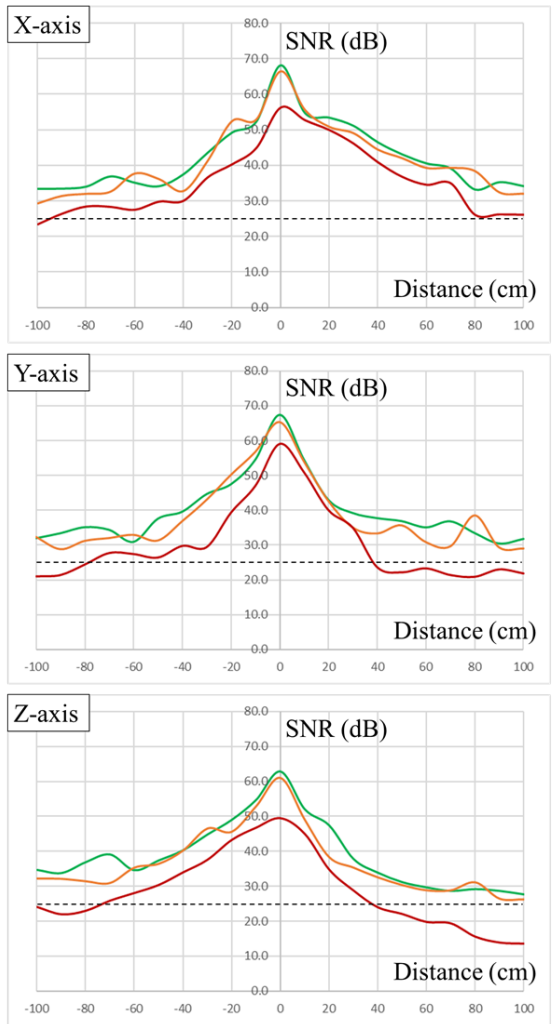
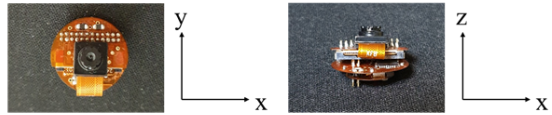


Figure 3.3.2 A test setup for wireless image acquisition and two restored photographs of black and white images of ‘ABC’ with 38×24 pixels.

written on white paper, as an object to be captured by the implantable camera. After the BLE communication of one-to-one connection between the implantable camera and the image receiver was completed by the signal exchange, the implantable camera started to obtain an image of ‘ABC’. Though an initial image acquired by the implantable camera was a color image of 640×480 pixels, this image was processed to be a black and white image of 38×24 pixels since this processing operation was programmed in the implantable camera. The captured and processed image of ‘ABC’ was successfully transmitted to the image receiver through the BLE communication and then restored using MATLAB as presented in Figure 3.3.2.

3.3.2.2. SNR Measurement

As shown in Figure 3.3.3, the SNR of received signals at the BLE image receiver was measured while the communication distances and directions between the fabricated implantable camera and the image receiver were varied. The



Unpackaged w/o a biological medium
 Packaged w/o a biological medium
 Packaged w/ an 8-mm-thick biological medium

Figure 3.3.3 The SNR of received signals at the BLE image receiver while varying the communication distances and directions. The green, orange, and red lines indicated the measurements using the unpackaged implantable camera, the packaged one, and the packaged one covered by a biological medium, respectively. The black dashed line was an acceptable SNR of 25 dB for reliable wireless communication.

measurements were performed using the unpackaged implantable camera, the packaged one, and the packaged one covered by an 8-mm-thick biological medium, respectively. Assuming an acceptable SNR was 25 dB in power, the communication range of the implantable camera was estimated for reliable wireless communication [128]. Although the maximum SNR with the packaged implantable camera was slightly decreased compared to that with the unpackaged one, both cases without any biological media showed a communication range of 100 cm or more. In contrast, when the packaged implantable camera was covered by the biological medium, there were the minimum and the maximum distance with the acceptable SNR, which were 36.4 cm in the Z-axis direction and 94.8 cm in the X-axis direction, respectively. Nevertheless, this suggested that the communication range of the implantable camera was still guaranteed for reliable wireless communication up to 36.4 cm, which was longer than a distance between the eye and the visual cortex in general.

3.4. Multi-Functional Handheld Remote Controller

3.4.1. Fabricated Remote Controller

The current stimulation ASIC, the class-E PA, the ZigBee module, and the FPGA were mounted on a PCB that resembles a gamepad as shown in Figure 3.4.1. Users' finger movements were considered in an arrangement of switches to provide user-friendly interfaces like a gamepad. The HNS-controller also became handheld due to parallel-connected batteries shown in Figure 3.4.1(b). A dimension of the HNS-controller was 17.5×10.0×5.30 cm, and it weighed 141.8 g except for batteries.

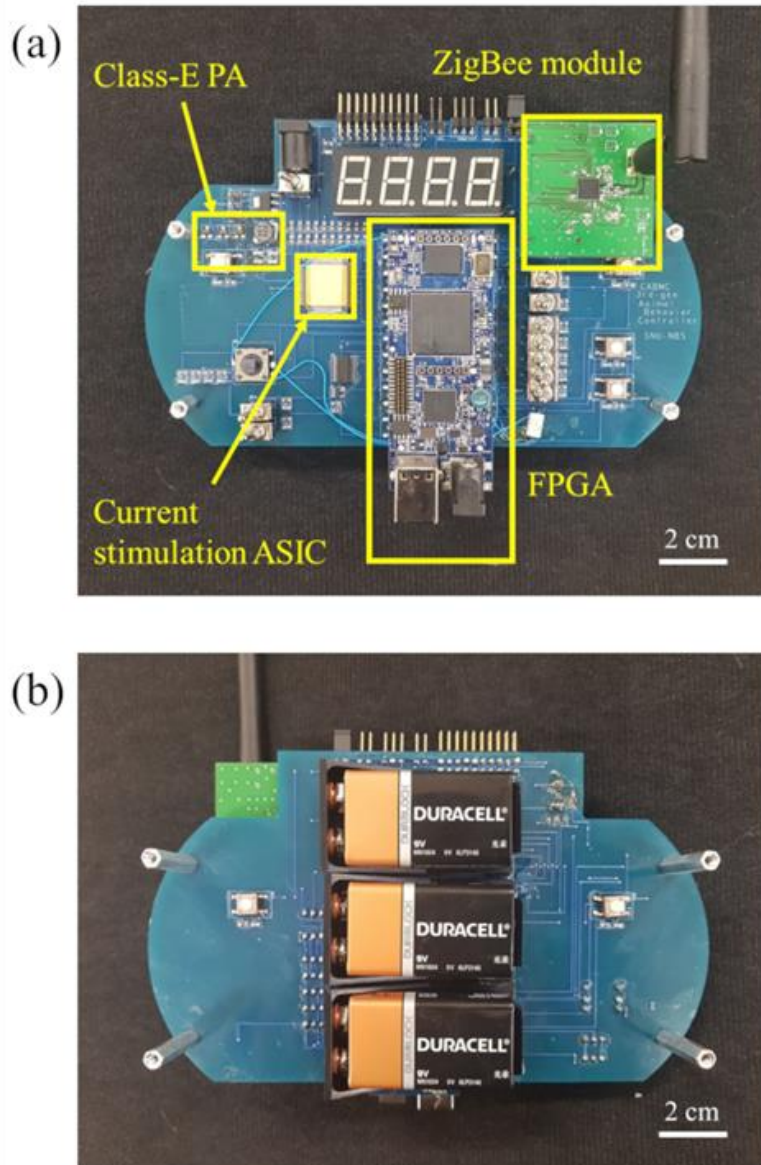


Figure 3.4.1 Photographs of (a) the top-view and (b) the bottom-view of the fabricated HNS-controller. Its dimension and weight were measured to be $17.5 \times 10.0 \times 5.30$ cm and 141.8 g except for batteries, respectively.

3.4.2. Evaluations

3.4.2.1. *In Vitro* Evaluation

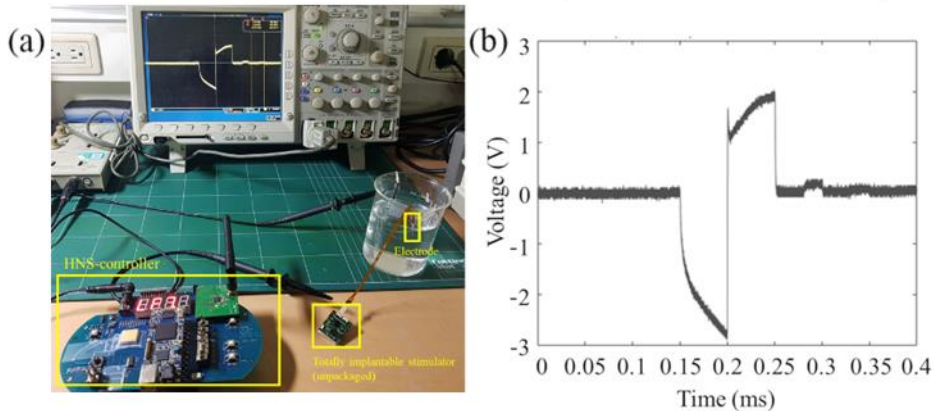


Figure 3.4.2 (a) A photograph of the *in vitro* evaluation for remote control of the totally implantable stimulator (unpacked) using the HNS-controller and (b) one of biphasic current pulses generated from the totally implantable stimulator in the PBS solution.

As shown in Figure 3.4.2(a), the HNS-controller wirelessly transmitted control data via ZigBee communication to an unpackaged totally implantable stimulator. This stimulator received these data and successfully supplied biphasic current pulses to the electrode with an impedance magnitude of 10 k Ω , dipped in the PBS solution. These biphasic current pulses were measured by the oscilloscope, and one of them was plotted as depicted in Figure 3.4.2(b). The measured pulse featured a duration of 0.100 ms, which conformed to the parameters preset by the HNS-controller for this evaluation. When the impedance of the electrode was considered, a peak voltage generated by the biphasic pulses with an amplitude of 0.200 mA should be ± 2 V. Though the measured peak voltage was close to ± 2 V, the pulse in Figure 3.4.2(b) was slightly distorted because it was supplied in the PBS solution,

an electrolyte.

3.4.2.2. *In Vivo* Evaluation

An electrode connected to the HNS-controller was inserted into the FRM region of a pigeon, and the biphasic current pulses were delivered through the

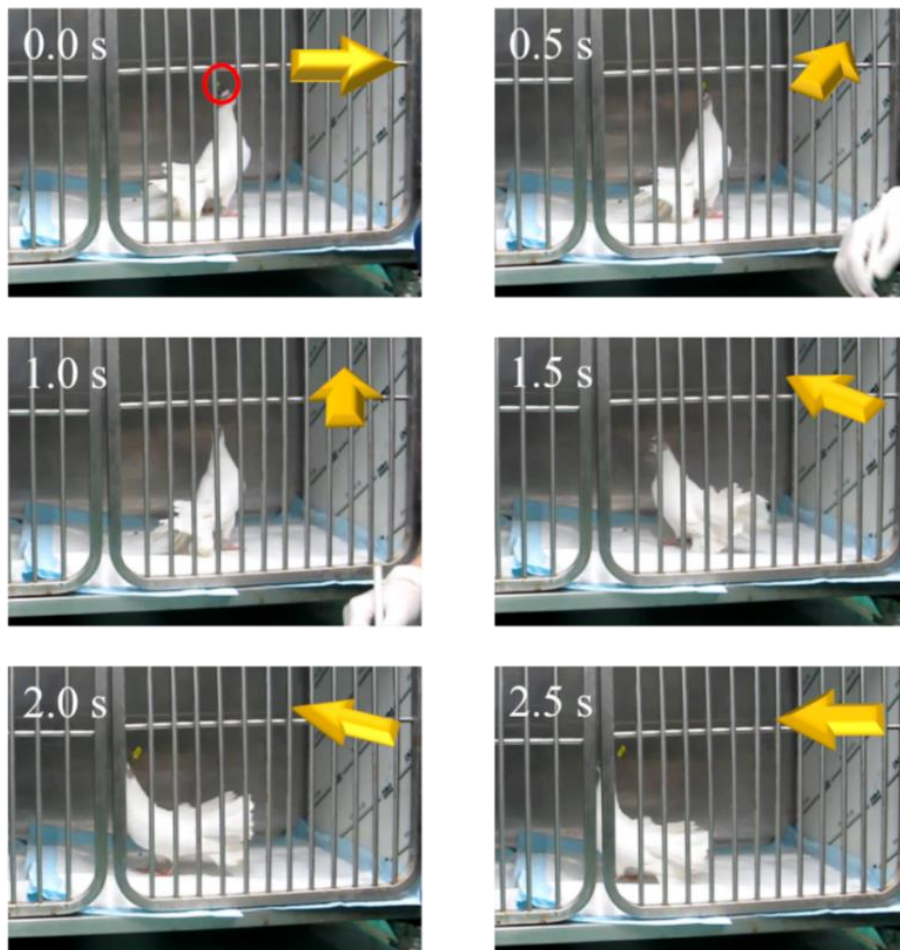


Figure 3.4.3 Photographs of a pigeon's turning-left behavior induced by percutaneous stimulation on the FRM region. These photographs show successive time flow for 2.5 seconds. The red circle indicates a percutaneous link that connected the HNS-controller to an electrode inserted into the target region.

electrode. Responding to one percutaneous stimulation, the pigeon showed a 180-degree turning-left behavior lasting 2.5 seconds as shown in Figure 3.4.3.

The same electrode was inserted into the target region of a pigeon and connected to an LCP-packaged stimulator totally implanted in the pigeon's back.

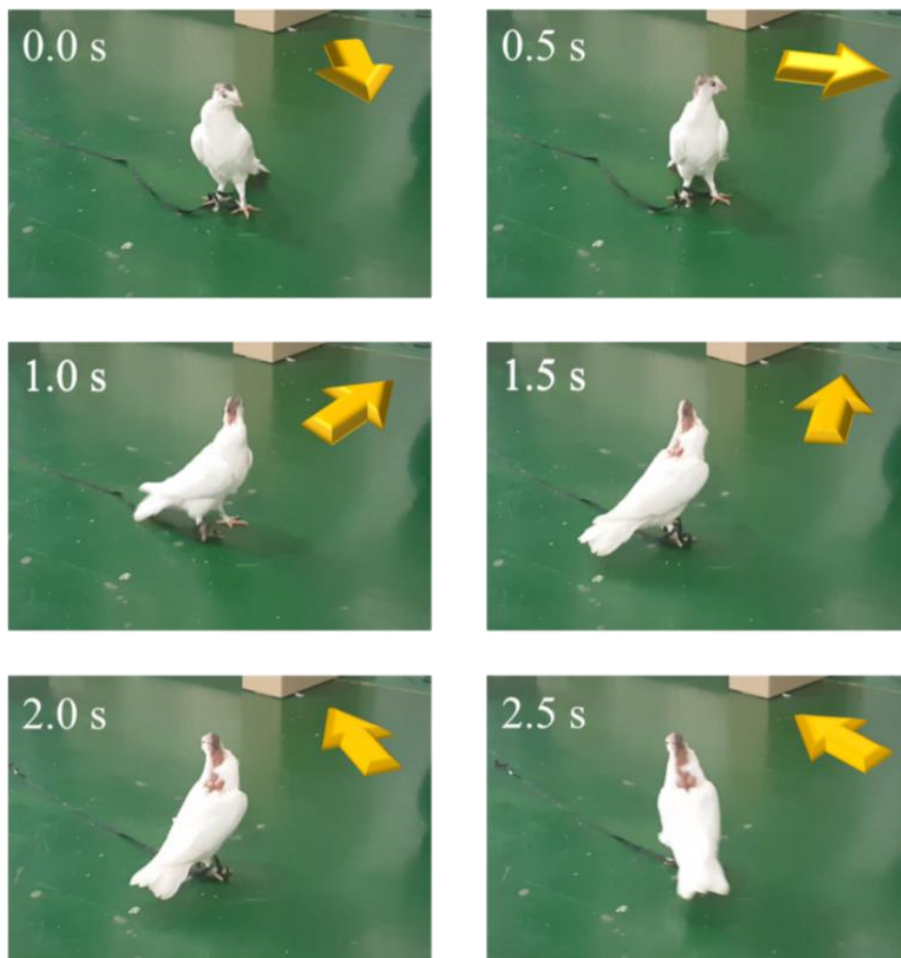


Figure 3.4.4 Photographs of a turning-left behavior of a pigeon induced by remote neural stimulation control using the HNS-controller. These photographs also show successive time flow for 2.5 seconds. The black wire on the bottom was tied to the pigeon's leg, restraining the pigeon not to run away in open areas.

After this stimulator received control data wirelessly sent from the HNS-controller, the biphasic current pulses were generated from the stimulator and delivered to the electrode. As shown in Figure 3.4.4, responding to the stimulation with the same parameters as in the case of percutaneous stimulation, the pigeon showed the identical 180-degree turning-left behavior lasting 2.5 seconds.

Chapter 4

Discussions

4.1. COP-Based Fabrication and Encapsulation

4.1.1. Fabrication Process and Fabricated Devices

The COP-based simple fabrication process was developed using thermal lamination and laser machining without the semiconductor technology. The COP-based process was successfully applied to the fabrication of the depth-type microprobes and the surface-type electrodes as well as the encapsulation.

During the process, a gold thin film was thermally laminated on a COP substrate with no adhesion layer since gold was known for good adhesion to COP [94]. Such adhesion between gold and COP was briefly tested by Scotch tape testing. After the thermal lamination, the Scotch tape testing was conducted five times on a gold-laminated COP substrate. As a result of this qualitative testing, there was no

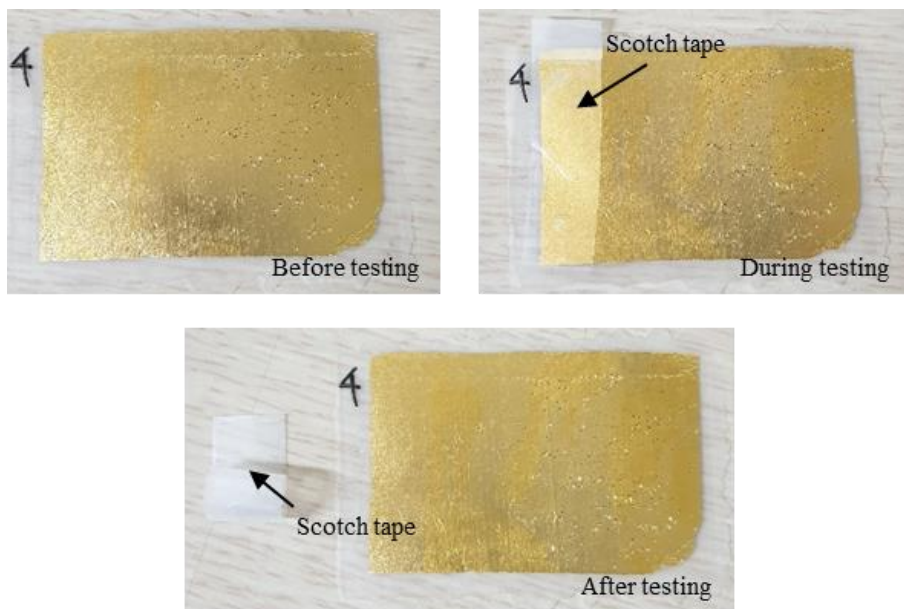


Figure 4.1.1 Photographs of Scotch tape testing on a gold-laminated COP substrate to briefly evaluate the adhesion between gold and COP.

detectable detachment between gold and COP as shown in Figure 4.1.1.

Although gold and COP featured good adhesion as verified above, it was crucial to optimize process conditions, including temperature, pressure, and time, during thermal lamination because their linear thermal expansion had somewhat of a big difference. A linear thermal expansion coefficient of COP is $70.0 \times 10^{-6} \text{ K}^{-1}$, whereas that of gold is $14.2 \times 10^{-6} \text{ K}^{-1}$ [89, 90]. Due to this difference, process conditions with higher temperature, higher pressure, or longer time can lead to severe migration of gold patterns on a COP substrate. Therefore, all of the process conditions in this study were empirically optimized values not to damage a gold thin film as well as a COP substrate. Fortunately, good adhesion between gold and COP helped to reduce the process time to be less than 3 minutes. Additionally, during the COP-based fabrication process, it was also found that COP can be well diffused under lower pressure as well as shorter time than those set in similar LCP-based fabrication process using thermal lamination, which made a COP substrate and a COP cover attached easily [45, 47]. These advantages of the COP-based fabrication process might be useful for future implantable devices that need a monolithic body and conformable shape modification by thermoforming [47].

In addition to the thermal lamination, laser machining was leveraged to simply pattern a gold thin film attached on a COP substrate. For example with the COP-based depth-type microprobe, the geometrical surface area of each channel, which was $100 \times 100 \text{ }\mu\text{m}$, was a little larger than that of other microprobes [30]. This is because the minimum feature size for gold patterning was $100 \text{ }\mu\text{m}$, which was limited by the beam size of the UV laser used in the developed COP-based

fabrication process. To reduce the width and the geometrical surface area of gold patterns, it is preferable to use laser equipment that has a smaller beam size; such laser equipment would make future COP-based microprobes narrower and have more multiple channels. Additionally, computer-aided layout files were used for this gold patterning and outline shaping in the developed COP-based fabrication process. Unlike masks for photolithography, traditionally used in metal patterning, these layout files can be easily revised at any time as needed. Thus, the number of channels and the shape of the COP-based microprobe are not limited to four channels and a depth-type microprobe, respectively. Herein, by the help of the computer-aided layout files, the IDEs in the COP encapsulation as well as the surface-type electrodes were also easily patterned on a gold-laminated COP substrate without masks.

The controllable stiffness of the COP-based microprobe in relation to its thickness was evaluated. The COP-based microprobe was flexible as a polymer-based microprobe. Nonetheless, when its thickness was more than 100 μm , the COP-based microprobe had sufficient stiffness so that it can be inserted in the rat brain. Hence, the COP-based microprobe had long shank length, reproducibility, mass fabrication, and mechanical stability with flexibility in common with an LCP-based microprobe [84, 112]. Furthermore, the COP-based microprobe featured larger elastic modulus and yield stress than those of the LCP-based microprobe. Therefore, the COP-based microprobe could be inserted in the rat brain even with smaller thickness.

4.1.2. Encapsulation and Optical Transparency

The leakage current data provided crucial information about the long-term reliability of the COP encapsulation in a physiological environment. The IDEs in Group 2 with the higher lamination pressure were intact for a longer time than those in Group 1. If the time of the second drastic increase was taken for approximate lifetime estimation, it was 122 days for Group1 and 211 days for Group2. This means that the lifetime of the COP encapsulation can be achieved up to approximately eight years, estimated by the ten-degree rule (4.1) at the body temperature as follows:

$$f = 2^{\frac{T-T_{\text{ref}}}{10}}, \quad (4.1)$$

where f is the factor of an increased rate of aging, T is the elevated temperature of 75 °C, and T_{ref} is the reference temperature of 37 °C. This lifetime was shorter than that of LCP but longer than those of both polyimide and parylene-C [45].

Though a generally recommended temperature for accelerated aging tests of polymer is less than 60 °C [129], for a proper comparison, a temperature of 75 °C was chosen to ensure an environment identical to that used in earlier work for this assessment of the reliability of polymer [45]. The real lifetime thus might slightly differ from the estimated lifetime since the prerequisite of the Arrhenius assumption

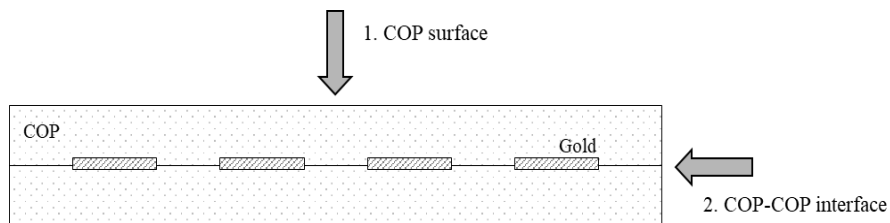


Figure 4.1.2 Possible leakage paths in the fabricated COP encapsulation: a COP surface and a COP-COP interface.

is inaccurate over 60 °C [129].

There can be two leakage paths in the fabricated COP encapsulation as shown in Figure 4.1.2. One path can be formed through a COP surface, and the other can be an interface between two COP films thermally laminated. Between the two possible leakage paths, it was thought that the limiting factor to the long-term reliability of the COP encapsulation could be the COP-COP interface with the following three reasons. First, in the tests, there was the proportional relation between the estimated lifetime and the applied pressure. The pressure was an

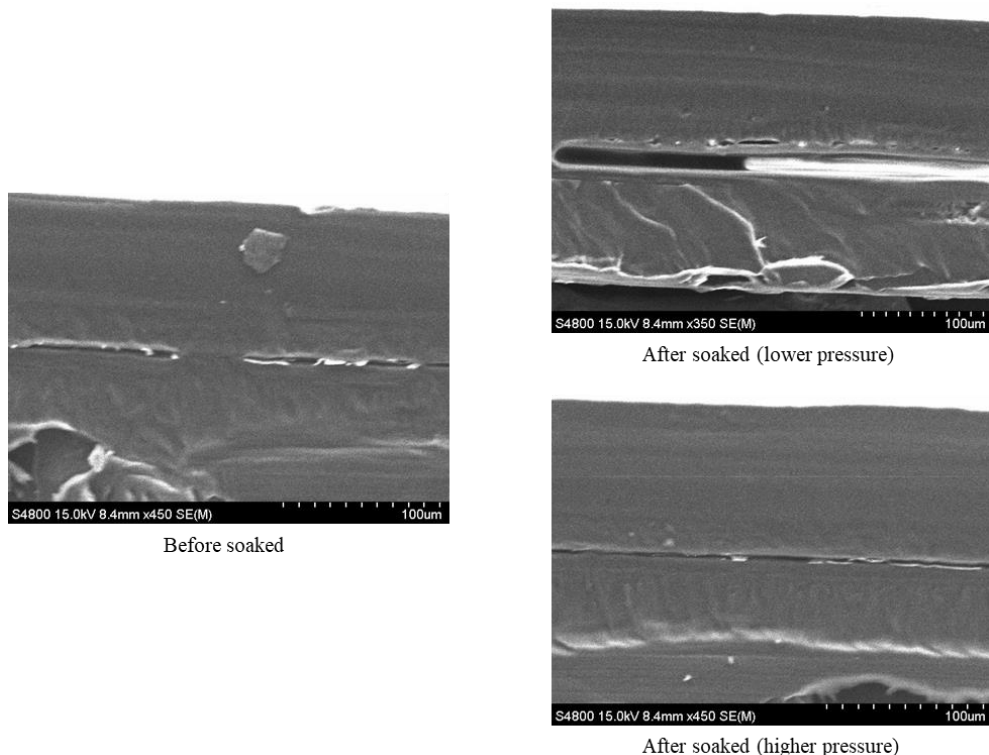


Figure 4.1.3 SEM images of cross-sections of the COP encapsulation before and after aging. After soaked, delamination was observed in both of the specimens fabricated under lower pressure and higher pressure.

important factor that can affect the adhesion between two COP films, thus can make the bonding of the two tight or can weaken the bonding. The second reason was based on results from LCP encapsulation similarly fabricated by thermal lamination in the previous research [117]. The fact that the limiting factor of thermally laminated polymer-based encapsulation may be polymer interfaces was proven by calculation as well as *in vitro* evaluation. Lastly, cross-sections of the COP encapsulation before and after aging were examined by a scanning electron microscope (SEM, S-4800, Hitachi, Japan), as shown in Figure 4.1.3. After soaked, delamination was observed in both of the specimens fabricated under lower pressure and higher pressure; more severe detachment was detected in the specimen encapsulated under lower pressure. Therefore, in order to further improve the long-term reliability of COP encapsulation, a method of enhancing the bonding of an interface can be applied. Surface treatment with plasma or more optimized process conditions may be used [47, 117].

In addition, optical transparency is one of attracting features of COP, which was used only for laser machining in the developed fabrication process. Optically transparent encapsulation is highly required in fabrication of certain implantable devices that demand the transmission of optical signals through encapsulating materials, such as retinal implants or optogenetic applications. In terms of optically transparent encapsulation, polymer has the same distinct advantages compared with opaque metal or ceramic. However, conventional transparent encapsulating polymer materials, such as polyimide, parylene-C, or polydimethylsiloxane, have insufficient reliability in a physiological environment, with their lifetimes of less than five years [31, 45].

To overcome this insufficient reliability, LCP has been researched for the superior reliability relative to that of other polymer materials, however, not all implantable devices can be encapsulated with LCP. For example, the opacity of LCP makes it challenging to seal the implantable devices that require the transmission of optical signals. The feasibility of LCP as an encapsulating material for photodiode-based retinal implants was investigated in the previous research by measuring the light transmittances of thinned LCP films [87]. A light transmittance of 20 % was guaranteed with an 8.28- μm -thick LCP film, but this level was too low to be transparent. Therefore, optical transparency of COP was herein evaluated as well for future uses in transparent encapsulation. A customized optical experimental test setup was built for light transmission tests as illustrated in Figure 4.1.4, and effects of thermal lamination on optical properties of COP were verified by measuring light

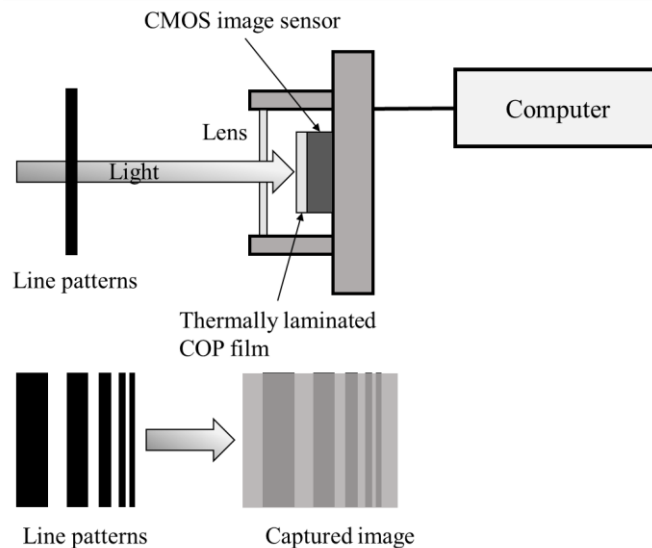


Figure 4.1.4 An illustration of a customized optical experimental setup for light transmission tests using thermally laminated COP films.

transmittances and minimum distinguishable line pitches.

Light transmission tests were conducted to evaluate light transmittances and the maximum resolution that can be achieved by COP films thermally laminated at various thicknesses. Two COP films were adhered to each other using the heating press without any internal materials (with process conditions of 235 °C, 0.509 MPa, and 40 seconds). Thereby, established thicknesses of the thermally laminated COP films were 26, 63, 113, 201, and 376 μm. As control experiments, the same light transmission tests were also carried out without COP films and with one bare 13-μm-thick COP film.

The customized optical experimental setup shown in Figure 4.1.4 used a commercial image sensing module containing an image sensor (OV7670, OmniVision Technologies, Inc., USA). The image sensor was covered with one of the thermally laminated COP films of different thicknesses during each light transmission test (Figure 4.1.4). Black and white line patterns of logarithmically varying pitches were projected onto the image sensor. From captured images, the light transmittances were evaluated. In addition, the contrast was calculated from a modulation transfer function (4.3; MTF , MTF) versus the spatial frequency with the modulation depth (4.2; M , M), which is correspondingly expressed as

$$M = \frac{A_{\max} - A_{\min}}{A_{\max} + A_{\min}} \quad (4.2)$$

and

$$MTF = \frac{M_{\text{image}}(f_s)}{M_{\text{object}}}, \quad (4.3)$$

where A is the light intensity, M_{image} is the modulation depth of a captured image,

M_{object} is the modulation depth of the line patterns, and f_s is the spatial frequency [130].

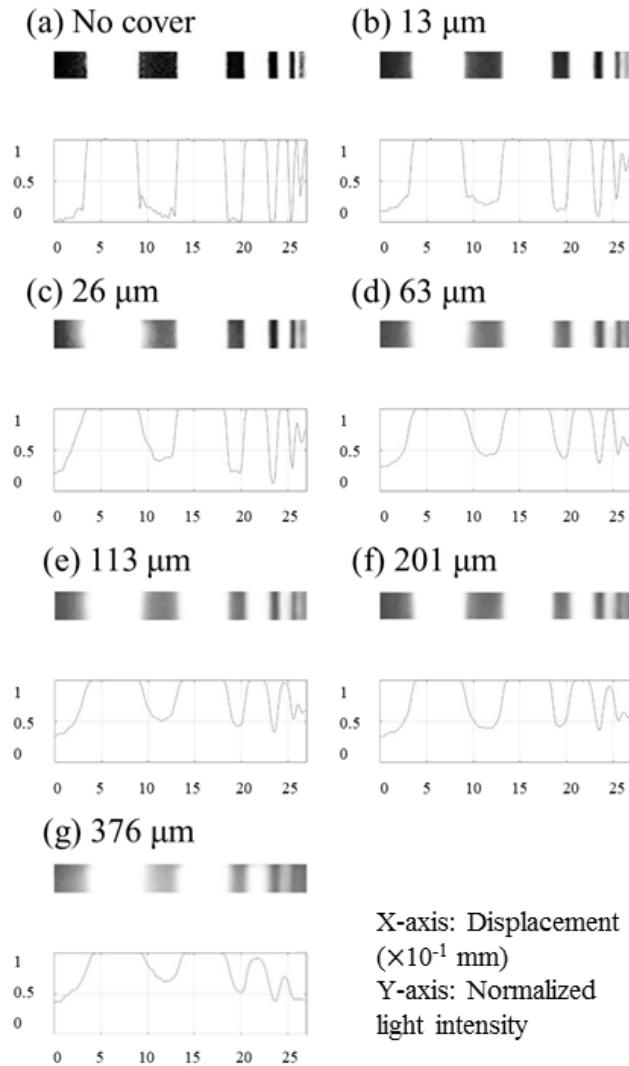


Figure 4.1.5 Captured images of the black and white line patterns and normalized light intensity outcomes along the horizontal displacement: (a) uncovered and covered by (b) a 13- μm -thick bare COP film and thermally laminated COP films whose thicknesses were (c) 26 μm , (d) 63 μm , (e) 113 μm , (f) 201 μm , and (g) 376 μm , respectively.

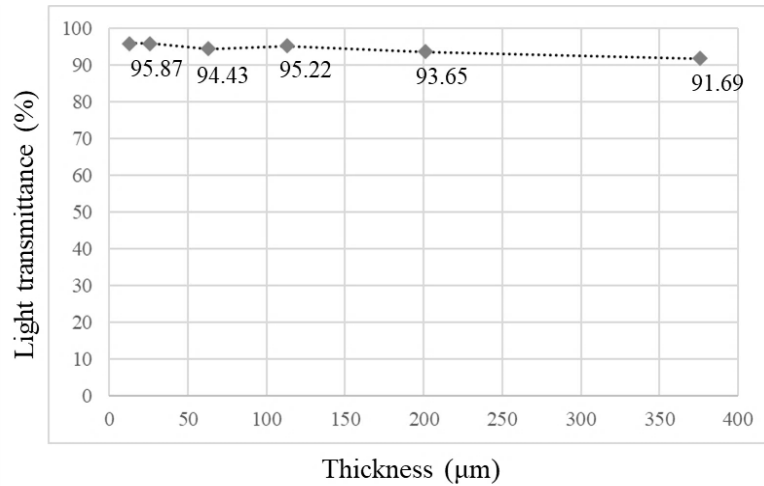


Figure 4.1.6 Measured light transmittances of thermally laminated COP films with varying thicknesses. Both light transmittances of the 13-µm-thick bare COP film and the 26-µm-thick thermally laminated COP film were identical to 95.87 %. The light transmittances of the 63-µm-, 113-µm-, 201-µm-, and 376-µm-thick thermally laminated COP films were 94.43, 95.22, 93.65, and 91.69 %, respectively.

Figure 4.1.5 presents captured images of the black and white line patterns and normalized light intensity outcomes along the horizontal displacement as obtained by the image sensor. In addition, Figure 4.1.6 shows the measured light transmittances of thermally laminated COP films with varying thicknesses. Compared with the data without COP films, the data from the image sensor covered by the 13-µm-thick bare COP film presented a light transmittance of 95.87 %, which was identical to that of the 26-µm-thick thermally laminated COP film. The light transmittance of thermally laminated COP films thinner than 376 µm exceeded 91.69 %.

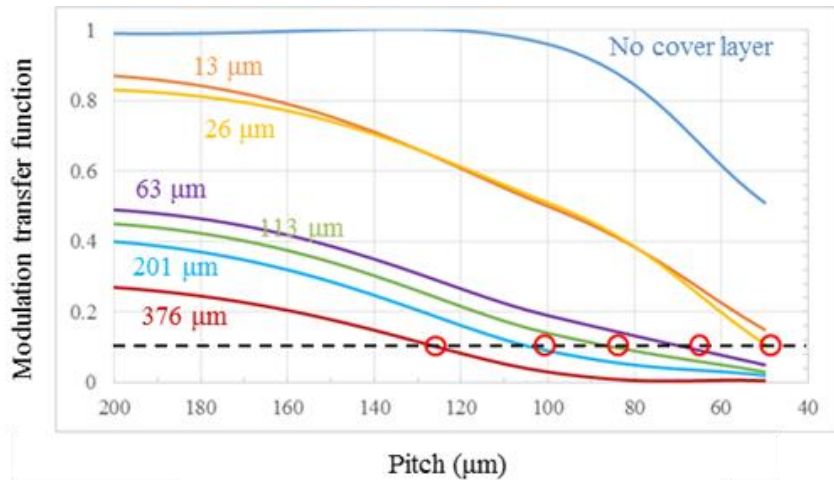


Figure 4.1.7 Calculated MTFs from the light transmission tests. The threshold level (the black dashed line) represents 10 % of MTF of the image captured without a COP film (the intersection at a 47.6 μm line pitch for the 26- μm -thick thermally laminated COP film).

Furthermore, the MTFs were quantitatively calculated as shown in Figure 4.1.7. A higher spatial frequency led to a lower MTF as a result of light scattering. The MTFs of the images with the thermally laminated COP films were compared with that of the uncovered image to determine the maximum resolution of the COP encapsulation. The maximum resolution was regarded as the spatial frequency at which an MTF was less than an acceptable threshold level of one tenth of the MTF from the uncovered image [87]. As a result, the minimum distinguishable line pitch of the 26- μm -thick thermally laminated COP film was 47.6 μm , which provided contrast similar to that of the 13- μm -thick bare COP film.

The light transmittances and the maximum resolution of the COP films, even after thermal lamination, were superior to those of LCP films, whose light

transmittance and minimum distinguishable line pitch were 20 % and 90 μm , respectively, at a thickness of 8.28 μm . For thermally laminated COP films, as the thicknesses was increased, a greater amount of light scattering occurred. Based on this result, optically transparent encapsulation using COPs can be developed as means by which to minimize lamination in areas where light will be transmitted.

There could be many potential applications of such optically transparent encapsulation based on COP, as depicted in Figure 4.1.8. One could be in retinal implants. The minimum distinguishable line pitch in this case was 47.6 μm , which is equivalent to ideally 4,400 channels in a macular area of 10 mm^2 . Another

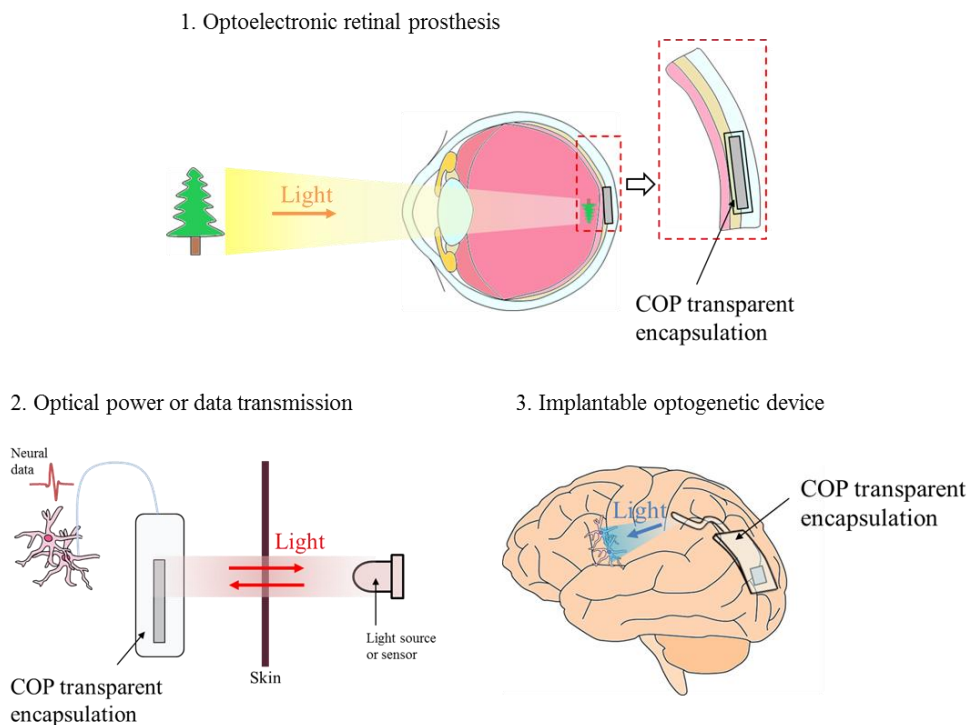


Figure 4.1.8 Illustrations of potential applications using COP-based optically transparent encapsulation.

application can be for the optical transmission of neural data to a receiver outside the body. Optical transmission involves rapid data rates up to tens of Gbps, which may improve the acquisition and transmission of big data in a neural form. Furthermore, in optogenetics, optical neural stimulation can be performed when stimulators are fully encapsulated and totally implanted *in vivo*.

4.2. Penta-Polar Stimulation

4.2.1. Designed IC and Electrode Configurations

The custom-designed ASIC successfully operated for the penta-polar stimulation and produced focused as well as steered electric field distribution with

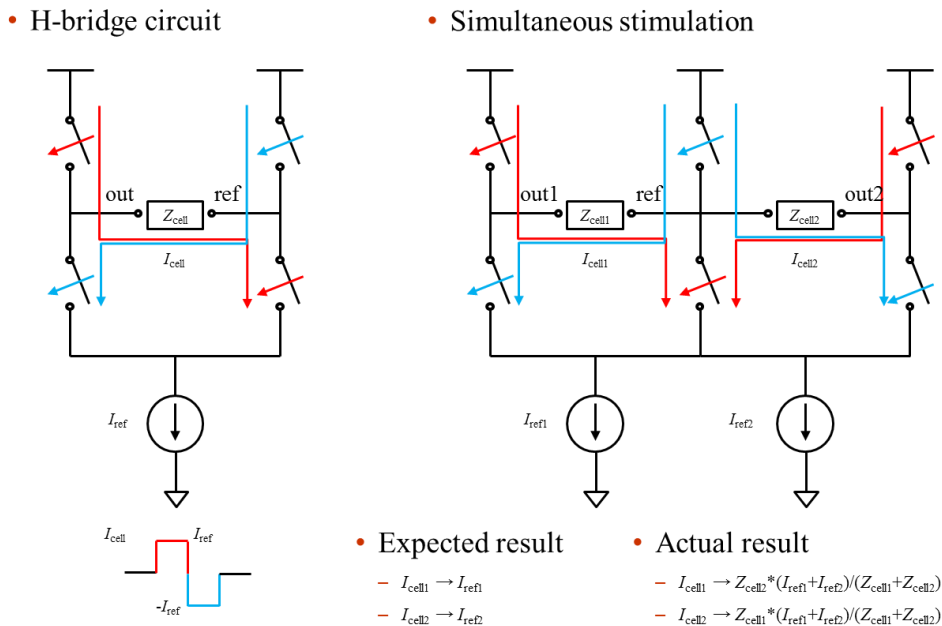


Figure 4.2.1 Detailed description on the reason why an H-bridge circuit is unable to be used for simultaneous stimulation.

the COP-based surface-type electrodes. The ASIC operation of five-channel simultaneous stimulation was feasible by devising the BCGs not to share the reference of the ASIC. Generally, an H-bridge circuit is used for biphasic current generation as described in Figure 4.2.1. However, if H-bridges are used for simultaneous stimulation, every biphasic current pulse might be summed together and divided by a resistance ratio between each output channel and a reference of stimulation circuits because all H-bridges share the same reference. Hence, an H-bridge is unable to be used for simultaneous stimulation such as the penta-polar stimulation.

The penta-polar stimulation was used for low-power but effective stimulation based on virtual channel generation. Five biphasic current pulses were considered as the minimum number needed to steer electric fields in four directions, like cardinal directions, in two dimensions. Thus, the grid-shaped arrangement of stimulation electrodes was chosen because it consists of one center electrode and four peripheral electrodes, compared with the honeycomb-shaped configuration

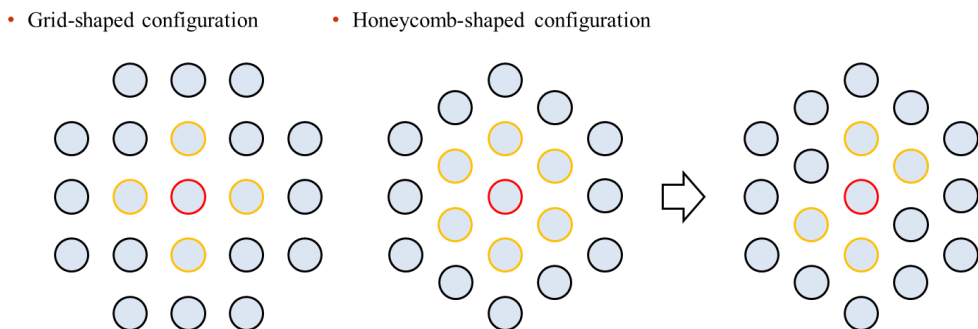


Figure 4.2.2 The grid-shaped and the honeycomb-shaped arrangement of stimulation electrodes controlled by the penta-polar stimulation.

using one center electrode and six peripheral electrodes. Nevertheless, this has no mean that the penta-polar stimulation only can control the grid-shaped configuration. As depicted in Figure 4.2.2, the penta-polar stimulation can cooperate with the honeycomb-shaped configuration, though the number of steerable directions would decrease.

4.2.2. Virtual Channels in Two Dimensions

The effectiveness of the penta-polar stimulation on focusing electric fields and generating virtual channels was verified. Although both results of the FEA and the *in vitro* evaluation did not exactly coincide, they showed the same information on the tendency of focusing electric fields and virtual channel generation as evaluated above. This also indicates that FEA can be sufficient to confirm only the tendency, but *in vitro* evaluation is highly required for precise stimulation using virtual channels in practice.

From the results, especially the fact that virtual channels demand a certain distance from physical electrodes was proven. In this case, such a distance was about 150 μm , and more virtual channels in two dimensions were estimated along another direction *in vitro* as shown in Figure 4.2.3. This distance must be considered in design procedures of stimulation electrodes for precisely steering virtual channels. For example, the thickness of a passivation layer of stimulation electrodes can be adjusted to be identical to the distance, or a medium such as hydrogel can be placed between target neurons and stimulation electrodes to match the distance. As for such virtual channel generation, further researches would be required for different

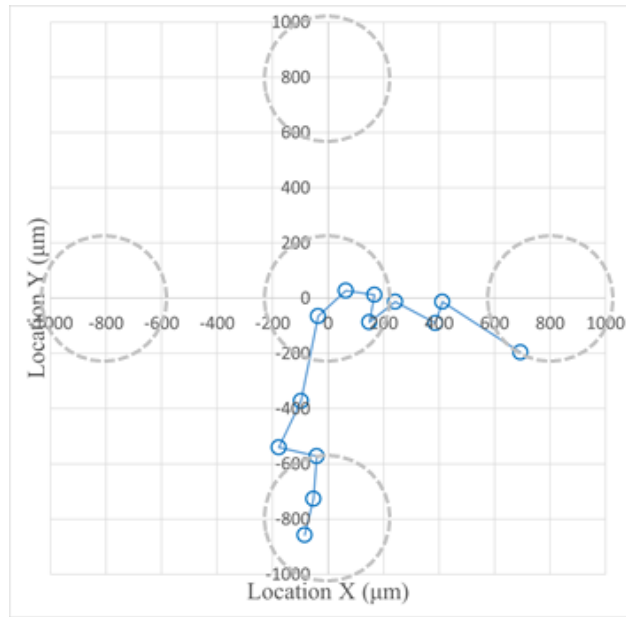


Figure 4.2.3 More virtual channels created *in vitro* by the penta-polar stimulation along another direction in two dimensions at the distance from the stimulation electrodes of 150 μm , the optimal distance for virtual channel generation herein.

configurations of physical electrodes in the future.

4.3. Implantable Camera

The implantable camera was proposed as a new image acquisition approach for a visual prosthetic system and developed. The current consumption of the implantable camera was minimized using the low-power components and communication protocol. As shown in Figure 4.3.1, a surface temperature of the implantable camera rose less than 3 $^{\circ}\text{C}$ even in continuous operation for an hour, and the package seemed to be good at heat dissipation due to the saturation of the temperature. Its size was miniaturized to have a diameter of 19.7 mm and a weight

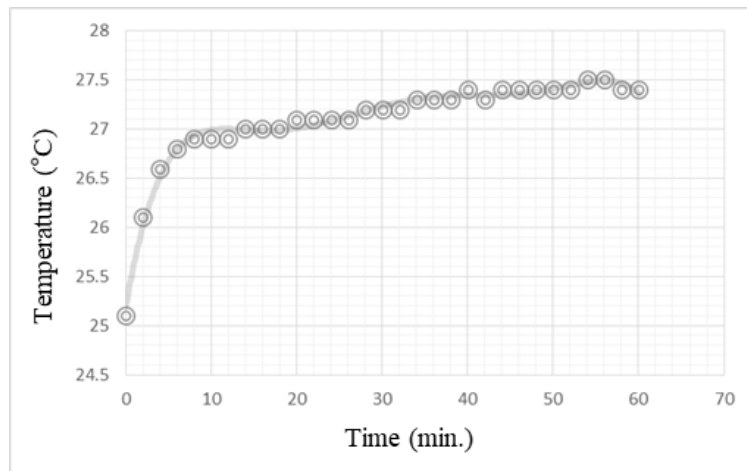


Figure 4.3.1 A surface temperature of the implantable camera measured for an hour in continuous operation.

of 5.75 g by the circuit design of the three-layered structure; the implantable camera thereby had an enough size to be inserted into the human eye with an averaged diameter of 24 to 25 mm [131].

The power module was inevitably separated from the implantable camera and connected by a polyimide cable, because a length of the rechargeable battery with the sufficiently large capacity of 100 mAh was more than 25 mm. As the performance of a rechargeable battery improves, it can be wholly implanted in the eye. Still, the separated power module have several advantages of helping stable power supply to the implantable camera while achieving its operating time estimated to be about eight hours with the nominal capacity of 100 mAh. In addition, the cable between the implantable camera and the power module could be used to fix the implantable camera when implanted in the eye, so that the pinhole lens can be located right behind the cornea. If this structure based on these advantages is used as it is for

a future implantable camera, it may be configured in a way that only an image sensor is partially implanted under the retina and connected to a power module with a wireless transceiver. Unlike conventional retinal implants, such a configuration has no need of a laser apparatus for high power supply because of the cooperating power module and can garner a variety of image information based on the complete camera structure [15, 27].

The functionality of the implantable camera was evaluated by the wireless image acquisition tests and the SNR measurements. In the wireless image acquisition tests, the implantable camera captured real-time images of the text, processed the images according to the preset configurations, and transmitted them to the image receiver. The images of the text were successfully displayed on a computer linked with the receiver. Furthermore, in the SNR measurements, the SNR of received signals at the receiver was measured with the varying communication distances and directions between the implantable camera and the receiver. Even when the implantable camera was covered by the biological medium, the communication range of the implantable camera was guaranteed up to 36.4 cm, which was a sufficient distance for reliable wireless communication between the eye and the visual cortex. Additionally, under this reliable communication range, the angle-dependency of the RSSI was also estimated as demonstrated in Figure 4.3.2, and it was shown that wireless radiation characteristics of the implantable camera were approximately angle-independent. One way to achieve a longer communication range might be to apply an antenna with larger transmit/receive power, but this was not the case herein because of the size constraints.

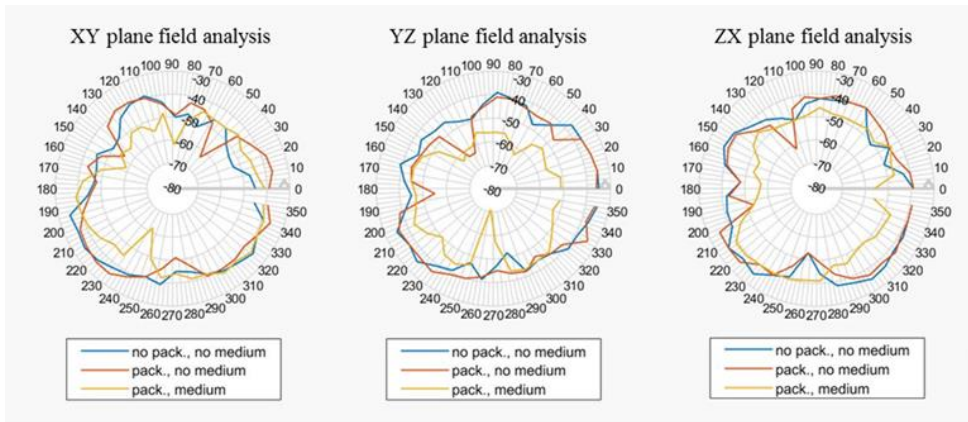


Figure 4.3.2 Radiation field analysis using the implantable camera to evaluate the angle-dependency of its wireless communication characteristics.

As listed in Table 4.3.1, the implantable camera can garner high-resolution images with a variety of information while tracking objects in accordance with natural eye movements, compared with the glasses-mounted camera and the MPDA. Because the implantable camera has these advantages, it can be useful especially in cooperating with a cortical visual prosthetic system that needs a large number of electrodes with a wide field of stimulation areas.

Table 4.3.1 Comparison of image acquisition approaches for visual prosthetic systems.

	Implantable camera	Glasses-mounted camera	MPDA
Image sensing area	2.36×1.76 mm	N/A	3.0×3.0 mm
The maximum number of pixels	307,200	N/A	1,600
Tracking objects in accordance with natural eye movements	O	X (needs more complicated hardware and software)	O

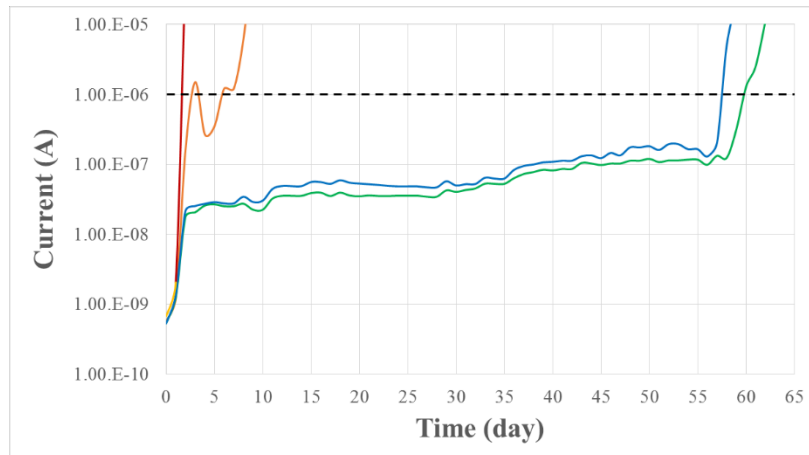


Figure 4.3.3 Leakage current measurements during accelerated aging. The red and orange lines showed the leakage currents of the elastomer-sealed samples without the epoxy coating. The green and blue lines indicated the leakage currents of the samples underwent both the epoxy coating and the elastomer sealing. The threshold level of 1 μ A, expressed as the black dashed line, was set arbitrarily.

4.3.1. Enhanced Reliability by Epoxy Coating

In the packaging, the biocompatible epoxy was coated prior to the elastomer sealing to enhance the reliability of the implantable camera. To estimate effects of the epoxy on the reliability in a physiological environment, leakage current measurements during accelerated aging were performed using custom-made IDEs on FR-4 PCBs. These IDEs were divided into two groups; one group of the samples was sealed by the elastomer without the epoxy coating, and the other group was coated with the epoxy first and sealed by the elastomer. To accelerate aging, these samples of both groups were put into a bottle with PBS solution (Gibco #10010, Invitrogen Life Technologies, USA) and placed into a convection oven heated to

75 °C. During the measurements, a voltage of 2 V was regularly applied, and leakage currents flowing in each sample were measured using the pico-ammeter.

As a result, Figure 4.3.3 presents the leakage currents evaluated from the samples of the two groups. After soaked, there were drastic increases of the leakage currents within three days for the elastomer-sealed samples without the epoxy coating. In contrast, the samples underwent both the epoxy coating and the elastomer sealing were reliable with drastic increases after 55 days. Therefore, these results implied the effects of the epoxy for the enhanced reliability in a physiological environment.

4.4. Multi-Functional Handheld Remote Controller

The HNS-controller was developed and applied to remote control of neural stimulation for constructing the totally implantable system. The handheld and user-friendly interfaces of the HNS-controller were deeply considered for users to use the HNS-controller under various circumstances. The HNS-controller was designed to resemble a gamepad that can be comfortably held by users and provide user-friendly experiences using simple switches. In addition, the HNS-controller became handheld by operating with batteries. Its estimated operating time would be 25.86 hours, more than a day, with three parallel-connected batteries, each of which has a nominal capacity of 1,000 mAh.

The functionality of the HNS-controller was evaluated *in vivo* especially for avian navigation as well as *in vitro*. *In vitro* evaluation, the totally implantable stimulator wirelessly received control data of biphasic current pulses preset by the

HNS-controller and generated the pulses corresponding to the control data. Subsequently, the FRM region of a pigeon was stimulated *in vivo* through both percutaneous stimulation and remote control using the HNS-controller. Each pigeon in both *in vivo* experiments responded to biphasic current pulses with the same parameters and showed the same 180-degree turning-left behavior lasting 2.5 seconds.

The multi-functional properties of the HNS-controller were helpful in the abovementioned experiments. The HNS-controller supplied biphasic current pulses using the current stimulation ASIC on it. This function was used not only to precisely position a target nucleus prior to implantation of the totally implantable stimulator, but also to stimulate the target region percutaneously. Furthermore, the HNS-controller wirelessly charged the battery in the stimulator using the class-E PA connected to an inductive link. Due to limited capacity of a battery, this function of inductive charging was necessary to operate the stimulator regularly *in vivo* for a long time. These multiple functions of the HNS-controller were achieved based on an FPGA. Parallel execution of an FPGA helped the HNS-controller to process its entire operation relatively fast and accurately. The multiple functions of the HNS-controller are briefly discussed in the next section.

In the future, more improvements on the HNS-controller will be required to transmit larger amount of data with higher data rate and accuracy to a multi-channel totally implantable stimulator connected to multiple electrodes.

4.4.1. Brief Discussions of the Two Extra Functions

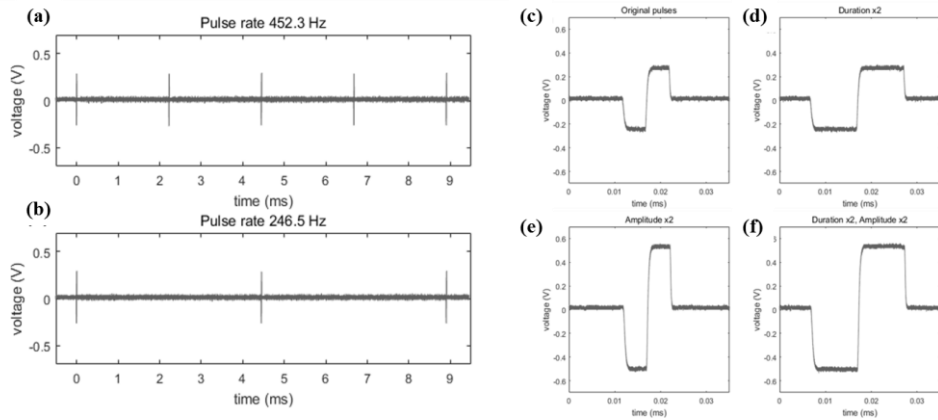


Figure 4.4.1 Biphasic current pulses generated from the current stimulation ASIC on the HNS-controller, which were measured by varying pulse rates, durations, and amplitudes: the current pulses at the pulse rate of (a) 452.3 Hz and (b) 246.5 Hz, and the current pulse at the duration and the amplitude of (c) 0.010 ms and 0.107 mA, (d) 0.020 ms and 0.107 mA, (e) 0.010 ms and 0.190 mA, and (f) 0.020 ms and 0.190 mA, respectively.

Figure 4.4.1 shows biphasic current pulses generated from the current stimulation ASIC on the HNS-controller for percutaneous stimulation, which were varied with several pulse rates, durations, and amplitudes. Though the ASIC was fundamentally designed to generate biphasic current pulses in pulse rates, durations, and amplitudes of 20.00–226.0 Hz, 0.020–1.280 ms, and 0.010–10.23 mA, respectively, these parameter ranges can be varied to be 40.70–452.3 Hz, 0.010–0.636 ms, and 0.010–10.23 mA by doubling a clock signal input to the ASIC. To measure the actual value of amplitude, a 3 k Ω resistor was connected to a load of the ASIC. This function can be used not only for precise positioning target neurons prior to implantation of a totally implantable stimulator, but also for percutaneous

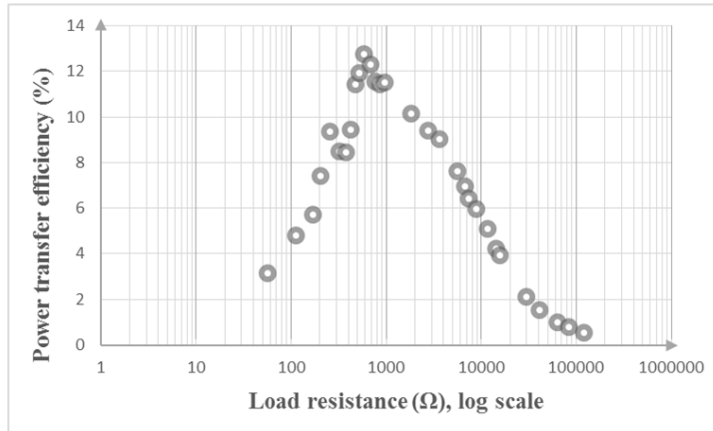


Figure 4.4.2 A graph of power transfer efficiency measured by varying a load resistance of a totally implantable stimulator from 56.1 Ω to 120 k Ω .

stimulation on the target neurons.

Figure 4.4.2 depicts power transfer efficiency through an inductive link connected with the HNS-controller measured by varying a load resistance of a totally implantable stimulator from 56.1 Ω to 120 k Ω . To implement an inductive link, a transmitter coil with a diameter of 25 mm, inductance of 13.0 μH , and series resistance of 7.8 Ω was designed on an FR-4 PCB. A receiver coil with a diameter of 15 mm, inductance of 2.8 μH , and series resistance of 8.3 Ω was fabricated on a polyimide substrate. Operating frequencies of the two coils separated by 1.6 mm were set to be both 2.5 MHz. The efficiency was calculated by dividing the power received at the receiver coil of the stimulator by the power consumed at the transmitter coil, which was connected to the class-E PA on the HNS-controller. From the results, the maximum transmitted power was measured to be 16.7 mW at the load resistance of 569 Ω , with the power transfer efficiency of 12.8 %.

The measured power and power transfer efficiency was sufficient to charge a rechargeable battery in a totally implantable stimulator, but also can be improved for better performance. Such low power transfer efficiency is mainly due to loose coupling between two coils constructing an inductive link. This can be improved by modifying specifications of a transmitter coil and a receiver coil to achieve somewhat of a coupling coefficient and a distance between the coils as in the following references [68, 132]. Specifications of a transmitter coil were calculated while the receiver coil remains unchanged, in order to achieve the coupling coefficient k and the distance d among the coils to be 0.4 and 10 mm, respectively, as follows.

First, the quality factor of a loading network (Q_L) was determined to calculate an inductance of a transmitter coil (L_1). It was assumed that only the current stimulation ASIC affected an actual load resistance of a totally implantable stimulator (R_{load} of 406 Ω). In the inductive charging, a proper value of Q_L (4.4) was selected to be 5, which was considered to be suitable for the optimization [68]:

$$Q_L = \frac{2\pi f L_1}{R_{total}} = 5. \quad (4.4)$$

To find L_1 from Q_L , the total load resistance seen by the class-E PA (R_{total}) can be expressed as follows (4.5),

$$R_{total} = R_L + R_{L1} + R_{Cp} + 1.365R_{on} + 0.2116R_{Cs}, \quad (4.5)$$

where R_L is the load resistance seen by the transmitter coil, R_{L1} is the effective series resistance of the transmitter coil, and R_{on} , R_{Cp} , and R_{Cs} are the on-resistance of a power transistor, the effective series resistance of parallel capacitors, and the effective series resistance of series capacitors of the class-E PA, respectively [132].

Because R_{on} , R_{Cp} , and R_{Cs} were measured to be less than 0.1Ω , they were assumed to be negligible. Then, R_L (4.6) follows

$$R_L = \frac{(2\pi fM)^2}{R_{load}}, \quad (4.6)$$

where f is the operating frequency, which was 2.5 MHz in this study, and M is the mutual inductance between the coils (4.7):

$$M = k\sqrt{L_1L_2}. \quad (4.7)$$

The mutual inductance M can be calculated as represented above, where L_2 is an inductance of the receiver coil. Using (4.4)-(4.7) and the values given above, the equation of L_1 and R_{L1} can be obtained as shown in (4.8):

$$L_1 = \frac{R_{L1}}{2.87 \times 10^6}. \quad (4.8)$$

From the equation, L_1 was calculated to be $0.348 \mu\text{H}$ if R_{L1} was 1Ω .

As the characteristics of the transmitter coil were obtained, the optimal power transfer efficiency η_{opt} can be calculated as,

$$\eta_{opt} = \frac{k^2 Q_1 Q_2}{(1 + \sqrt{1 + k^2 Q_1 Q_2})^2}, \quad (4.9)$$

where Q_1 and Q_2 are the quality factors of the transmitter coil and the receiver coil, respectively [132]. From the results above, η_{opt} was calculated to be 40.8 %. The power transfer efficiency can be increased more than three times compared to the experiment result.

In addition, it was reported that the maximum coupling coefficient k between two coils occurred when a diameter of a transmitter coil d_1 satisfied the following equation (4.10), where d_2 is a diameter of a receiver coil [68]:

$$d_1^2 = d_2^2 + 4d^2. \quad (4.10)$$

By increasing coupling coefficient k , the power transfer efficiency can be more optimized than the result calculated when k was assumed to be 0.4. In our design, d_1 was calculated to be 25 mm using (4.10). By this process, a transmitter coil that could be connected to the HNS-controller can be optimized if a receiver coil is fixed for a totally implantable stimulator.

4.5. Totally Implantable Visual Prosthetic System

Figure 4.5.1 describes the suggested totally implantable visual prosthetic system constructed by the integration with the COP-based fabrication, the penta-polar stimulation, the implantable camera, and the handheld remote controller.

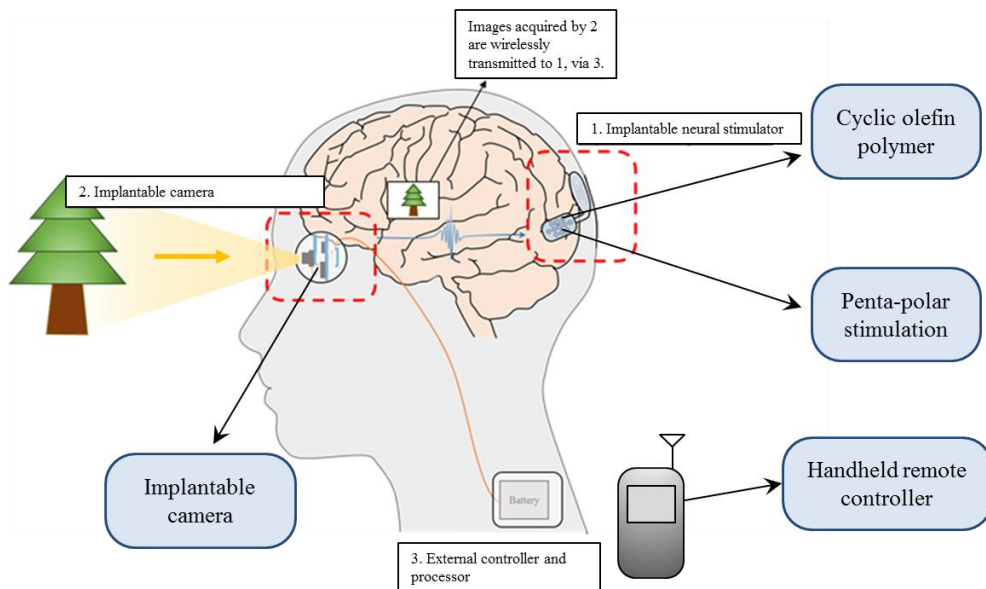


Figure 4.5.1 A conceptual view of the suggested totally implantable visual prosthetic system constructed by the integration with the COP-based fabrication, the penta-polar stimulation, the implantable camera, and the handheld remote controller.

As mentioned above, the target of the suggested visual prosthetic system was chosen as the visual cortex due to the implantable camera, which should be applied to blind patients underwent eye enucleation first. The implantable camera has advantages of obtaining real-time images with high resolution while focusing on objects in accordance with natural eye movements. These merits not only help blind patients to see the real world similarly with normal vision, but also improve their spatial perception by wide-field and precise visual cortex stimulation based on the abundant image information. The sophisticated images acquired by the implantable camera can be transmitted through the handheld remote controller after processed. On the other hand, these images also can be sent to the neural stimulator directly because the reliable communication range of the implantable camera is longer than the distance between the eye and the visual cortex.

The handheld neural stimulator features the expanded applicability with the multiple functions, such as percutaneous stimulation, inductive charging of a battery in the neural stimulator, and remote neural stimulation control, apart from the user-friendly interfaces. The percutaneous stimulation can be used for precise positioning the neural stimulator prior to its implantation. The inductive charging and the remote control can be performed occasionally and intentionally by users to assure the operation of the neural stimulator by stable power supply and data transmission. Although not available at this moment, several functions as an image processor can be integrated with the controller because there is plenty of room spatially in the controller.

The neural stimulator can be simply fabricated using COP as well as

employing the penta-polar stimulation for more delicate neural stimulation. Circuits for the neural stimulator can be designed similar to those of the totally implantable stimulator used in the evaluations using the handheld remote controller; the current stimulation ASIC can be replaced with the penta-polar stimulation ASIC. Though the visual cortex has the largest size to be stimulated than the retina and the optic nerve, it is challenging to realize super-high-density electrodes as well as connections to the neural stimulator. Using the penta-polar stimulation with the virtual channel generation, with a small number of stimulation electrodes, precise and high-resolution stimulation can be performed, thereby increasing the spatial efficiency. Nonetheless, due to effects of electrode configurations on virtual channel generation, the configurations must be carefully considered and simulated to effectively create virtual channels. Such stimulation electrodes can be simply fabricated by the COP-based process, and the COP-based electrodes were proved to have sufficient stiffness and functionality to be used for brain stimulation.

Furthermore, COP also can be leveraged in the encapsulation of the neural stimulator with the estimated lifetime of more than eight years, which was longer than those of polyimide and parylene-C and can be enhanced by optimizing the process conditions during thermal lamination. Thereby, the COP-based fabrication and encapsulation can be conducted for future monolithic integration, both enabling device miniaturization and lowering the manufacture cost as well as eliminating feedthroughs that may form small gaps through which moisture and ions can penetrate.

In the future, the suggested totally implantable visual prosthetic system

Table 4.5.1 A comparison table among visual prosthetic systems including the suggested totally implantable visual prosthetic system in this dissertation.

	This study	Retinal prosthesis	Optic nerve stimulation	Cortical visual prosthesis
Target size	3,495 mm ³ (primary visual cortex)	3.3×3.3 mm	1–3 mm diameter (section) 18–25 mm length (intraorbital part)	3,495 mm ³ (primary visual cortex)
System configuration	Totally implantable	Partially implantable	Partially implantable	Partially implantable
Image acquisition approach	Implantable camera	Glasses-mounted camera, MPDA	Glasses-mounted camera	Glasses-mounted camera
Electrode type	Depth, Surface	Surface	Cuff, Depth	Depth, Surface
Substrate material	COP	Titanium, Polyimide, LCP	N/A	N/A
Power and data transmission	Rechargeable battery, wireless communication protocol	Inductive link	N/A	Inductive link
Related diseases	Believed to restore damaged vision of the blind due to different causes, including both retina and optic nerve damages	Retinitis pigmentosa, Age-related macular degeneration	A variety of causes including retinal degeneration	Believed to restore damaged vision of the blind due to different causes, including both retina and optic nerve damages

would be constructed with these distinct and outstanding advantages, based on this study. Unlike conventional partially implantable visual prosthetic systems, the suggested totally implantable one can provide blind patients with benefits to perform several ordinary activities, such as sleep, shower, or running. In addition, the suggested totally implantable system can remove the possibility of functional failure as a result of unpredictable external damages as well as cosmetic issues.

Chapter 5

Conclusion

In this dissertation, a novel, totally implantable visual prosthetic system is suggested based on overall four researches conducted as in the following: 1) simple fabrication of implantable parts, such as micro-sized electrodes and a package, for a neural stimulator based on COP without semiconductor techniques, 2) penta-polar stimulation for virtual channel generation to overcome a limited number of physical electrodes in a confined space, 3) a new image acquisition strategy using an implantable camera, and 4) a handheld remote control for a totally implantable neural stimulation system without hindering patient's various activities.

Simple fabrication process of implantable units was developed using COP, which has biocompatibility, high transparency, and strong adhesion to gold. This fabrication process is simpler and faster without masks, vacuum, and huge fabrication facilities than metal deposition and photolithography techniques. A COP-based depth-type microprobe was firstly fabricated by the developed process. Based on COP films stacked in multiple layers, this microprobe features controllable stiffness regarding its thickness. Because of this stiffness, the functionality of the microprobe was elucidated through simultaneous multichannel neural signal recording in the left SI region of a rat. Furthermore, COP was introduced as an encapsulating material for implantable devices. The *in vitro* reliability test results validated the long-term reliability of the COP encapsulation.

In addition, virtual channels were generated by penta-polar stimulation. The purpose was to apply virtual channels in two dimensions, thus the penta-polar stimulation ASIC and the stimulation electrodes arranged in a cross shape were designed. The effectiveness of the penta-polar stimulation was evaluated by

comparing with mono-polar stimulation. Furthermore, virtual channels were estimated in accordance with a distance from the stimulation electrodes, while varying an amplitude ratio of the simultaneous stimuli. In conclusion, the effectiveness was verified and found the distance-dependency of virtual channel generation using the penta-polar stimulation.

An implantable camera was proposed and developed as a new image acquisition approach for a visual prosthetic system. The implantable camera was fabricated in a spherical form by epoxy coating and elastomer sealing, enough to be inserted into the eye. Its operation was verified by wireless image acquisition that displayed a processed black and white image. Furthermore, even when the implantable camera was covered by a biological medium, its communication range was guaranteed up to 36.4 cm, which was a longer distance for reliable communication than a distance between the eye and the visual cortex.

A handheld remote controller for neural stimulation was developed. With ZigBee wireless communication, this controller becomes handheld by operating with batteries more than a day. In addition, simple switches make it easy to use the controller like a gamepad. Because of these handheld and user-friendly interfaces of the controller, users can manipulate it under various circumstances with no interference with their ordinary activities. The functionality and the feasibility of the controller were evaluated *in vivo*, especially in avian navigation. When the target nucleus was stimulated by remote control, the 180-degree turning-left behavior of a pigeon were consistently observed as the pigeon responded to percutaneous stimulation on the target nucleus.

This study foretells the development of the suggested totally implantable visual prosthetic system constructed by the integration with the COP-based fabrication, the penta-polar stimulation, the implantable camera, and the handheld remote controller with the following distinct and outstanding advantages in the future. Unlike conventional partially implantable visual prosthetic systems, the suggested totally implantable one can enable blind patients to perform several ordinary activities. In addition, the suggested totally implantable system can remove the possibility of functional failure as a result of unpredictable external damages as well as cosmetic issues, using the handheld remote controller. The COP-based fabrication and encapsulation can be carried out for simple fabrication as well as future monolithic integration, both enabling device miniaturization and lowering the manufacture cost as well as eliminating feedthroughs. Using the penta-polar stimulation with the virtual channel generation, precise and high-resolution stimulation can be performed, thereby increasing the spatial efficiency. The implantable camera provides advantages of obtaining real-time images with high resolution while focusing on objects in accordance with natural eye movements.

References

- [1] North, R. B., Ewend, M. G., Lawton, M. T., & Piantadosi, S. (1991). Spinal cord stimulation for chronic, intractable pain: superiority of “multi-channel” devices. *Pain*, *44*(2), 119–130.
- [2] Prochazka, A., Mushahwar, V. K., & McCreery, D. B. (2001). Neural prostheses. *The Journal of Physiology*, *533*(1), 99–109.
- [3] Alo, K. M., & Holsheimer, J. (2002). New Trends in Neuromodulation for the Management of Neuropathic Pain. *Neurosurgery*, *50*(4), 690–704.
- [4] Wilson, B. S., & Dorman, M. F. (2007). The Surprising Performance of Present-Day Cochlear Implants. *IEEE Transactions on Biomedical Engineering*, *54*(6), 969–972.
- [5] Picaud, S., & Sahel, J. A. (2014). Retinal prostheses: Clinical results and future challenges. *Comptes Rendus Biologies*, *337*(3), 214–222.
- [6] Morishita, T., Fayad, S. M., Higuchi, M. A., Nestor, K. A., & Foote, K. D. (2014). Deep Brain Stimulation for Treatment-resistant Depression: Systematic Review of Clinical Outcomes. *Neurotherapeutics*, *11*(3), 475–484.
- [7] Flint, R. D., Scheid, M. R., Wright, Z. A., Solla, S. A., & Slutzky, M. W. (2016). Long-Term Stability of Motor Cortical Activity: Implications for Brain Machine Interfaces and Optimal Feedback Control. *Journal of Neuroscience*, *36*(12), 3623–3632.
- [8] Loeb, G. E. (2018). Neural Prosthetics: A Review of Empirical vs. Systems Engineering Strategies. *Applied Bionics and Biomechanics*, 2018.
- [9] Rizzo, J. F., Snebold, L., & Kenney, M. (2007). Development of a Visual Prosthesis. In *Visual Prosthesis and Ophthalmic Devices* (pp. 71–93). Humana Press.
- [10] Weiland, J. D., & Humayun, M. S. (2008). Visual Prosthesis. *Proceedings of the IEEE*, *96*(7), 1076–1084.
- [11] Margalit, E., Maia, M., Weiland, J. D., Greenberg, R. J., Fujii, G. Y., Torres, G., Piyathaisere, D. V., O’Hearn, T. M., Liu, W., Lazzi, G., Dagnelie, G., Scribner, D. A., de Juan Jr, E., & Humayun, M. S. (2002). Retinal Prosthesis for the Blind. *Survey of Ophthalmology*, *47*(4), 335–356.
- [12] Troyk, P. R., Bradley, D., Bak, M., Cogan, S., Erickson, R., Hu, Z., Kufta, C., McCreery, D., Schmidt, E., Sung, S., & Towle, V. (2006, January). Intracortical Visual Prosthesis Research-Approach and Progress. In *2005 IEEE Engineering in*

Medicine and Biology 27th Annual Conference (pp. 7376–7379). IEEE.

- [13] Duret, F., Brelén, M. E., Lambert, V., Gérard, B., Delbeke, J., & Veraart, C. (2006). Object localization, discrimination, and grasping with the optic nerve visual prosthesis. *Restorative Neurology and Neuroscience*, 24(1), 31–40.
- [14] Sakaguchi, H., Kamei, M., Fujikado, T., Yonezawa, E., Ozawa, M., Cecilia-Gonzalez, C., Ustariz-Gonzalez, O., Quiroz-Mercado, H., & Tano, Y. (2009). Artificial vision by direct optic nerve electrode (AV-DONE) implantation in a blind patient with retinitis pigmentosa. *Journal of Artificial Organs*, 12(3), 206–209.
- [15] Mathieson, K., Loudin, J., Goetz, G., Huie, P., Wang, L., Kamins, T. I., Galambos, L., Smith, R., Harris, J. S., Sher, A., & Palanker, D. (2012). Photovoltaic retinal prosthesis with high pixel density. *Nature Photonics*, 6(6), 391–397.
- [16] Li, M., Yan, Y., Wu, K., Lu, Y., Sun, J., Chen, Y., Chai, X., Katz, S., Cao, P., Ma, Z., Sun, P., Ren, Q., & Li, L. (2017). Penetrative Optic Nerve-Based Visual Prosthesis Research. In *Artificial Vision* (pp. 165–176). Springer, Cham.
- [17] Fernández, E., & Normann, R. A. (2017). CORTIVIS Approach for an Intracortical Visual Prostheses. In *Artificial Vision* (pp. 191–201). Springer, Cham.
- [18] Troyk, P. R. (2017). The Intracortical Visual Prosthesis Project. In *Artificial Vision* (pp. 203–214). Springer, Cham.
- [19] Bloch, E., Luo, Y., & da Cruz, L. (2019). Advances in retinal prosthesis systems. *Therapeutic Advances in Ophthalmology*, 11, 1–16.
- [20] Luo, Y. H. L., & da Cruz, L. (2016). The Argus® II Retinal Prosthesis System. *Progress in Retinal and Eye Research*, 50, 89–107.
- [21] Kitiratschky, V. B. D., Stingl, K., Wilhelm, B., Peters, T., Besch, D., Sachs, H., Gekeler, F., Bartz-Schmidt, K. U., & Zrenner, E. (2015). Safety evaluation of “retina implant alpha IMS”-a prospective clinical trial. *Graefes Archive for Clinical and Experimental Ophthalmology*, 253(3), 381–387.
- [22] Hornig, R., Dapper, M., Le Joliff, E., Hill, R., Ishaque, K., Posch, C., Benosman, R., LeMer, Y., Sahel, J. A., & Picaud, S. (2017). Pixium Vision: First Clinical Results and Innovative Developments. In *Artificial Vision* (pp. 99–113). Springer, Cham.
- [23] 서울아산병원 인공망막 이식수술 국내 첫 성공. (2017, July 10). Retrieved October 31, 2019, from: <https://www.youtube.com/watch?v=v9nAqhP8Omc>.
- [24] Retinal Implant Market Size, Share & Trends Analysis Report By Device Type (Retina Implant Alpha AMS, Implantable Miniature Telescope, and Argus II), By Region, And Segment Forecasts, 2018-2026. (2018). Retrieved November 1, 2019,

from: <https://www.grandviewresearch.com/industry-analysis/retinal-implant-market>.

- [25] Klauke, S., Goertz, M., Rein, S., Hoehl, D., Thomas, U., Eckhorn, R., Bremmer, F., & Wachtler, T. (2011). Stimulation with a Wireless Intraocular Epiretinal Implant Elicits Visual Percepts in Blind Humans. *Investigative Ophthalmology & Visual Science*, 52(1), 449–455.
- [26] Fujikado, T., Kamei, M., Sakaguchi, H., Kanda, H., Morimoto, T., Ikuno, Y., Nishida, K., Kishima, H., Maruo, T., Konoma, K., Ozawa, M., & Nishida, K. (2011). Testing of Semichronically Implanted Retinal Prosthesis by Suprachoroidal-Transretinal Stimulation in Patients with Retinitis Pigmentosa. *Investigative Ophthalmology & Visual Science*, 52(7), 4726–4733.
- [27] Stingl, K., Bartz-Schmidt, K. U., Besch, D., Braun, A., Bruckmann, A., Gekeler, F., Greppmaier, U., Hipp, S., Hörtdörfer, G., Kernstock, C., Koitschev, A., Kusnyerik, A., Sachs, H., Schatz, A., Stingl, K. T., Peters, T., Wilhelm, B., & Zrenner, E. (2013). Artificial vision with wirelessly powered subretinal electronic implant alpha-IMS. *Proceedings of the Royal Society B: Biological Sciences*, 280(1757).
- [28] Lorach, H., Marre, O., Sahel, J. A., Benosman, R., & Picaud, S. (2013). Neural stimulation for visual rehabilitation: Advances and challenges. *Journal of Physiology-Paris*, 107(5), 421–431.
- [29] Fernandez, E. (2018). Development of visual Neuroprostheses: trends and challenges. *Bioelectronic Medicine*, 4(1).
- [30] Cogan, S. F. (2008). Neural Stimulation and Recording Electrodes. *Annual Review of Biomedical Engineering*, 10, 275–309.
- [31] Ahn, S. H., Jeong, J., & Kim, S. J. (2019). Emerging Encapsulation Technologies for Long-Term Reliability of Microfabricated Implantable Devices. *Micromachines*, 10(8).
- [32] Adunka, O., Kiefer, J., Unkelbach, M. H., Lehnert, T., & Gstoettner, W. (2004). Development and Evaluation of an Improved Cochlear Implant Electrode Design for Electric Acoustic Stimulation. *The Laryngoscope*, 114(7), 1237–1241.
- [33] Gimsa, J., Habel, B., Schreiber, U., van Rienen, U., Strauss, U., & Gimsa, U. (2005). Choosing electrodes for deep brain stimulation experiments—electrochemical considerations. *Journal of Neuroscience Methods*, 142(2), 251–265.
- [34] Li, L., Cao, P., Sun, M., Chai, X., Wu, K., Xu, X., Li, X., & Ren, Q. (2009). Intraorbital optic nerve stimulation with penetrating electrodes: in vivo

- electrophysiology study in rabbits. *Graefe's Archive for Clinical and Experimental Ophthalmology*, 247(3), 349–361.
- [35] Cheng, D. L., Greenberg, P. B., & Borton, D. A. (2017). Advances in Retinal Prosthetic Research: A Systematic Review of Engineering and Clinical Characteristics of Current Prosthetic Initiatives. *Current Eye Research*, 42(3), 334–347.
- [36] Choi, Y. I., Kim, K., & Lee, S. (2019). Fabrication and evaluation of nanostructured microelectrodes for high-spatial resolution in retinal prostheses. *Microsystem Technologies*, 25(5), 2099–2107.
- [37] Zeng, Q., Zhao, S., Yang, H., Zhang, Y., & Wu, T. (2019). Micro/Nano Technologies for High-Density Retinal Implant. *Micromachines*, 10(6).
- [38] Argus II: the life-changing retinitis pigmentosa treatment. (n.d.). Retrieved November 2, 2019, from: <https://www.secondsight.com/discover-argus>.
- [39] Cochlear™ Nucleus® System. (n.d.). Retrieved November 2, 2019, from: <https://www.cochlear.com/in/en/home/products-and-accessories/cochlear-nucleus-system>.
- [40] Deep Brain Stimulation. (n.d.). Retrieved November 2, 2019, from: <https://www.medtronic.com/us-en/healthcare-professionals/therapies-procedures/neurological/deep-brain-stimulation.html>.
- [41] Neural Probes. (n.d.). Retrieved November 2, 2019, from: <https://neuronexus.com/products/neural-probes>.
- [42] PRIMA Bionic Vision System. (n.d.). Retrieved November 2, 2019, from: <https://www.pixium-vision.com/en/technology-1/prima-vision-restoration-system>.
- [43] SYNCHRONY Cochlear Implant. (n.d.). Retrieved November 2, 2019, from: <https://www.medel.com/hearing-solutions/cochlear-implants/synchrony>.
- [44] Jeong, J., Lee, S. W., Min, K. S., Shin, S., Jun, S. B., & Kim, S. J. (2012). Liquid Crystal Polymer (LCP), an Attractive Substrate for Retinal Implant. *Sensors and Materials*, 24(4), 189–203.
- [45] Lee, S. W., Min, K. S., Jeong, J., Kim, J., & Kim, S. J. (2011). Monolithic Encapsulation of Implantable Neuroprosthetic Devices Using Liquid Crystal Polymers. *IEEE Transactions on Biomedical Engineering*, 58(8), 2255–2263.
- [46] Kim, J. H., Min, K. S., An, S. K., Jeong, J. S., Jun, S. B., Cho, M. H., Son Y. D., Cho, Z. H., & Kim, S. J. (2012). Magnetic Resonance Imaging Compatibility of the Polymer-Based Cochlear Implant. *Clinical and Experimental Otorhinolaryngology*, 5(Suppl 1), S19–S23.

- [47] Jeong, J., Bae, S. H., Min, K. S., Seo, J. M., Chung, H., & Kim, S. J. (2014). A Miniaturized, Eye-Conformable, and Long-Term Reliable Retinal Prosthesis Using Monolithic Fabrication of Liquid Crystal Polymer (LCP). *IEEE Transactions on Biomedical Engineering*, 62(3), 982–989.
- [48] Hassler, C., Boretius, T., & Stieglitz, T. (2011). Polymers for Neural Implants. *Journal of Polymer Science Part B: Polymer Physics*, 49(1), 18–33.
- [49] Eiber, C. D., Lovell, N. H., & Suaning, G. J. (2013). Attaining higher resolution visual prosthetics: A review of the factors and limitations. *Journal of Neural Engineering*, 10(1).
- [50] Wise, K. D., Bhatti, P. T., Wang, J., & Friedrich, C. R. (2008). High-density cochlear implants with position sensing and control. *Hearing Research*, 242(1–2), 22–30.
- [51] Viventi, J., Kim, D. H., Vigeland, L., Frechette, E. S., Blanco, J. A., Kim, Y. S., Avrin, A. E., Tiruvadi, V. R., Hwang, S. W., Vanleer, A. C., Wulsin, D. F., Davis, K., Gelber, C. E., Palmer, L., der Spiegel, J. V., Wu, J., Xiao, J., Huang, Y., Contreras, D., Rogers, J. A., & Litt, B. (2011). Flexible, foldable, actively multiplexed, high-density electrode array for mapping brain activity *in vivo*. *Nature Neuroscience*, 14(12), 1599–1605.
- [52] Wilke, R. G., Greppmaier, U., Stingl, K., & Zrenner, E. (2011). Fading Of Perception In Retinal Implants Is A Function Of Time And Space Between Sites Of Stimulation. *Investigative Ophthalmology & Visual Science*, 52(14), 458.
- [53] Wilke, R., Gabel, V. P., Sachs, H., Schmidt, K. U. B., Gekeler, F., Besch, D., Szurman, P., Stett, A., Wilhelm, B., Peters, T., Harscher, A., Greppmaier, U., Kibbel, S., Benav, H., Bruckmann, A., Stingl, K., Kusnyerik, A., & Zrenner, E. (2011). Spatial Resolution and Perception of Patterns Mediated by a Subretinal 16-Electrode Array in Patients Blinded by Hereditary Retinal Dystrophies. *Investigative Ophthalmology & Visual Science*, 52(8), 5995–6003.
- [54] Moghaddam, G. K., Lovell, N. H., Wilke, R. G., Suaning, G. J., & Dokos, S. (2014). Performance optimization of current focusing and virtual electrode strategies in retinal implants. *Computer Methods and Programs in Biomedicine*, 117(2), 334–342.
- [55] Meffin, H. (2013, September). What limits spatial perception with retinal implants?. In *2013 IEEE International Conference on Image Processing* (pp. 1545–1549). IEEE.
- [56] Dumm, G., Fallon, J. B., Williams, C. E., & Shivdasani, M. N. (2014). Virtual

- Electrodes by Current Steering in Retinal Prostheses. *Investigative Ophthalmology & Visual Science*, 55(12), 8077–8085.
- [57] Green, R., & Abidian, M. R. (2015). Conducting Polymers for Neural Prosthetic and Neural Interface Applications. *Advanced Materials*, 27(46), 7620–7637.
- [58] Loizos, K., Cela, C., Marc, R., & Lazzi, G. (2016). Virtual electrode design for increasing spatial resolution in retinal prosthesis. *Healthcare Technology Letters*, 3(2), 93–97.
- [59] Xiang, Z., Yen, S. C., Sheshadri, S., Wang, J., Lee, S., Liu, Y. H., Liao, L. D., Thakor, N. V., & Lee, C. (2016). Progress of Flexible Electronics in Neural Interfacing-A Self-Adaptive Non-Invasive Neural Ribbon Electrode for Small Nerves Recording. *Advanced Materials*, 28(22), 4472–4479.
- [60] Wellman, S. M., Eles, J. R., Ludwig, K. A., Seymour, J. P., Michelson, N. J., McFadden, W. E., Vazquez, A. L., & Kozai, T. D. (2018). A Materials Roadmap to Functional Neural Interface Design. *Advanced Functional Materials*, 28(12).
- [61] Won, S. M., Song, E., Zhao, J., Li, J., Rivnay, J., & Rogers, J. A. (2018). Recent Advances in Materials, Devices, and Systems for Neural Interfaces. *Advanced Materials*, 30(30).
- [62] Kim, C., Jeong, J., & Kim, S. J. (2019). Recent Progress on Non-Conventional Microfabricated Probes for the Chronic Recording of Cortical Neural Activity. *Sensors*, 19(5).
- [63] Wallhagen, M. I. (2009). The Stigma of Hearing Loss. *The Gerontologist*, 50(1), 66–75.
- [64] Mitchell-Innes, A., Morse, R., Irving, R., & Begg, P. (2017). Implantable microphones as an alternative to external microphones for cochlear implants. *Cochlear Implants International*, 18(6), 304–313.
- [65] Cohen, N. (2007). The Totally Implantable Cochlear Implant. *Ear and Hearing*, 28(2), 100S–101S.
- [66] Goffman, E. (2009). *Stigma: Notes on the Management of Spoiled Identity*. Simon and Schuster.
- [67] Catrysse, M., Hermans, B., & Puers, R. (2004). An inductive power system with integrated bi-directional data-transmission. *Sensors and Actuators A: Physical*, 115(2–3), 221–229.
- [68] Adeeb, M. A., Islam, A. B., Haider, M. R., Tulip, F. S., Ericson, M. N., & Islam, S. K. (2012). An Inductive Link-Based Wireless Power Transfer System for

Biomedical Applications. *Active and Passive Electronic Components*, 2012.

- [69] Yun, S., Koh, C. S., Jeong, J., Seo, J., Ahn, S. H., Choi, G. J., Shim, S., Shin, J., Jung, H. H., Chang, J. W., & Kim, S. J. (2019). Remote-Controlled Fully Implantable Neural Stimulator for Freely Moving Small Animal. *Electronics*, 8(6).
- [70] Liu, T., Bihr, U., Anis, S. M., & Ortmanns, M. (2012, August). Optical Transcutaneous Link for Low Power, High Data Rate Telemetry. In *2012 Annual International Conference of the IEEE Engineering in Medicine and Biology Society* (pp. 3535–3538). IEEE.
- [71] Theogarajan, L., Shire, D., Kelly, S., Wyatt, J. L., & Rizzo, J. (2009, April). Visual Prostheses: Current Progress and Challenges. In *2009 International Symposium on VLSI Design, Automation and Test* (pp. 126–129). IEEE.
- [72] Weiland, J. D., Cho, A. K., & Humayun, M. S. (2011). Retinal Prostheses: Current Clinical Results and Future Needs. *Ophthalmology*, 118(11), 2227–2237.
- [73] Winter, J. O., Cogan, S. F., & Rizzo, J. F. (2007). Retinal prostheses: current challenges and future outlook. *Journal of Biomaterials Science, Polymer Edition*, 18(8), 1031–1055.
- [74] Chestek, C. A., Cunningham, J. P., Gilja, V., Nuyujukian, P., Ryu, S. I., & Shenoy, K. V. (2009, September). Neural Prosthetic Systems: Current Problems and Future Directions. In *2009 Annual International Conference of the IEEE Engineering in Medicine and Biology Society* (pp. 3369–3375). IEEE.
- [75] Gilja, V., Chestek, C. A., Diester, I., Henderson, J. M., Deisseroth, K., & Shenoy, K. V. (2011). Challenges and Opportunities for Next-Generation Intracortically Based Neural Prostheses. *IEEE Transactions on Biomedical Engineering*, 58(7), 1891–1899.
- [76] Lewis, P. M., Ackland, H. M., Lowery, A. J., & Rosenfeld, J. V. (2015). Restoration of vision in blind individuals using bionic devices: A review with a focus on cortical visual prostheses. *Brain Research*, 1595, 51–73.
- [77] Foroushani, A. N., Pack, C. C., & Sawan, M. (2018). Cortical visual prostheses: from microstimulation to functional percept. *Journal of Neural Engineering*, 15(2).
- [78] Niketeghad, S., & Pouratian, N. (2019). Brain Machine Interfaces for Vision Restoration: The Current State of Cortical Visual Prosthetics. *Neurotherapeutics*, 16(1), 134–143.
- [79] Metz, S., Bertsch, A., Bertrand, D., & Renaud, P. (2004). Flexible polyimide probes with microelectrodes and embedded microfluidic channels for simultaneous drug

- delivery and multi-channel monitoring of bioelectric activity. *Biosensors and Bioelectronics*, 19(10), 1309–1318.
- [80] Lee, C. J., Oh, S. J., Song, J. K., & Kim, S. J. (2004). Neural signal recording using microelectrode arrays fabricated on liquid crystal polymer material. *Materials Science and Engineering: C*, 24(1–2), 265–268.
- [81] Lee, K., Singh, A., He, J., Massia, S., Kim, B., & Raupp, G. (2004). Polyimide based neural implants with stiffness improvement. *Sensors and Actuators B: Chemical*, 102(1), 67–72.
- [82] Pellinen, D. S., Moon, T., Vetter, R. J., Miriani, R., & Kipke, D. R. (2006, January). Multifunctional Flexible Parylene-Based Intracortical Microelectrodes. In *2005 IEEE Engineering in Medicine and Biology 27th Annual Conference* (pp. 5272–5275). IEEE.
- [83] Wester, B. A., Lee, R. H., & LaPlaca, M. C. (2009). Development and characterization of *in vivo* flexible electrodes compatible with large tissue displacements. *Journal of Neural Engineering*, 6(2).
- [84] Lee, S. E., Jun, S. B., Lee, H. J., Kim, J., Lee, S. W., Im, C., Shin, H. C., Chang, J. W., & Kim, S. J. (2012). A Flexible Depth Probe Using Liquid Crystal Polymer. *IEEE Transactions on Biomedical Engineering*, 59(7), 2085–2094.
- [85] Jeong, Y. S., Ratier, B., Moliton, A., & Guyard, L. (2002). UV–visible and infrared characterization of poly(p-xylylene) films for waveguide applications and OLED encapsulation. *Synthetic Metals*, 127(1–3), 189–193.
- [86] Liu, C., Wang, D., Wang, W., Song, Y., Li, Y., Zhou, H., Chen, C., & Zhao, X. (2013). Synthesis of soluble and autophotosensitive hyperbranched polyimides with good optical properties and thermal properties. *Polymer Journal*, 45(3), 318–325.
- [87] Park, J. H., Jeong, J., Moon, H., Kim, C., & Kim, S. J. (2016). Feasibility of LCP as an Encapsulating Material for Photodiode-Based Retinal Implants. *IEEE Photonics Technology Letters*, 28(9), 1018–1021.
- [88] Bernard, M., Jubeli, E., Bakar, J., Tortolano, L., Saunier, J., & Yagoubi, N. (2017). Biocompatibility assessment of cyclic olefin copolymers: Impact of two additives on cytotoxicity, oxidative stress, inflammatory reactions, and hemocompatibility. *Journal of Biomedical Materials Research Part A*, 105(12), 3333–3349.
- [89] COP Zeonex. (n.d.). Retrieved November 21, 2016, from: http://www.zeon.co.jp/business_e/enterprise/speplast/speplast1.html.
- [90] COP ZeonorFilm. (n.d.). Retrieved November 21, 2016, from: <http://www.zeon.co.jp>

p/business_e/enterprise/speplast/speplast2.html.

- [91] LCP Vecstar. (n.d.). Retrieved September 15, 2018, from: https://www.kuraray.eu/fileadmin/presse/publikationen/downloads_k_fair_2013/New_business_development_division/Kuraray_LCP_Film_Brochure.pdf.
- [92] Parylene-C GALXYL. (n.d.). Retrieved September 15, 2018, from: http://www.vp-scientific.com/parylene_properties.htm.
- [93] Polyimide PI-2525. (n.d.). Retrieved September 15, 2018, from: http://www.dupont.com/content/dam/dupont/products-and-services/electronic-and-electrical-materials/semiconductor-fabrication-and-packaging-materials/documents/PI-2525_2555_2574_ProductBulletin.pdf.
- [94] Lee, D. S., Yang, H., Chung, K. H., & Pyo, H. B. (2005). Wafer-Scale Fabrication of Polymer-Based Microdevices via Injection Molding and Photolithographic Micropatterning Protocols. *Analytical Chemistry*, 77(16), 5414–5420.
- [95] Illa, X., Ordeig, O., Snakenborg, D., Romano-Rodríguez, A., Compton, R. G., & Kutter, J. P. (2010). A cyclic olefin polymer microfluidic chip with integrated gold microelectrodes for aqueous and non-aqueous electrochemistry. *Lab on a Chip*, 10(10), 1254–1261.
- [96] Nunes, P. S., Ohlsson, P. D., Ordeig, O., & Kutter, J. P. (2010). Cyclic olefin polymers: emerging materials for lab-on-a-chip applications. *Microfluidics and Nanofluidics*, 9(2–3), 145–161.
- [97] Lu, C., Froriep, U. P., Koppes, R. A., Canales, A., Caggiano, V., Selvidge, J., Bizzi, E., & Anikeeva, P. (2014). Polymer Fiber Probes Enable Optical Control of Spinal Cord and Muscle Function In Vivo. *Advanced Functional Materials*, 24(42), 6594–6600.
- [98] Rai, V. N., Srivastava, A. K., Mukherjee, C., & Deb, S. K. (2012). Surface enhanced absorption and transmission from dye coated gold nanoparticles in thin films. *Applied Optics*, 51(14), 2606–2615.
- [99] Axelevitch, A., & Apter, B. (2015). In-situ investigation of optical transmittance in metal thin films. *Thin Solid Films*, 591, 261–266.
- [100] Bonham, B. H., & Litvak, L. M. (2008). Current focusing and steering: Modeling, physiology, and psychophysics. *Hearing Research*, 242(1–2), 141–153.
- [101] Berenstein, C. K., Mens, L. H., Mulder, J. J., & Vanpoucke, F. J. (2008). Current Steering and Current Focusing in Cochlear Implants: Comparison of Monopolar, Tripolar, and Virtual Channel Electrode Configurations. *Ear and Hearing*, 29(2),

250–260.

- [102] Martens, H. C. F., Toader, E., Decré, M. M. J., Anderson, D. J., Vetter, R., Kipke, D. R., Baker, K. B., Johnson, M. D., & Vitek, J. L. (2011). Spatial steering of deep brain stimulation volumes using a novel lead design. *Clinical Neurophysiology*, *122*(3), 558–566.
- [103] Firszt, J. B., Koch, D. B., Downing, M., & Litvak, L. (2007). Current Steering Creates Additional Pitch Percepts in Adult Cochlear Implant Recipients. *Otology & Neurotology*, *28*(5), 629–636.
- [104] Wong, Y. T., Dommel, N., Preston, P., Hallum, L. E., Lehmann, T., Lovell, N. H., & Suaning, G. J. (2007). Retinal Neurostimulator for a Multifocal Vision Prosthesis. *IEEE Transactions on Neural Systems and Rehabilitation Engineering*, *15*(3), 425–434.
- [105] Rizzo III, J. F. (2011). Update on Retinal Prosthetic Research: the Boston Retinal Implant Project. *Journal of Neuro-Ophthalmology*, *31*(2), 160–168.
- [106] Chuang, A. T., Margo, C. E., & Greenberg, P. B. (2014). Retinal implants: a systematic review. *British Journal of Ophthalmology*, *98*(7), 852–856.
- [107] Shepherd, R. K., Shivdasani, M. N., Nayagam, D. A., Williams, C. E., & Blamey, P. J. (2013). Visual prostheses for the blind. *Trends in Biotechnology*, *31*(10), 562–571.
- [108] Chow, A. Y., Pardue, M. T., Chow, V. Y., Peyman, G. A., Liang, C., Perlman, J. I., & Peachey, N. S. (2001). Implantation of Silicon Chip Microphotodiode Arrays into the Cat Subretinal Space. *IEEE Transactions on Neural Systems and Rehabilitation Engineering*, *9*(1), 86–95.
- [109] Stingl, K., Bartz-Schmidt, K. U., Besch, D., Chee, C. K., Cottrill, C. L., Gekeler, F., Groppe, M., Jackson, T. L., MacLaren, R. E., Koitschev, A., Kusnyerik, A., Neffendorf, J., Nemeth, J., Naeem, M. A. N., Peters, T., Ramsden, J. D., Sachs, H., Simpson, A., Singh, M. S., Wilhelm, B., Wong, D., & Zrenner, E. (2015). Subretinal Visual Implant Alpha IMS-Clinical trial interim report. *Vision Research*, *111*, 149–160.
- [110] Safaric, S., & Malaric, K. (2006, June). ZigBee wireless standard. In *Proceedings ELMAR 2006* (pp. 259–262). IEEE.
- [111] Kuzminykh, I., Snihurov, A., & Carlsson, A. (2017, February). Testing of Communication Range in ZigBee Technology. In *2017 14th International Conference The Experience of Designing and Application of CAD Systems in Microelectronics (CADSM)* (pp. 133–136). IEEE.

- [112] Motta, P. S., & Judy, J. W. (2005). Multielectrode Microprobes for Deep-Brain Stimulation Fabricated with a Customizable 3-D Electroplating Process. *IEEE Transactions on Biomedical Engineering*, 52(5), 923–933.
- [113] Pearson, C. E. (1956). General theory of elastic stability. *Quarterly of Applied Mathematics*, 14(2), 133–144.
- [114] Moon, T., Ghovanloo, M., & Kipke, D. R. (2003, September). Buckling Strength of Coated and Uncoated Silicon Microelectrodes. In *Proceedings of the 25th Annual International Conference of the IEEE Engineering in Medicine and Biology Society (IEEE Cat. No. 03CH37439)* (Vol. 2, pp. 1944–1947). IEEE.
- [115] Matteucci, P. B., Chen, S. C., Tsai, D., Dodds, C. W., Dokos, S., Morley, J. W., Lovell, N. H., & Suaning, G. J. (2013). Current Steering in Retinal Stimulation via a Quasimonopolar Stimulation Paradigm. *Investigative Ophthalmology & Visual Science*, 54(6), 4307–4320.
- [116] Gomez, C., Oller, J., & Paradells, J. (2012). Overview and Evaluation of Bluetooth Low Energy: An Emerging Low-Power Wireless Technology. *Sensors*, 12(9), 11734–11753.
- [117] Jeong, J., Bae, S. H., Seo, J. M., Chung, H., & Kim, S. J. (2016). Long-term evaluation of a liquid crystal polymer (LCP)-based retinal prosthesis. *Journal of Neural Engineering*, 13(2).
- [118] Cha, K., Horch, K., & Normann, R. A. (1992). Simulation of a Phosphene-Based Visual Field: Visual Acuity in a Pixelized Vision System. *Annals of Biomedical Engineering*, 20(4), 439–449.
- [119] Min, K. S., Lee, C. J., Jun, S. B., Kim, J., Lee, S. E., Shin, J., Chang, J. W., & Kim, S. J. (2014). A Liquid Crystal Polymer-Based Neuromodulation System: An Application on Animal Model of Neuropathic Pain. *Neuromodulation: Technology at the Neural Interface*, 17(2), 160–169.
- [120] Ye, X., Wang, P., Liu, J., Zhang, S., Jiang, J., Wang, Q., Chen, W., & Zheng, X. (2008). A portable telemetry system for brain stimulation and neuronal activity recording in freely behaving small animals. *Journal of Neuroscience Methods*, 174(2), 186–193.
- [121] Farahmand, S., Vahedian, H., Eslami, M. A., & Sodagar, A. M. (2012, August). Wearable, Battery-Powered, Wireless, Programmable 8-Channel Neural Stimulator. In *2012 Annual International Conference of the IEEE Engineering in Medicine and Biology Society* (pp. 6120–6123). IEEE.

- [122] Fluri, F., Mützel, T., Schuhmann, M. K., Krstić, M., Endres, H., & Volkmann, J. (2017). Development of a head-mounted wireless microstimulator for deep brain stimulation in rats. *Journal of Neuroscience Methods*, 291, 249–256.
- [123] Kendir, G. A., Liu, W., Wang, G., Sivaprakasam, M., Bashirullah, R., Humayun, M. S., & Weiland, J. D. (2005). An Optimal Design Methodology for Inductive Power Link With Class-E Amplifier. *IEEE Transactions on Circuits and Systems I: Regular Papers*, 52(5), 857–866.
- [124] Acar, M., Annema, A. J., & Nauta, B. (2007). Analytical Design Equations for Class-E Power Amplifiers. *IEEE Transactions on Circuits and Systems I: Regular Papers*, 54(12), 2706–2717.
- [125] Seo, J., Choi, G. J., Park, S., Lee, J., Baek, C., Jang, J., Lim, J., Shin, S., Seo, K., Seo, J. M., Song, Y. K., & Kim, S. J. (2017, July). Wireless Navigation of Pigeons using Polymer-Based Fully Implantable Stimulator: A Pilot Study using Depth Electrodes. In *2017 39th Annual International Conference of the IEEE Engineering in Medicine and Biology Society (EMBC)* (pp. 917–920). IEEE.
- [126] Cai, L., Dai, Z., Wang, W., Wang, H., & Tang, Y. (2015). Modulating Motor Behaviors by Electrical Stimulation of Specific Nuclei in Pigeons. *Journal of Bionic Engineering*, 12(4), 555–564.
- [127] Shin, S., Kim, J., Jeong, J., Gwon, T. M., Choi, G. J., Lee, S. E., Kim, J., Jun, S. B., Chang, J. W., & Kim, S. J. (2016). High Charge Storage Capacity Electrodeposited Iridium Oxide Film on Liquid Crystal Polymer-Based Neural Electrodes. *Sensors and Materials*, 28, 243–260.
- [128] Oghogho, I., Edeko, F. O., & Emagbetere, J. (2018). Measurement and modelling of TCP downstream throughput dependence on SNR in an IEEE802.11b WLAN system. *Journal of King Saud University-Engineering Sciences*, 30(2), 170–176.
- [129] Rubehn, B., & Stieglitz, T. (2010). In vitro evaluation of the long-term stability of polyimide as a material for neural implants. *Biomaterials*, 31(13), 3449–3458.
- [130] Boreman, G. D. (2001). *Modulation Transfer Function in Optical and Electro-Optical Systems* (Vol. 4). Bellingham, WA: SPIE press.
- [131] Kolb, H. (2007). Gross Anatomy of the Eye. In *Webvision: The Organization of the Retina and Visual System [Internet]*. University of Utah Health Sciences Center.
- [132] Adeeb, M. A. (2006). A Class-E Inductive Powering Link with Backward Data Communications for Implantable Sensor Systems.

Supplements

S.1. Solubility, Diffusivity, and Permeability of COP

To further discuss the long-term reliability of COP encapsulation, solubility, diffusivity, and permeability of COP need to be considered and estimated as in the following reference [117]. Although these properties are not used in this thesis, they can be helpful for calculating relative humidity or water vapor concentration in COP encapsulation for future studies.

Solubility is a chemical property of the ability for a given substance to dissolve in a solvent. In this case, a given substance and a solvent are COP and water vapor, respectively. Based on the Henry's law, the solubility of COP S_{COP} is presented as follows (S.1),

$$S_{\text{COP}} = \frac{\left(\frac{\text{density of COP}}{\text{COP}}\right) \times \left(\frac{\text{water absorption}}{\text{rate of COP}}\right) \times \left(\frac{\text{water vapor}}{\text{volume at } T}\right)}{\left(\frac{\text{weight of}}{\text{water vapor}}\right)} \quad (\text{S.1})$$

where T is the body temperature herein. As a result, S_{COP} can be calculated to be 0.14 (dimensionless).

In addition, diffusivity is a rate of diffusion, which means the coefficient of proportionality between the molecular flux due to diffusion and the gradient in the concentration of a barrier. This property can be generally expressed by the Fick's first law. To estimate the diffusivity of COP D_{COP} , its water vapor transmission rate (WVTR) was firstly measured by a WVTR testing apparatus (PERMATRAN-W 3/33 MA, MOCON, Inc., USA), provided by the Prof. Park, C. R.'s laboratory of the Department of Materials Science and Engineering in Seoul National University.

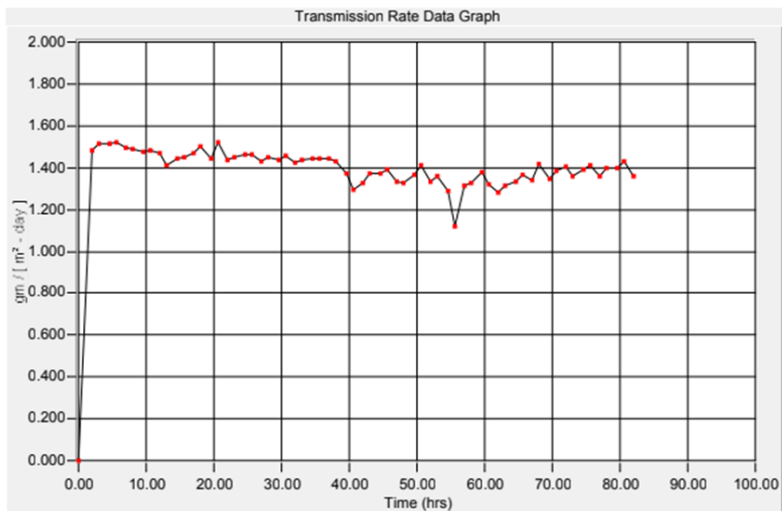
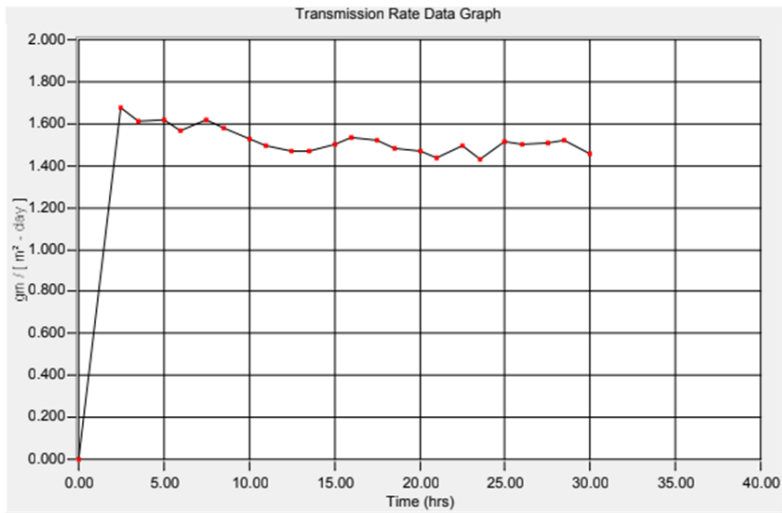


Figure S.1.1 WVTR measurement results of a bare 100- μm -thick COP film (top) and a thermally laminated COP film with a total thickness of 100 μm (bottom), respectively.

In this measurement, a bare 100- μm -thick COP film and a thermally laminated COP film with a total thickness of 100 μm were used. Figure S.1.1 shows WVTR measurement results. The WVTRs of the bare COP film and the thermally laminated COP film were evaluated as 0.150 and 0.146 $\text{g}\cdot\text{mm}/(\text{m}^2\cdot\text{day})$, respectively. After

thermal lamination, the WVTR seemed to be slightly decreased, but no significant effect of thermal lamination on the WVTR was observed. With the WVTRs and the Fick's first law, D_{COP} can be calculated to be 1.74×10^{-11} cm²/s for the bare COP film and to be 1.69×10^{-11} cm²/s for the thermally laminated COP film.

Lastly, permeability indicates the penetration of a permeate through a solid. In this case, a permeate is water vapor, and a solid is COP. By approximating the Fick's law, the permeability of COP P_{COP} can be simply estimated as follows (S.2),

$$P_{\text{COP}} = D_{\text{COP}} \times S_{\text{COP}}. \quad (\text{S.2})$$

Using the calculated values above, P_{COP} can be evaluated to be 2.44×10^{-12} cm²/s for the bare COP film and to be 2.36×10^{-12} cm²/s for the thermally laminated COP film.

As mentioned above, these properties of COP were only estimated in this supplement and not used to evaluate the long-term reliability as in the following reference [117]. These values might be useful in future studies on the estimation of lifetimes of COP encapsulation, for example, against the penetration of moisture and ions through a COP surface.

S.2. Complete Results of the Penta-Polar Stimulation



Figure S.2.1 FEA results of the steered electric field measurements using the penta-polar stimulation when the recording distance from the stimulation electrodes was $13\ \mu\text{m}$.



Figure S.2.2 FEA results of the steered electric field measurements using the penta-polar stimulation when the recording distance from the stimulation electrodes was $50\ \mu\text{m}$.



Figure S.2.3 FEA results of the steered electric field measurements using the pentapolar stimulation when the recording distance from the stimulation electrodes was 100 μm .



Figure S.2.4 FEA results of the steered electric field measurements using the pentapolar stimulation when the recording distance from the stimulation electrodes was 150 μm .



Figure S.2.5 FEA results of the steered electric field measurements using the pentapolar stimulation when the recording distance from the stimulation electrodes was 200 μm .



Figure S.2.6 FEA results of the steered electric field measurements using the pentapolar stimulation when the recording distance from the stimulation electrodes was 250 μm .

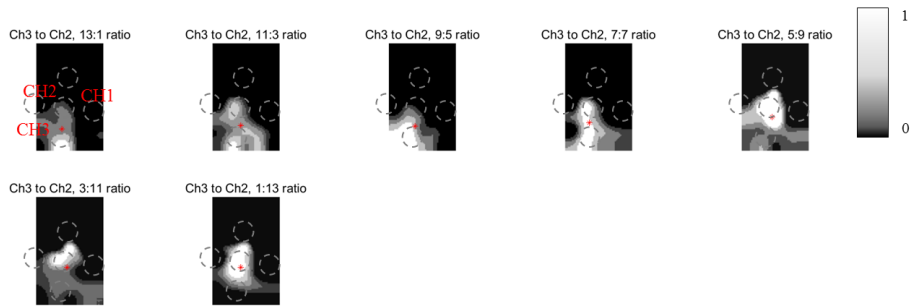


Figure S.2.7 *In vitro* evaluation results of the steered electric field measurements using the penta-polar stimulation when the recording distance from the stimulation electrodes was 13 μm .

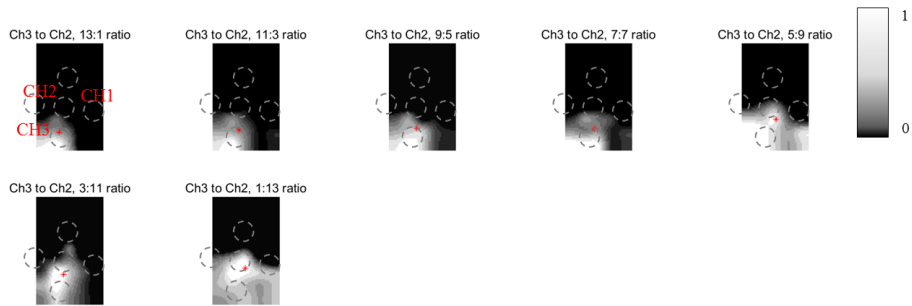


Figure S.2.8 *In vitro* evaluation results of the steered electric field measurements using the penta-polar stimulation when the recording distance from the stimulation electrodes was 50 μm .

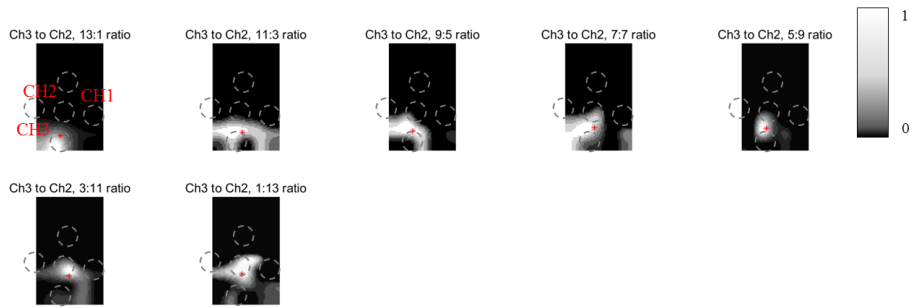


Figure S.2.9 *In vitro* evaluation results of the steered electric field measurements using the penta-polar stimulation when the recording distance from the stimulation electrodes was 100 μm .

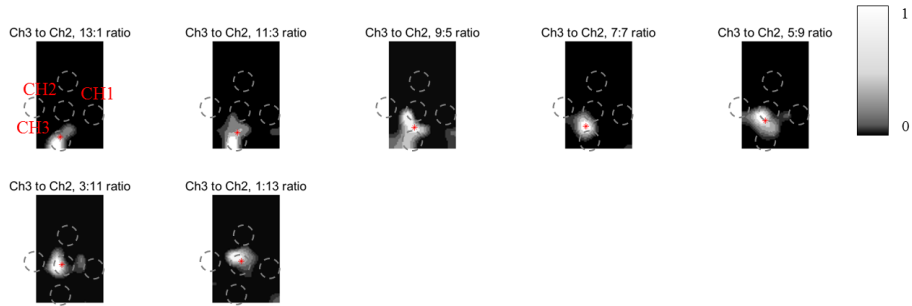


Figure S.2.10 *In vitro* evaluation results of the steered electric field measurements using the penta-polar stimulation when the recording distance from the stimulation electrodes was 150 μm .

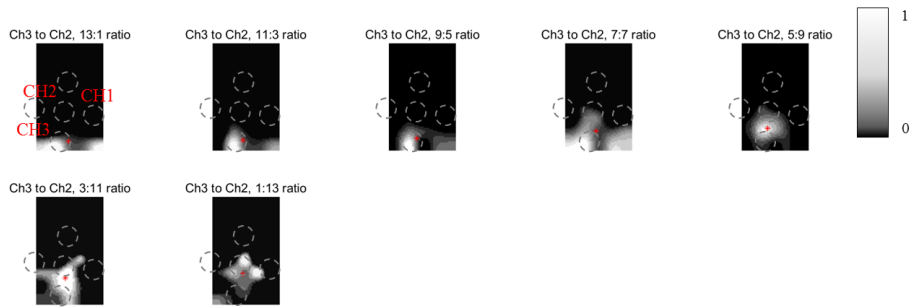


Figure S.2.11 *In vitro* evaluation results of the steered electric field measurements using the penta-polar stimulation when the recording distance from the stimulation electrodes was 200 μm .

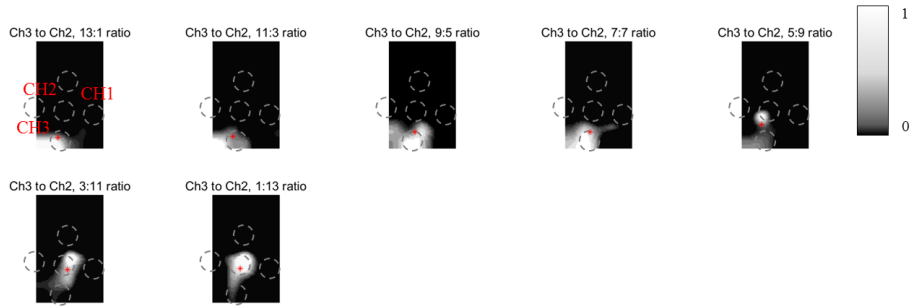


Figure S.2.12 *In vitro* evaluation results of the steered electric field measurements using the penta-polar stimulation when the recording distance from the stimulation electrodes was 250 μm .

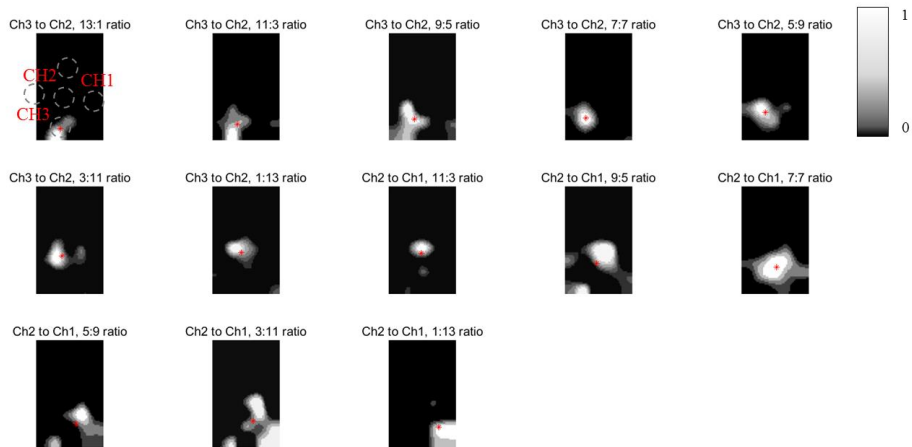


Figure S.2.13 *In vitro* evaluation results of the steered electric field measurements especially in two dimensions along with more diverse directions using the pentapolar stimulation when the recording distance from the stimulation electrodes was $150\ \mu\text{m}$.

국문 초록

시각 보철 시스템은 일반적으로 실명 환자들의 부분 시력을 전기 자극으로 회복시키기 위하여 수술적으로 이식될 수 있는 장치인 신경 자극기와 이미지 센서 또는 컨트롤러, 프로세서를 포함하는 외부의 주변 장치들로 구성된다. 망막 보철 장치 또는 망막 임플란트와 같이 몇몇 시각 보철 시스템은 이미 상용화 되었지만, 여전히 더 나은 시각 보철 시스템을 위하여 다뤄져야 할 많은 이슈들 (예를 들어, 이식형 장치의 기관 물질, 전극의 배열, 외부 하드웨어의 사용, 전력 공급 및 데이터 전송 방법, 설계 및 제작 방식 등)이 있다. 본 학위논문은 완전 이식형 시각 보철 시스템을 제안하며, 이를 위하여 다음과 같이 중요하다고 생각되는 총 네 가지의 이슈들과 관련된 연구 내용을 다룬다.

- 1) 폴리머를 기반으로 한 신경 자극기의 미세 전극 및 패키지와 같은 이식 가능한 부분을 반도체 기술 없이 간단하게 제작하는 방법과
- 2) 제한된 공간에서 전극 개수의 물리적인 한계를 극복하기 위하여 가상 채널을 형성하는 다극성 자극 방식,
- 3) 이식형 카메라를 사용하는 새로운 이미지 획득 전략,
- 4) 환자의 다양한 활동을 방해하지 않으면서 신경 자극기에 전력을 공급하고 데이터를 전송하는 방법.

첫째로, 금속이나 실리콘, 세라믹에 비하여 폴리머는 유연성 및 미세 제작에의 적용 가능성을 포함하는 두드러진 이점들이 있기 때문에 시각 보철 시스템을 구성하는 다양한 이식 가능한 부분들에 널리 이용되었다. 대부분의 폴리머 기반 이식형 장치들은 금속 증착과 사진 식각을 기반으로 하는 반도체 공정으로 제작되었다. 이 공정은 폴리머

기판 위에 금속을 패터닝 하는 데에 있어서 높은 정확성과 정밀도를 제공한다. 하지만 그 공정은 또한, 사진 식각에 쓰이는 마스크와 금속 증착을 위한 진공뿐만 아니라 아주 큰 공정 설비를 요구하기 때문에 시간 소모가 심하고 복잡하다. 이는 본 연구에서 낮은 수분 흡수 (<0.01 %)와 높은 빛 투과 (92 %)를 특징으로 하는 생체적합한 고리형 올레핀 폴리머 (cyclic olefin polymer, COP)가 이식형 장치를 위한 새로운 기판 물질로써 선택된 이유이다. COP를 기반으로 하여, 마스크와 진공, 큰 공정 설비가 필요 없이 이식 가능한 장치를 간단하게 제작하는 공정이 개발되었다. COP는 금과의 강한 접합과 자외선에 대한 높은 투명성을 또 다른 특징으로 한다. 이와 같은 접합 특성과 자외선 투명성 덕분에, 금박은 COP 기판에 별도의 접합층 없이 열로 접합될 수 있을 뿐만 아니라 그 기판에 손상을 주지 않으면서 자외선 레이저를 통하여 미세하게 가공될 수 있다. 개발된 COP 기반의 공정을 처음으로 사용하여 침습형 미세 프로브가 제작되었고, 그 전기화학적, 기계적 특성과 기능성이 각각 임피던스 측정과 버클링 테스트, 생체 내 신경신호 기록으로 평가되었다. 그리고 COP를 사용한 밀봉의 가능성도 알아보기 위하여, 개발된 공정을 사용하여 형성된 COP 밀봉의 장기 안정성이 생리식염수에서의 가속 노화 중 누설 전류 측정을 통하여 추정되었다.

둘째로, 자극 전극의 크기가 충분히 작아진다고 하더라도, 동시에 출력되는 자극에 의해 형성되는 전기장의 중첩인 크로스 토크 때문에 개개의 신경세포를 정밀하게 자극하기 위하여 전극을 배열하는 것은 아주 어렵다. 따라서 인접한 전극 사이에 적당한 간격이 필요하게

되고, 이는 특히 뇌 또는 망막과 같은 제한된 공간에서 전극 개수의 물리적인 한계를 야기한다. 이 한계를 극복하기 위하여, 많은 연구자들은 실제 전극 사이에서 큰 전기장 세기를 갖는 중간 영역을 나타내는 가상 채널을 이용한 자극 전략을 제안하였다. 이러한 가상 채널은 둘 이상의 전극에서 동시에 출력되는 자극 파형을 합칠 수 있는 다극성 자극에 의하여 형성이 가능하다. 본 연구에서는 가상 채널을 이용하여 더 정교한 자극 패턴을 만들기 위하여, 특히 2차원에서의 가상 채널을 생성하고자 격자형 배열의 전극과 함께 5극성 자극이 사용되었다. 이 5극성 자극은 다섯 개의 서로 다른 전류원을 갖도록 맞춤 설계된 집적회로와 개발된 COP 기반 공정으로 제작된 평면형 전극을 사용하여 구현되었다. 먼저, 5극성 자극의 효과를 확인하고자 이 자극으로 전기장을 한 곳에 더 집중된 형태로 만들 수 있음이 단극성 자극과의 비교를 통하여 검증되었다. 그리고 유한 요소 분석과 생체 외 평가 둘 모두를 통하여, 5극성 자극으로 인한 가상 채널 형성을 뜻하는 전기장 분포가 인접한 두 전극에서 나오는 자극의 진폭비와 그 전극으로부터 떨어진 거리에 따라 변화됨이 추정되었다.

셋째로, 본 연구에서는 눈에 이식된 채로 실시간 이미지를 얻음으로써 완전 이식형 시각 보철 시스템을 구성하는 이식형 카메라를 새로운 이미지 획득 방식으로써 제안한다. 이 이식형 카메라는 실명 환자들이 자연스러운 눈의 움직임을 따라서 물체를 볼 수 있으며 잠이나 샤워, 달리기와 같은 일상적인 활동들을 방해 받지 않고 수행할 수 있도록 돕는다는 점에서 독특한 장점을 갖는다. 기존의 부분 이식형 시각 보철 시스템에서 쓰이는 안경 부착형 카메라와 같은 착용 장비로는

이러한 장점들을 얻을 수 없다. 게다가, 이식형 카메라는 망막 임플란트의 미세 포토다이오드 어레이와 달리 완전한 카메라 구조를 이용하여 다양한 이미지 정보를 획득할 수 있다는 장점을 갖는다. 이러한 이점들을 달성하기 위하여, 그 이식형 카메라는 수분 침투를 막고자 생체적합한 에폭시로 코팅되었고 생체적합성과 유연성을 얻기 위하여 의료용 실리콘 엘라스토머로 밀봉된 후에 눈에 충분히 삽입될 수 있는 형태 및 크기로 제작되었다. 이 장치의 동작은 흑백으로 처리된 이미지를 표시하는 무선 이미지 획득으로 시험되었다. 그리고 몸 안에서 이식형 카메라 갖는 안정적인 통신 거리를 측정하기 위하여, 장치가 생체 내 환경을 모사하기 위한 8 mm 두께의 생체 물질로 덮인 상태에서 그 장치의 신호 대 잡음비가 측정되었다.

마지막으로, 기존의 시각 보철 시스템에서 몸에 부착된 형태의 외부 하드웨어는 이식된 장치에 전력과 데이터를 안정적으로 전달하고 이미지 신호를 수집하기 위하여 일반적으로 사용되었다. 그럼에도 불구하고, 이러한 하드웨어는 외부로부터의 손상으로 인한 기능적인 결함과 수면 및 샤워, 달리기, 수영 활동 중 이용 불가능성, 외형적인 이슈 등을 포함하는 공통적인 문제들을 야기한다. 전력 및 데이터 전송을 위한 외부 코일은 시각 보철 시스템에서 컨트롤러와 프로세서에 유선으로 연결되고, 이러한 연결은 그 코일이 앞서 언급된 문제들에 특히 취약하게 만든다. 이러한 이슈를 해결하고자, 휴대용 무선 컨트롤러로 제어되는 완전 이식형 신경 자극 시스템이 제안된다. 이 휴대용 무선 컨트롤러는 저전력이지만 비교적 장거리 통신이 가능한 직비 (ZigBee) 무선 통신을 통하여 재충전 가능한 배터리로 동작하는

완전 이식형 자극기를 제어할 수 있다. 이 외에도, 이 휴대용 컨트롤러를 사용하면 폭넓은 응용을 위한 두 가지 기능을 추가로 수행할 수 있다. 하나는 유선 경피 자극이며, 다른 하나는 재충전 가능한 배터리의 유도 충전 기능이다. 또한, 이 휴대용 컨트롤러의 간단한 스위치를 사용하면 사용자는 게임패드와 같이 자극 파라미터를 쉽게 조절할 수 있다. 이러한 휴대 가능하고 사용자 친화적인 인터페이스를 통해 다양한 상황에서 그 컨트롤러를 쉽게 사용할 수 있다. 그 컨트롤러의 기능은 생체 외 평가뿐만 아니라 조류의 움직임 제어를 위한 유선 경피 자극 및 원격 제어를 통해 생체 내에서도 평가되었다. 또한, 그 컨트롤러를 사용한 원격 신경 자극 제어의 수행 가능성을 검증하기 위하여 두 생체 내 실험의 결과가 서로 비교되었다.

결론적으로, COP 기반의 간단한 제작 공정과 5극성 자극, 이식형 카메라, 휴대용 다기능 무선 컨트롤러를 포함하는 연구 결과에 대한 여러 논의가 이루어진다. 그리고 이러한 결과와 고찰에 기초하여, 본 학위논문의 연구가 완전 이식형 시각 보철 시스템의 구현에 어떻게 적용될 수 있는 지가 이 논문의 끝에서 상세히 설명된다.

주요어: 완전 이식형, 시각 보철 시스템, 고리형 올레핀 폴리머, 간단한 제작 공정, 5극성 자극, 가상 채널, 이식형 카메라, 휴대용 다기능 무선 컨트롤러

학번: 2015-20942